The Combination of Two Concentric Discharge Channels into a Nested Hall-Effect Thruster

by

Raymond Liang

A dissertation submitted in partial fulfillment
of the requirements for the degree of
Doctor of Philosophy
(Aerospace Engineering)
in The University of Michigan
2013

Doctoral Committee:

Professor Alec D. Gallimore, Chair
Professor Iain D. Boyd
Associate Professor John E. Foster
Daniel L. Brown
Peter Y. Peterson

For my parents, Jun Luan Liang and Grace Chen Liang

ACKNOWLEDGEMENTS

Since the summer after my sophomore year, electric propulsion research has remained, in some fashion, part of my higher education. Although I considered and tried to escape on a few occasions, I found that nothing quite compares to the combination of rocket engines and plasmas. There are many people who greatly influenced my journey in the fields of electric propulsion and aerospace engineering. Without their support and guidance, my accomplishments would not have been possible or nearly as enjoyable.

I would like to first thank my doctoral advisor, Professor Alec Gallimore. He took a chance with a rookie who had a crazy idea about nesting Hall thrusters and remained supremely supportive throughout my graduate education, especially when a certain thruster came out of the chamber with destroyed ceramics. The creative freedom I enjoyed under his tutelage is unrivaled, and his guidance was invaluable. I will be forever grateful for the opportunities given to me during my time as his student.

The other members of my committee were also critical to my success as a graduate student. Dr. Peter Peterson made the X2 possible, and I remain appreciative for his guidance on Hall thruster design, fabrication, and testing. Dr. Daniel Brown served as our AFRL sponsor for most of my time as a graduate student and saved me several times with fruitful discussions, helpful tips, paper clearances, and functioning cathode parts. Professor John Foster and Professor Iain Boyd always provided great advice, and I learned much from their courses as well.

I would also like to thank Dr. Brian Beal and Dr. James Haas at the Air Force Research Laboratory and Dr. Mitat Birkan of the Air Force Office of Scientific Research for their support of the X2. Brian Beal was the original sponsor and reviewed all of my original design work. Although my interactions with James Haas were limited, I appreciated his support as branch chief and author of the legendary thesis haiku.

The National Defense Science and Engineering Fellowship and the Department of Aerospace Engineering at the University of Michigan provided funding for my first four years of graduate school. I am very grateful for the financial support from both organizations.

The Plasmadynamics and Electric Propulsion Laboratory is a unique environment that promotes creative thinking and ambitious research, but its former, current, and future people are its greatest resource. Dr. Tim Smith provided much guidance to our lab in general and always served as a good resource of knowledge. I found his pro tips particularly useful. Dr. Mitchell Walker and Dr. Richard Hofer were always very responsive to my questions and provided helpful insights into Hall thruster testing and test equipment. To Doctors Bryan Reid, Kristina Lemmer, Sonca Nguyen, and Bailo Ngom, thank you for showing me the ropes during our brief coincidental time together as students.

I learned a great deal from Doctors Robbie Lobbia, Tom Liu, Ricky Tang, Rohit Shastry, David Huang, and Mike McDonald. Thank you all for your guidance, good times, and help during long tests, late setups, and even later pumpdowns. Robbie, your self-taught electronics knowledge is remarkably impressive, and I appreciated your regular tips to avoid dumb mistakes. Tom, thank you for our many interesting conversations and for your help around the lab. I swear, the ion gauges on LVTF weren't rigged and are indeed reading 10^{-8} . Ricky, I will remain forever impressed with your willingness to serve in our armed forces immediately after you defend your thesis, and your talks on the gas dynamic mirror were always enjoyable. Rohit, a

great deal of my plasma diagnostics knowledge comes from you. I remain grateful for your mentorship and your willingness to answer all sorts of questions. David, thank you for always pushing me to become a better researcher and for asking the hard questions. You have an amazing ability to explain complex concepts in simple and understandable ways. Mike M., we were regularly complete opposites in the lab, but there were also times when we were complementary to each other. Thanks for all the help with the insanity of emissive probes and use of the HARP.

To Doctors Adam Shabshelowitz and Laura Spencer, there are no two other people with whom I would have rather joined PEPL. Although I did not share your affinity (and occasional hatred) of RF and microwave plasmas, I always enjoyed your company throughout our mutual time at Michigan. Adam, thanks for all your help through the years from studying for prelims to building and testing thrusters of various types. You were regularly a great resource for knowledge and made our lab a better place. Laura, thanks for being a cheerful presence in our lab and for trying to save the world before the rest of us destroy it. Your nested cupcakes are amazing!

To Roland Florenz, Chris Durot, Kim Trent, Mike Sekerak, Chris Bellant, and Scott Hall, I know you all will continue to do great work at PEPL. Roland, thank you for all your help with the X2, and I hope you have found my experiences most useful in your continuing work with the X3. May your gigantic thruster reign supreme. Chris D, you're a brave one for tackling the optical diagnostics, and I appreciated your occasional help with experiment setups. Mike S, I have always admired your pursuit of knowledge and the skills you bring to our lab. Thank you for our interesting discussions and our marathon experiment. Kim, we didn't get many opportunities to work together, but I have regularly enjoyed talking with you about your work and passing on whatever knowledge I can. To Chris B and Scott, our common time in the lab was limited, but I know you both will do great work.

My time as a graduate student at the University of Michigan would not have gone

as smoothly without the help with many others within the Department of Aerospace Engineering and College of Engineering. Professor Daniel Scheeres and Professor Werner Dahm were responsible for bringing me to the University of Michigan, and I appreciated their help and guidance during my initial time at UM. I would like to thank Denise Phelps, Suzanne Smith, Cynthia Enoch, Linda Weiss, and Mariette Davis for their much appreciated help with the many processes at our university. Thomas Griffin, Chris Chartier, Eric Kirk, and Aaron Borgman regularly helped us maintain our lab and provided mechanical and electrical advice. Terry Larrow masterfully machined parts for the X2 and always kept an open door to my many questions.

There are a number of people outside of the University of Michigan who aided my work. Dr. Dean Massey provided a great deal of help around PEPL during his stay in Ann Arbor, and I appreciated his willingness to help at all hours of the day and for his creation of the xenon recovery system. Dr. Dan Goebel provided critical advice regarding cathodes and always remained patient with students. Bill Cleveland and the crew at Precision Manufacturing Services also masterfully machined parts for the X2 and were always welcoming during my visits to their shop. Jonathan Zagel and Eric Viges of ElectroDynamic Applications regularly helped with xenon supply and recovery, and their efforts were much appreciated.

During my time at Virginia Tech, there were several professors who were instrumental in the early stages of my higher education. I would like to thank Dr. Joseph Wang, who was the first to take a chance with my inexperienced self. He was the first of my teachers in electric propulsion and took me on before I took a single fluids course. Dr. Hanspeter Schaub provided terrific advice on choosing graduate schools and is also responsible for my affinity toward astrodynamics. Dr. Chris Hall also provided critical guidance during my undergraduate studies, and I appreciated my short time in his Space Systems Simulation Laboratory. Lastly, I would like to thank

Dr. Charles Dudley, Dr. Terry Papillon, and the rest of University Honors for their encouragement of undergraduate research.

As appears to be PEPL tradition, I have left those closest to me for the finale. To my mom and dad, you have always supported my education and worked extremely hard to provide everything I needed. I hope to make you both proud. To my fiancée, Monica Meyerhardt, thank you for waiting for me all these years and for being the highlight of every day. I promise these people named Giggles and Shuffles are not figments of my imagination or muppets running amuck in the lab. I'll be coming home to you soon, and there I will stay for the rest of our lives.

Ray Liang

TABLE OF CONTENTS

LIST OF FIGURES

Figure

LIST OF TABLES

Table

NOMENCLATURE

Roman

A_c	collector area	[cm^2]
B, $\vec{B}$	magnetic field (scalar, vector)	[G]
d_{IC}	inner-channel mean diameter	[mm]
d_{OC}	outer-channel mean diameter	[mm]
d_{plate}	E×B probe E-plate separation distance	[m]
e	elementary charge	[C]
E, $\vec{E}$	electric field (scalar, vector)	[V/m]
F, $\vec{F}$	force (scalar, vector)	[N]
g_0	standard gravitational acceleration at sea level	[m/s]
i	charge species index	[-]
I	current, probe current	[A]
I_A	combined axial beam current	[A]
I_{A_k}	axial beam current for the k-th channel	[A]
I_b	beam current	[A]
I_d	discharge current	[A]
I_{sp}	specific impulse	[s]
$I_{sp,a}$	anode specific impulse	[s]
I_+	collected ion current	[A]
j	current density, ion current density	[mA/cm^2]
k	channel index	[-]
k_B	Boltzmann constant	[J/K]
m_e	electron mass	[kg]
m_i	initial spacecraft mass	[kg]
m_f	final spacecraft mass	[kg]
m_p	propellant mass	[kg]

m_{Xe}	xenon ion mass	[kg]
$\dot{m}_a$	anode mass flow rate	[mg/s, kg/s]
$\dot{m}_c$	cathode mass flow rate	[mg/s, kg/s]
$\dot{m}_i$	ion mass flow rate	[mg/s, kg/s]
$\dot{m}_p$	propellant mass flow rate	[mg/s, kg/s]
$\dot{m}_t$	total mass flow rate	[mg/s, kg/s]
M	number of nested channels	[-]
N	number of charge species	[-]
p	pressure, indicated pressure	[torr]
p_b	base pressure	[torr]
p_c	corrected pressure	[torr]
P_d	discharge power	[W]
P_{htr}	cathode heater power	[W]
P_{kpr}	cathode keeper power	[W]
P_{mag}	electromagnet power	[W]
P_t	total power	[W]
q	charge	[C]
Q	average charge (factor) of ions	[-]
r	radial position	[m]
r_L	Lamour or gyrotron radius	[m]
T	thrust	[mN]
T_1	inner-channel thrust in single-channel mode	[mN]
T_2	outer-channel thrust in single-channel mode	[mN]
T_1'	inner-channel thrust in dual-channel mode	[mN]
T_2'	outer-channel thrust in dual-channel mode	[mN]
T_e	electron temperature	[eV]
v, $\vec{v}$	velocity (scalar, vector)	[m/s]
v_e	effective exhaust velocity	[m/s]
v_i	ion velocity	[m/s]
v_{pass}	E×B probe ion pass velocity	[km/s]
v_{th}	thermal velocity	[m/s]
V	voltage, probe voltage, grid voltage	[V]
V_a	acceleration voltage	[V]

V_c	cathode coupling voltage	[V]
V_{cg}	cathode-to-ground voltage	[V]
V_d	discharge voltage	[V]
V_{mp}	most-probable voltage	[V]
V_p	plasma potential	[V]
V_{plate}	E×B probe applied E-plate voltage	[V]
z	axial position	[mm]
Z	charge state integer	[-]

Greek

β	plume divergence half-angle	[deg]
Δv	velocity change	[km/s]
η_a	anode efficiency	[-]
η_b	current utilization efficiency	[-]
η_{b_A}	axial current utilization efficiency	[-]
η_c	cathode efficiency	[-]
η_d	divergence utilization efficiency	[-]
η_m	mass utilization efficiency	[-]
η_{m_A}	axial mass utilization efficiency	[-]
η_{mag}	electromagnet efficiency	[-]
η_q	charge utilization efficiency	[-]
η_t	total efficiency	[-]
η_v	voltage utilization efficiency	[-]
τ_b	current factor	[-]
τ_d	divergence factor	[-]
τ_q	charge factor	[-]
τ_v	voltage factor	[-]
Υ	individual thrust ratio	[-]
Υ_t	total thrust ratio	[-]
ϕ	polar angle about thruster centerline	[-]
Φ	particle flux	[$1/\text{m}^2/\text{s}$]
Ω	ion species current fraction	[-]

Abbreviations

AFOSR	Air Force Office of Scientific Research

AFRL	Air Force Research Laboratory
CDT	Closed Drift Thruster
CEX	Charge EXchange
CFF	Cathode Flow Fraction
DC	Direct Current
EP	Electric Propulsion
HARP	High-speed Axial Reciprocating Probe
HET	Hall-Effect Thruster
JPL	Jet Propulsion Laboratory
LaB_6	Lanthanum Hexaboride
LVDT	Linear Variable Differential Transformer
LVTF	Large Vacuum Test Facility
MACEEP	Michigan Air Force Center of Excellence in Electric Propulsion
NASA	National Aeronautics and Space Administration
NHT	Nested Hall-effect Thruster
PEPL	Plasmadynamics and Electric Propulsion Laboratory
PPU	Power Processing Unit
PID	Proportional Integral Derivative
RPA	Retarding Potential Analyzer
SOTA	State Of The Art
SPT	Stationary Plasma Thruster
TAL	Thruster with Anode Layer
UM	University of Michigan
XIPS	Xenon Ion Propulsion System

ABSTRACT

The Combination of Two Concentric Discharge Channels into a Nested Hall-Effect Thruster

by

Raymond Liang

Chair: Alec D. Gallimore

Hall-effect thrusters continue to be one of the most efficient technologies for spacecraft maneuvering and stationkeeping. One of the ongoing efforts in the electric propulsion community is to scale Hall-effect thrusters to high powers (10 kW - 1 MW) while maximizing performance and minimizing the thruster's mass and size. A nested Hall-effect thruster is one configuration that can satisfy these goals, but the concept was largely untested until the development of a demonstration thruster by the University of Michigan and the Air Force Research Laboratory, with later sponsorship from the Air Force Office of Scientific Research. This prototype nested Hall-effect thruster, known as the X2, features two concentric, annular discharge channels in which xenon gas undergoes ionization and acceleration. Both discharge channels proved capable of operating separately or simultaneously using a shared hollow cathode.

Performance measurements showed capabilities on par with state-of-the-art Hall-effect thrusters with additional benefits in low-voltage operation with simultaneous firing of both channels. The X2's unique features include the availability of single-channel and dual-channel modes. The combination of all modes extends the throttling

range of the X2 by allowing the exit area to vary according to the desired thrust-to-power ratio and specific impulse.

This study of the X2 nested Hall-effect thruster also investigates how two simultaneously firing channels combine. Thrust measurements show a small increase in performance beyond common facility effects on electric propulsion devices. An array of plasma diagnostics provide further detail on the mechanisms that are responsible for the thrust augmentation, including changes in ion acceleration and ion beam current.

CHAPTER I

Introduction

1.1 Problem Statement

The continuing exploration and utilization of space will always require efficient and effective methods of propulsion. Of the many technologies developed for space propulsion, this work focuses on improving the capabilities of one particular device known as a Hall-effect thruster (HET). HETs belong within a category of technologies known as electric propulsion (EP) and enable missions that require low propellant mass fractions and high velocity changes. The applications for Hall-effect thrusters include stationkeeping of geostationary satellites and primary propulsion for deep-space exploration.

Over the 60-year history of HET development, researchers and developers have proposed various methods for configuring and scaling Hall-effect thrusters [1–8]. This work investigates the feasibility and capabilities of one particular type of HET known as a nested Hall-effect thruster (NHT). The concept of NHTs is not particularly new, but prior to the research conducted for this work, the characteristics and performance of NHTs remained largely unknown or unpublished.

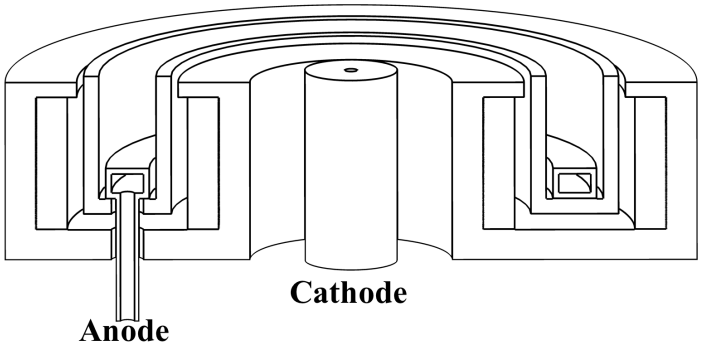

(a) Hall-effect thruster

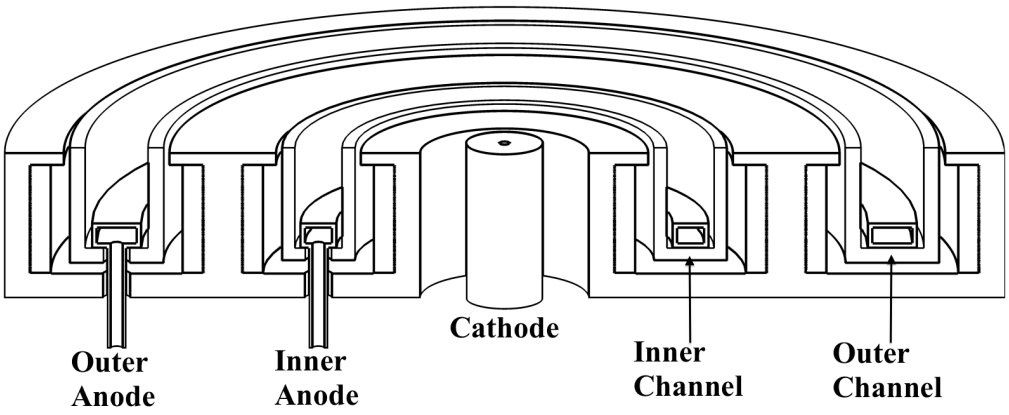

(b) Nested Hall-effect thruster

Figure 1.1: **Notional representations of a Hall-effect thruster and a nested Hall-effect thruster, arbitrarily scaled and proportioned for illustrative purposes only**

1.2 Aim and Scope

The aim of this work is to investigate the nature of two simultaneously-firing discharge channels integrated into a single nested Hall-effect thruster. Accomplishing this aim involved the development of one of the first NHTs, known as the X2. Named for its two discharge channels, the X2 is a concept demonstrator developed by the University of Michigan (UM) and the Air Force Research Laboratory (AFRL) utilizing existing HET design philosophies.

The unique contributions of this work to the field of electric propulsion include the determination of the performance of a NHT and the demonstration of single-channel and dual-channel operation of a NHT with two concentric discharge channels. More importantly, this investigation focuses on the unique features of the nested configuration with particular emphasis on the manner in which the two discharge channels combine. The mechanisms through which thrust can be augmented in dual-channel mode are identified through the use of various plasma diagnostics. These same measurements also provide a first-ever plume characterization of two simultaneously-firing nested discharge channels.

1.3 Overview of Study

The remaining chapters of this thesis will further describe this study of a NHT. Chapter II provides background knowledge on electric propulsion, fundamental parameters, and efficiency models. Information on Hall-effect thrusters and NHTs in this chapter will provide additional detail on the history and motivation behind the development and testing of the X2. Chapter III provides an overview of the NHT used for all experiments and measurements. Chapter IV describes the design of the conducted research, including the plasma diagnostics, measurement techniques, and test facilities. Performance measurements on the X2 are discussed in Chapter V, while

measurements of the internal plasma and external plume are featured in Chapter VI. The integration of the plume measurements with efficiency models will show how dual-channel operation affects the efficiency and performance of the X2, as discussed in Chapter VII. Chapter VIII concludes this work with a summary and suggestions for future work.

CHAPTER II

Background

The discussion of the capabilities and properties of nested Hall-effect thrusters requires first an overview of background information on electric propulsion and Hall-effect thrusters. This chapter provides the necessary information to understand the motivation behind the development of the X2 NHT as well as the experimental results shown in the following chapters. Aside from Hall-effect thrusters, there exist many other useful and interesting propulsion technologies, but this chapter will not treat these alternatives in great detail. Other resources include References [9–13].

Section 2.1 is an overview of fundamental propulsion parameters that are used to evaluate EP devices such as the X2. A brief background in high-power electric propulsion will be provided in Section 2.2, and additional details on Hall-effect thrusters and clusters in Sections 2.3 and 2.4, respectively.

2.1 Fundamental Performance Parameters

Quantifying the performance of electric thrusters typically requires a number of measured and calculated parameters. Thrust stands and flow meters typically provide direct measurements of thrust T and propellant mass flow rate $\dot{m}$, respectively. These two parameters can then yield two important metrics of electric rocket performance: the specific impulse I_{sp} and the total efficiency η_t.

The specific impulse is a metric for how effectively a thruster is utilizing propellant to generate thrust. Equation 2.1 shows the general formulation of I_{sp} as the ratio of the total impulse to total propellant mass consumed over a period of time t_1 to t_2. For constant thrust and mass flow rate, the calculation of specific impulse simplifies to Equation 2.2. Dividing by the standard gravitational acceleration at sea level g_0 turns the units of I_{sp} into seconds, thereby avoiding conflicts between imperial and metric unit systems.

$$I_{sp} = \frac{\int_{t_1}^{t_2} T dt}{g_0 \int_{t_1}^{t_2} \dot{m} dt} \tag{2.1}$$

$$I_{sp} = \frac{T}{\dot{m} g_0} \tag{2.2}$$

Figure 2.1 shows some examples of flight propulsion devices with their rated specified specific impulse and thrust. The same parameters for experimental ion and Hall-effect thrusters are also shown to illustrate future directions in this performance space. Chemical propulsion, including bipropellant and monopropellant engines, generates much higher thrust than state-of-the-art electric propulsion devices, which include electrothermal thrusters (resistojets and arcjets) and electrostatic thrusters (ion thrusters and Hall-effect thrusters). On the other hand, electric propulsion delivers significantly higher specific impulse along with a wider range of I_{sp} capability. Continuing research in EP pushes the the thrust and I_{sp} capabilities of Hall-effect and ion thrusters with higher power, improved efficiency, and variability in acceleration voltage.

Specific impulse is an important parameter due to its impact on the amount of propellant required to execute maneuvers. The necessary propellant for a burn, as performed with a chemical or electric propulsion device, can be calculated using the

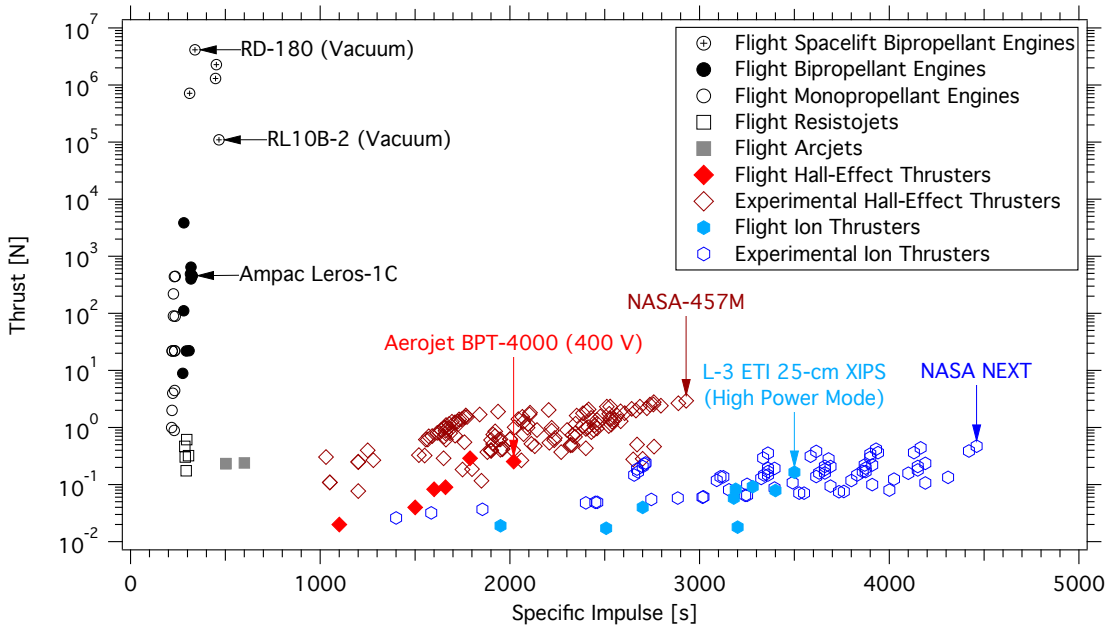

Figure 2.1: **Thrust and specific impulse of various chemical and electric flight engines along with experimental counterparts to the electric propulsion devices.** This figure includes, in particular, experimental ion and Hall-effect thrusters to illustrate the expansion in thrust and I_{sp} capability due to ongoing research.

Tsiolkovsky rocket equation, as shown in Equation 2.3.

$$\frac{m_i}{m_f} = \frac{m_f + m_p}{m_f} = \exp\left(\frac{\Delta v}{I_{sp} g_0}\right) \tag{2.3}$$

In this form, Equation 2.3 considers the engine thrust as the only applied force and neglects other external forces, such as aerodynamic drag or solar pressure. For a given maneuver requiring a velocity change Δv, the required propellant mass m_p can be calculated if the final spacecraft mass m_f and the thruster's I_{sp} are known. The rocket equation indicates that m_p can be reduced by selecting an engine with higher I_{sp}, assuming fixed Δv and m_f. This reduces the initial mass of the spacecraft m_i and can ultimately lead to sufficient mass savings that permits a step-down to a lighter, cheaper launch vehicle. Alternatively, for fixed m_i, reducing m_p with a high-I_{sp} engine allows more of the final spacecraft mass to be allocated to payload or other subsystems.

The total efficiency of an EP device is determined by the ratio of the jet power $\dot{m} v_e^2/2$ to the total input power P_t, where v_e is the effect exhaust velocity of the jet from the thruster. Using the relation $T = \dot{m} v_e$, the total efficiency η_t can be expressed in two forms in Equation 2.4. This equation displays an important relationship between the thrust-to-power ratio, T/P_t, and the I_{sp} of an electric propulsion device. Holding total efficiency constant, T/P_t and I_{sp} are inversely proportional to each other. As a result, increasing I_{sp} typically comes at the expense of T/P_t and vice-versa. This relationship will have interesting implications for HETs and NHTs.

$$\eta_t = \frac{T^2}{2\dot{m}_t P_t} = \frac{g_0}{2}\left(\frac{T}{P_t}\right) I_{sp} \tag{2.4}$$

2.2 Electric Propulsion

As the term suggests, electric propulsion utilizes electrical power to create thrust. This differs from chemical propulsion, where propulsive energy originates from the chemical bonds in propellant. However, like the vast majority of SOTA propulsion systems, electric propulsion relies on a working fluid to transfer momentum. In the case of many electric engines, this working fluid is a plasma composed of positively- and negatively-charge particles. Xenon gas is most commonly used in current spacecraft, but mercury, cesium [10], krypton [14–16], and bismuth [17,18] are among many other propellants explored by researchers across various EP devices.

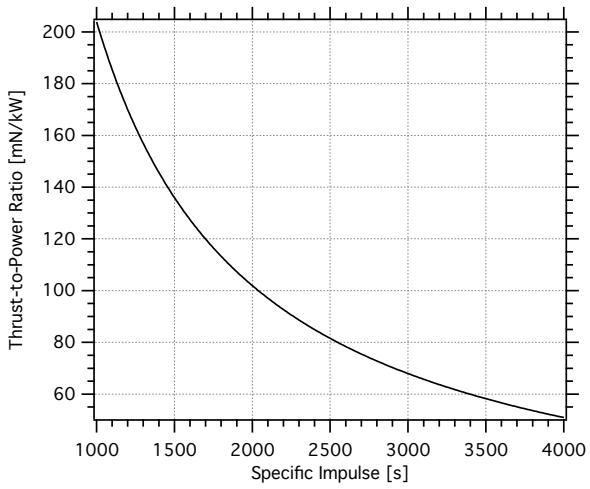

Figure 2.2: **Maximum thrust-to-power ratio over a range of specific impulse for a hypothetical 100%-efficient electric thruster.** The theoretical limit on thrust-to-power ratio makes increasing power the most effective method of increasing thrust from an EP device.

The available electrical power is one of the limiting factors in the potential performance of an electric thruster, and in order to make full use of available power, the thrust-to-power ratio should be maximized at the required I_{sp}. However, Equation 2.4 shows that, even in the case of 100% efficiency, there exists a maximum thrust-to-power ratio for any given specific impulse. Figure 2.2 illustrates the maximum T/P within a range of I_{sp} from 1000 s to 4000 s.

The implications of the theoretical T/P limit are simple. In order to obtain more thrust from an electric thruster, obtaining higher efficiency will not always be sufficient. As thrust-to-power ratio has a finite limit, scaling the device to higher power will most effectively increase the thrust. One of the most influential limitations for electric propulsion is the state of the art of the supporting power systems, as the available power greatly determines the available thrust. Additionally, for electrostatic thrusters, available voltage will determine the range of specific impulse.

To date, the flight of EP devices up to 4.5 kW has allowed communications satellites and scientific spacecraft to exploit higher I_{sp} for higher Δv capability or reduced propellant mass. NASA's Dawn mission will execute the highest propelled Δv (approximately 11 km/s) of any spacecraft in history with its NSTAR-derived ion thrusters [19]. ESA's SMART-1 launched as a secondary payload onboard an Ariane 5 and used the Snecma PPS-1350 as primary propulsion from a geosynchronous transfer orbit to lunar orbit [20]. Most recently, Boeing introduced the all-electric 702SP with the 25-cm Xenon Ion Propulsion System (XIPS) by L-3 Electron Technologies for orbit raising, stationkeeping, and momentum management [21]. The 702SP couples high-I_{sp} propulsion with a mass-optimized spacecraft, resulting in sufficient mass saving to launch two from vehicles as small as the SpaceX Falcon 9.

The application of EP at even higher powers enables the possibility of new classes of missions, including cargo tugs [22, 23], electric upper stages on launch vehicles [24], and propelled outer-planet explorers [25, 26]. Many of these high-power mission concepts offer substantial increases over the state of the art in delivered payload mass and Δv capability. One set of examples are the manned exploration architectures developed by the Human Exploration Framework Team [27]. Their summary states, "Electric propulsion is key for achieving affordable missions to an asteroid or similar long-range destinations." In this particular application, the use of high-power EP reduced the number of heavy-lift launches by a factor of 2, thereby offering both

technological and economic benefits.

Executing a high-power EP mission would first require the development of a thruster of adequate power, thrust, and specific impulse. Additionally, the power system, power processing units, gimbals, and other support equipment must also exist. Thruster lifetime must also be sufficient for such missions. Given recent and past advances in power throttling [28–30] and lifetime [31–34], HETs remain strong candidates for high-power EP missions.

2.3 Hall-Effect Thrusters

Hall-effect thrusters, also known simply as Hall thrusters or closed-drift thrusters (CDTs), come primarily in two broad types and several configurations. The two main types of HETs are traditionally known as stationary plasma thrusters (SPTs) and thrusters with anode layer (TALs). SPT-type thrusters are also known as magnetic layer thrusters. The differentiating feature between SPTs and TALs is the material used to create the discharge channel walls. SPTs have dielectric walls that are commonly made of ceramics such as boron nitride or borosil, and TALs have metallic walls. A comparison of SPTs and TALs can be found in Ref [35].

In addition to the discharge channel wall material, the channel geometry has been varied in numerous studies. The traditional configuration for the discharge channel is a simple circular annulus, which is the most relevant to this work. Other variants include linear [36], cylindrical [37], and racetrack HETs [4].

Considering the numerous variations of HETs, this study of a nested Hall-effect thruster is relatively narrow in scope. Hereafter, only magnetic layer (SPT-type) HETs with circular geometries will be relevant. Additionally, the ionization and acceleration processes will be considered single-stage, as opposed to two-stage HETs where an additional electrode can be used to control the two processes separately.

A highly simplified schematic of a Hall-effect thruster is shown in Figure 2.3.

Plasma is created in a HET by direct-current discharge via the anode and hollow cathode. The anode typically doubles as the primary propellant injector, while a small fraction of the propellant also flows through the hollow cathode. Through a self-sustaining heating process, the hollow cathode emits electrons that move toward the positively-biased anode and into the plume for neutralization. For a more thorough description of hollow cathode operation, Ref. [13] is suggested.

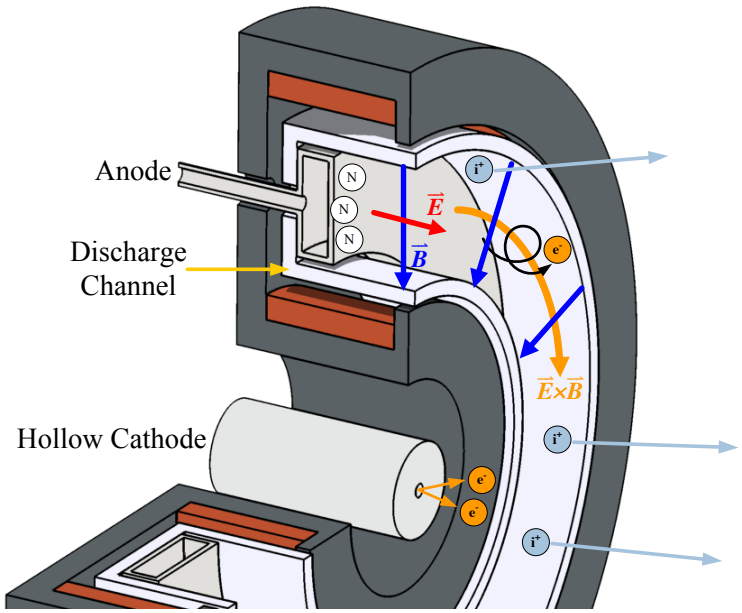

Figure 2.3: **Hall-effect thruster schematic**

Electrons that move toward the anode are magnetized by a magnetic field $\vec{B}$ that is mostly radial in direction. With a DC voltage applied between the anode and cathode, the electric field $\vec{E}$ in the discharge channel is roughly axial, resulting in crossed electric and magnetic fields near the channel exit. The magnitude of the magnetic field inside the discharge channel is sufficiently high to magnetize electrons but sufficiently low to leave accelerated ions unmagnetized. Electron motion toward the anode becomes impeded by a quasi-radial magnetic field that causes an $\vec{E}\times\vec{B}$ drift and the formation of the so-called Hall current in the discharge channel. A strong electric field forms nears the exit of the discharge channel in order to maintain current continuity [38]. Ionization of neutrals occurs by collision with energetic electrons in

the Hall current. Ions are then immediately accelerated by the electric field, thereby creating thrust by reaction force.

Figure 2.4 shows a simplified diagram of the propellant supply system for a laboratory Hall-effect thruster. Such a system supported the experiments discussed in the following chapters. State-of-the-art Hall-effect thrusters use hollow cathodes that require propellant to operate during and after ignition. For large-orifice cathodes, ion bombardment of internal surfaces allows the cathode to operate without additional power to a heater, as the heating of the emitter from bombardment is sufficient to sustain thermionic electron emission [13]. The total mass flow rate $\dot{m}_t$ into the thruster is then simply the sum of the anode mass flow rate $\dot{m}_a$ and the cathode mass flow rate $\dot{m}_c$, as shown in Equation 2.5. Typically, mass flow controllers provide fine control of the propellant flow into the anode and cathode.

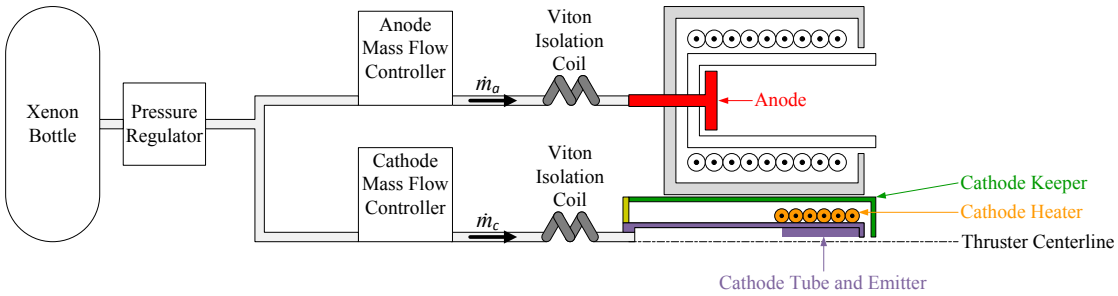

Figure 2.4: **Simplified laboratory Hall-effect thruster propellant supply system**

$$\dot{m}_t = \dot{m}_a + \dot{m}_c \tag{2.5}$$

Figure 2.5 shows a basic, minimal electrical schematic for a Hall-effect thruster. The voltage applied between the anode and cathode is the discharge voltage V_d, while the current between the anode and cathode is the discharge current I_d. Under typical operation, the discharge power supply operates under voltage control mode. As a result, I_d is indirectly controlled by the supplied propellant mass flow rate and the

magnetic field in the discharge channel.

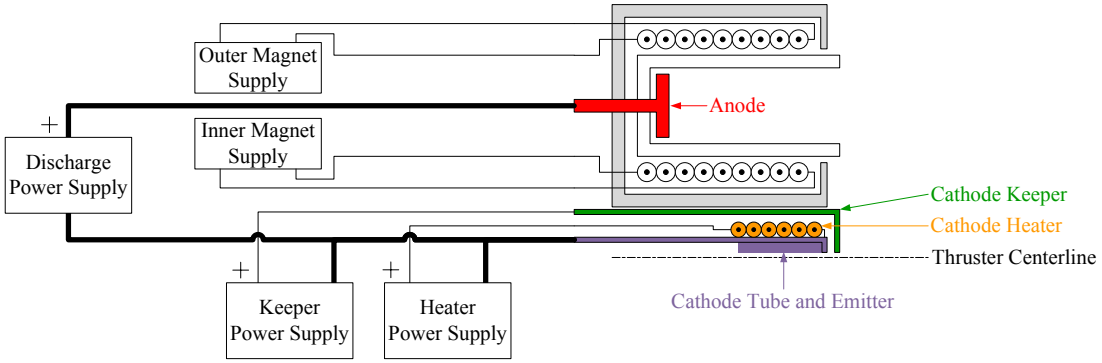

Figure 2.5: **Example Hall-effect thruster electrical schematic**

The voltage applied between the anode and cathode V_d is only partially used for ion acceleration. Some voltage is necessary to draw electrons from the cathode. This potential difference is typically measured as the cathode coupling voltage V_c and this quantity is measured against the downstream plasma potential V_p. The remaining voltage $V_d - V_c$ is available for ion acceleration, although not all of $V_d - V_c$ is necessarily used. The part of V_d that does not directly contribute to ion acceleration is considered the loss voltage [38].

As run in a laboratory setting, a HET requires a large discharge power supply to create the plasma and several smaller power supplies for the electromagnets, the cathode heater, and the cathode keeper. The total power P_t going into the thruster can therefore be broken down into its components, as shown in Equation 2.6.

$$P_t = P_d + P_{mag} + P_{htr} + P_{kpr} \tag{2.6}$$

The discharge power P_d is the power required to create and sustain the plasma between the anode and cathode. The power used for ionization and acceleration of propellant comes from the discharge power, which typically takes up a dominant percentage of the total power. The power required by the electromagnets P_{mag} varies

between operating conditions. Magnet currents are adjusted for every operating condition to maximize efficiency. During operation of the thruster, the cathode heater power P_{htr} and cathode keeper power P_{kpr} are commonly zero, as they are mostly used for the ignition process. Ignition and startup sequences will be discussed in Section 3.3.

Figure 2.6 shows a sample of HET performance data from the H6 at 20 mg/s and 7% cathode flow fraction [39, 40]. The majority of the data show that T/P_t and I_{sp} are inversely proportional, as shown in Equation 2.4. T/P_t maximizes around 1000 s, which corresponded to discharge voltages around 120 V. Below 1000 s I_{sp}, the efficiency of HETs becomes impractically low such that thrust-to-power ratio no longer increases with decreasing specific impulse.

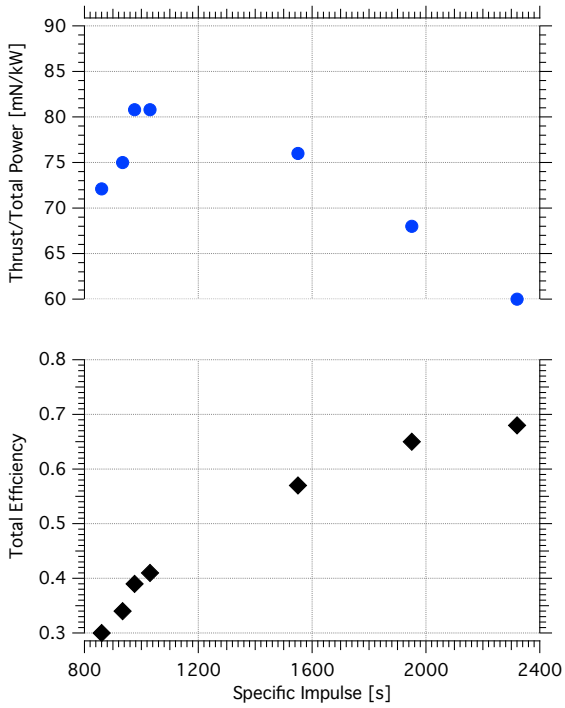

Figure 2.6: **Sample thrust-to-power ratio and total efficiency from the H6 performance tests**

These data establish an important performance characteristic common in state-of-the-art HETs. At some low discharge voltage and low specific impulse, there exists a maximum in thrust-to-power ratio. Typical HETs operate at discharge voltages of

300 V or above, so throttling to maximize T/P_t requires decreasing discharge voltage. HETs also operate near an optimal current density [41], resulting in an optimal discharge current for a fixed exit area. The net effect of decreasing V_d to maximize T/P_t is a decrease in P_d and therefore P_t, assuming I_d remains in a fixed range. Maximizing thrust-to-power ratio at low power becomes a self-defeating process, as high thrust-to-power ratio at low power does not yield high thrust.

Two potential solutions exist that would enable throttling between high T/P_t and high I_{sp} at constant power. The first is to increase the operating range of HETs in terms of discharge current, particularly above the nominal current density. The second solution is to vary the exit area such that the current density remains approximately the same. The development of HET clusters and NHTs falls into the realm of the latter.

2.4 Nested Hall-Effect Thrusters

In anticipation of future high-power EP missions, researchers in the electric propulsion community have developed methods for scaling HETs to 100 kW and above. The most explored methods are to simply increase the size of a traditional Hall-effect thruster or to cluster multiple HETs to achieve the desired total power. Clustering can be an effective method of scaling up in power without the need to develop new thrusters. The use of smaller thrusters can also simplify testing, as less capable vacuum facilities would be sufficient [3, 42]. However, the tradeoff includes an increase in complexity for the propellant supply system and the power distribution system.

Figure 2.7 shows a sampling of the HETs developed by NASA Glenn Research Center and illustrates the effect of increasing the size of HETs while maintaining the traditional, single-channel configuration. The thrusters included in the image are the NASA-120M, NASA-173Mv2, NASA-400M, and the NASA-457M. The nominal discharge power range represented in Figure 2.7 is 3 kW to 50 kW. The higher-power

HETs in Figure 2.7 have large overall footprints with cylindrical voids at the center. Though useful for mounting an internal cathode, this unused space can become sufficiently large to fit another thruster inside. This naturally leads to the concept of nested Hall-effect thrusters. One could even entertain the possibility of nesting different propulsion devices within a high-power HET, but the concept of heterogeneous nested thrusters is beyond the scope of this work.

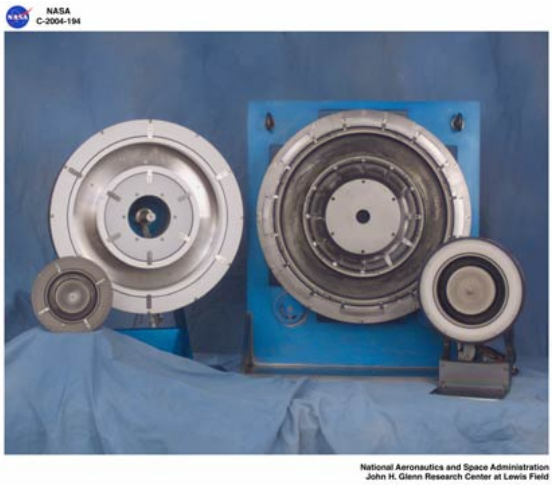

Figure 2.7: **Hall-effect thrusters developed by NASA ranging from 3 kW to 50 kW nominal power. Photo courtesy of NASA.**

The idea of nested Hall-effect thrusters has existed since, at the latest, 1986 when Pekshev and Suslov reported on a three-channel NHT. Reference [43] provides a brief overview of this thruster which uses the separate phases of three-phase AC current to power each of the channels. NHT concepts that operated in a more traditional manner were studied by NASA Glenn Research Center in 2005 and the Busek Company in 2006 [6,44]. United Technologies Corporation also considered the NHT configuration [45]. In 2011, Busek reported the demonstration of a functional NHT [46]. However, with the exception of the X2, no NHT performance or plume data are available in open literature despite the number of organizations studying the technology.

One motivation behind the development of NHTs is the desire to minimize thruster footprint and mass, especially at power above 100 kW. A study performed by Florenz,

Gallimore, and Peterson showed mass reductions up to 85% and thruster footprint reductions up to 70% by using a NHT from 100 kW past 1 MW [47]. Smaller, but still substantial, reductions in footprint and mass were reported by NASA Glenn on a 100-kW design [44]. The reductions scale proportionally with power, as single-channel HETs can become impractically large annuli at very high powers.

The closest relative to the NHT with an experimental history are clustered HETs. In particular, the work by Beal and Walker on clusters operated on shared cathodes are most relevant to the concept of NHTs [42, 48–50]. Both researchers showed that two HETs can run off of a single cathode. The geometric configurations considered include placing the cathode between the HETs and on the far side of one HET. In both cases, simultaneous operation was possible using a shared cathode, leading to the feasibility that nested operation could also be achieved with a similar electrical configuration.

2.5 Hall-Effect Thruster Efficiency Model

In addition to demonstrating the capabilities and feasibility of a NHT, this work will also examine how the X2 utilizes various inputs to produce directed thrust. Existing phenomenological models for HETs decompose the measured total efficiency into a number of contributing efficiencies, mostly called utilization efficiencies. Work by Hofer [38, 51, 52] and Brown [40, 53] serve as the basis for the efficiency model used in this work. The expressions for thrust and efficiency will be reformulated for application with NHTs. This section will begin by a review of the efficiency model for a single-channel HET and will then expand the model to NHTs.

2.5.1 Single-Channel Efficiency Model

The model for thrust, as shown in Equation 2.7, is a summation of the thrust contributions of all the present charge species of propellant. For xenon, this is a

summation of the thrust contribution for Xe^{1+}, Xe^{2+}, Xe^{3+}, and so on. The thrust for each charge species is the product of that species' ion mass flow rate $\dot{m}_i$ and mean ion velocity $\langle v_i \rangle$.

$$T = \sum_{i=1}^{N} \dot{m}_i \langle v_i \rangle \tag{2.7}$$

The *ion* mass flow rate is rarely a product of direct measurement and is instead calculated from the ion beam current I_b. Equation 2.8 gives the ith-species mass flow rate by a conversion of a flow of charge $I_{b,i}$ to a flow of mass $\dot{m}_i$ using the mass-to-charge ratio $m_{Xe}/q = m_{Xe}/eZ_i$, where m_{Xe} is the xenon ion mass, e is the elementary charge and Z_i is the integer value for the charge state. For convenience, the expression for ion mass flow rate will utilize the total beam current I_b by introducing the ith species current fraction Ω_i, as shown in Equations 2.8 and 2.9.

$$\dot{m}_i = I_{b,i} \frac{m_{Xe}}{eZ_i} = I_b \frac{m_{Xe} \Omega_i}{eZ_i} \tag{2.8}$$

$$\Omega_i = \frac{I_{b,i}}{I_b} \tag{2.9}$$

The mean exhaust velocity of the ith species $\langle v_i \rangle$ comes from conservation of energy and depends on the voltage drop $V_{a,i}$ used to accelerate ions and the divergence half-angle β_i.

$$\langle v_i \rangle = \sqrt{\frac{2eZ_i V_{a,i}}{m_{Xe}}} \cos\beta_i \tag{2.10}$$

Combining Equations 2.8 and 2.10 yields the expanded equation for thrust. Two of the essential assumptions of this model allow all but two variables to be undistributed from the summation over all charge species. The first assumption is that all charge species experience the same accelerating voltage, resulting in $V_{a,i} = V_a$. The second

assumption is that divergence angle is also independent of charge species. These allow the simplification of Equation 2.11 into Equation 2.12.

$$T = \sum_{i=1}^{N} I_b \frac{m_{Xe}}{e} \frac{\Omega_i}{Z_i} \sqrt{\frac{2eZ_i V_{a,i}}{m_{Xe}}} \cos\beta_i \tag{2.11}$$

$$T = I_b \sqrt{\frac{2m_{Xe}V_a}{e}} \cos\beta \sum_{i=1}^{N} \left(\frac{\Omega_i}{\sqrt{Z_i}} \right) \tag{2.12}$$

The decomposition of the total efficiency from Equation 2.4 into Equation 2.13 will use the expression for thrust from Equation 2.12 as well as two additional variables: anode mass flow rate $\dot{m}_a$ and the discharge power P_d. These variables are common because the anode mass flow rate typically dominates the total mass flow rate, and the discharge power is typically the majority of the total input power.

$$\eta_t = \frac{T^2}{2\dot{m}_a I_d V_d} \frac{\dot{m}_a}{\dot{m}_t} \frac{P_d}{P_t} = \frac{T^2}{2\dot{m}_a P_d} \eta_c \eta_{\text{mag}} \tag{2.13}$$

The additional efficiencies introduced are the cathode efficiency η_c and the electromagnet efficiency η_{mag}. η_c approaches unity as the propellant supplied to the cathode approaches zero, and η_{mag} approaches unity when all auxiliary components utilize zero power. η_{mag} is so named because, in many state-of-the-art HETs, only the electromagnets require steady-state power after ignition. Other auxiliary components, such as the cathode heater and cathode keeper, usually shut off after startup.

$$\eta_c = \frac{\dot{m}_a}{\dot{m}_t} \tag{2.14}$$

$$\eta_{\text{mag}} = \frac{P_d}{P_t} \tag{2.15}$$

The first ratio in Equation 2.13 is known as the anode efficiency η_a, as reiterated in Equation 2.16, and typically dominates η_t. Many evaluations of laboratory Hall-

effect thrusters utilize η_a instead of η_t because η_c and η_{mag} are not always maximized during the design process. In the case of the X2, an existing cathode was essentially borrowed from another HET, and the electromagnets were sized for compatibility with available laboratory power supplies. Due to these reasons, all performance data for the X2 will use anode efficiency instead of total efficiency.

$$\eta_a = \frac{T^2}{2\dot{m}_a P_d} \tag{2.16}$$

In a similar manner to efficiency, specific impulse can be expressed as the product of an "anode" quantity (anode specific impulse $I_{sp,a}$) and an auxiliary efficiency (cathode efficiency), as shown in Equations 2.17 and 2.18. As the anode mass flow rate usually dominates the total mass flow rate, anode specific impulse closely approximates specific impulse with a difference that is usually within 10%. Anode specific impulse is another performance parameter under common usage for laboratory Hall-effect thrusters. The performance data on the X2 will show anode specific impulse for the same reasons anode efficiency is used.

$$I_{sp,a} = \frac{T}{\dot{m}_a g_0} \tag{2.17}$$

$$I_{sp} = \frac{T}{\dot{m}_a g_0}\frac{\dot{m}_a}{\dot{m}_t} = I_{sp,a}\eta_c \tag{2.18}$$

By combining Equations 2.12 and 2.13 and introducing the average charge Q as defined in Equation 2.19, the total efficiency can be decomposed into the various utilization efficiencies.

$$Q = \left(\sum_{i=1}^{N} \frac{\Omega_i}{Z_i}\right)^{-1} \tag{2.19}$$

$$\eta_t = \left(\frac{I_b}{I_d}\right)\left(\frac{I_b m_{Xe}}{\dot{m}_a e Q}\right)\left(\frac{V_a}{V_d}\right)(\cos\beta)^2\left[Q\left(\sum_{i=1}^{N}\frac{\Omega_i}{\sqrt{Z_i}}\right)^2\right]\eta_c\eta_{\text{mag}} \tag{2.20}$$

$$\eta_t = \eta_b\eta_m\eta_v\eta_d\eta_q\eta_c\eta_{mag} \tag{2.21}$$

Each factor enclosed in parentheses is one of the utilization efficiencies. Aside from the cathode and electromagnet efficiencies, the remaining utilization efficiencies are:

- Current utilization efficiency η_b
- Mass utilization efficiency η_m
- Voltage utilization efficiency η_v
- Divergence efficiency η_d
- Charge utilization efficiency η_q

Current utilization efficiency η_b is the ratio of the beam current to the discharge current, as shown in Equation 2.22, and is a measure of how much of the input current is carried by thrust-producing ions. The remainder of the current is carried by electrons that make their way from the cathode to the anode. Though necessary for completing the circuit between the electrodes, these electrons do not directly produce thrust and resistively heat the anode, resulting in power loss.

$$\eta_b = \frac{I_b}{I_d} \tag{2.22}$$

Current utilization efficiency is determined by measurement of the ion beam current. Typically, some variant of a Faraday probe is employed to measure a spatial distribution of ion current density in the plume of the thruster. The spatial distribution of ion current density is then integrated to determine a total ion beam current.

In this work, the form of Faraday probe used is a planar probe injected into the near-field of the X2, as discussed in Section 4.3.

Divergence efficiency η_d is the measure of ion beam collimation and approaches unity as a greater percentage of beam ions are accelerated in the same direction. Determination of the divergence half-angle β is also typically performed by spatial measurement of the ion current density distribution. η_d is then determined from β as:

$$\eta_d = [\cos(\beta)]^2 \tag{2.23}$$

Voltage utilization efficiency η_v is the fraction of the discharge voltage used for acceleration of ions, as described in Equation 2.24. The remainder of the applied voltage is considered the loss voltage and includes the voltage required to extract electrons from the cathode. η_v approaches unity as ions are accelerated by a greater percentage of the applied discharge voltage. In order to calculate voltage utilization efficiency, the accelerating voltage V_a is determined by a Retarding Potential Analyzer (RPA) with an adjacent Langmuir probe. Section 4.2 will discuss the details behind the determination of the accelerating voltage.

$$\eta_v = \frac{V_a}{V_d} \tag{2.24}$$

Mass utilization efficiency is the fraction of the propellant mass flow rate supplied to the anode that is converted into thrust-producing ions, as described in Equation 2.25. η_m is the only parameter that is not directly measured by a probe but uses FP and E×B measurements to estimate the ion mass flow rate. The ion beam current, $I_b = I_d\eta_b$, is converted into mass flow rate by the mass-to-average charge ratio of ions, m_{Xe}/eQ.

$$\eta_m = \frac{m_{Xe} I_d}{\dot{m}_a e} \eta_b \sum_{i=1}^{N} \frac{\Omega_i}{Z_i} = \frac{m_{Xe} I_b}{\dot{m}_a e Q} \tag{2.25}$$

Charge utilization efficiency η_q quantifies the efficiency loss due to the creation and acceleration of multiply-charged ions. As expressed in Equation 2.26, η_q is unity when all ions are singly-charged. Determination of the species current fractions Ω_i typically employs an E×B probe, as discussed in Section 4.2.

$$\eta_q = \frac{\left(\sum_{i=1}^{N} \frac{\Omega_i}{\sqrt{Z_i}}\right)^2}{\sum_{i=1}^{N} \frac{\Omega_i}{Z_i}} = Q \left(\sum_{i=1}^{N} \frac{\Omega_i}{\sqrt{Z_i}}\right)^2 \tag{2.26}$$

2.5.2 NHT Efficiency Model

Development of a new efficiency model for a NHT comes from the ability to measure beam currents and divergence angles for each channel of the X2 while in dual-channel mode. With the introduction of channel-dependent I_{b_k} and β_k, an updated method of integrating these variables into utilization efficiencies became necessary. This model will treat each k-th channel as an individual thrust source but will include some constraints and assumptions. These assumptions include:

- All anodes are biased to the same discharge voltage with respect to a common cathode or cathodes at the same floating voltage. The former cathode case applies to the X2.
- The accelerating voltage, as a result of the uniform V_d, is the same for all channel and all charge species: $V_{a_{i,k}} = V_a$.
- The current fractions for the various species are the same for all channels: $\Omega_{i,k} = \Omega_i$.
- The divergence half-angle remains independent of species but is allowed to vary between channels: $\beta_{i,k} = \beta k$.

For nested Hall-effect thrusters, the model for thrust becomes the summation of the thrust contributions from N charge species originating from M discharge channels.

$$T = \sum_{k=1}^{M} \left(\sum_{i=1}^{N} \dot{m}_{i,k} \langle v_{i,k} \rangle \right) \tag{2.27}$$

The ion mass flow rate becomes dependent on the beam current from each channel I_{b_k}, and the expression for mean velocity remains nearly the same.

$$\dot{m}_{i,k} = I_{b_k} \frac{m_{Xe} \Omega_{i,k}}{e Z_i} \tag{2.28}$$

$$\langle v_{i,k} \rangle = \sqrt{\frac{2 e Z_i V_{a_{i,k}}}{m_{Xe}}} \cos\beta_{i,k} = \sqrt{\frac{2 e Z_i V_a}{m_{Xe}}} \cos\beta_{i,k} \tag{2.29}$$

The NHT multi-channel thrust, in the most general form, becomes:

$$T = \sqrt{\frac{2 m_{Xe}}{e}} \sum_{k=1}^{M} \left(\sum_{i=1}^{N} I_{b_k} \sqrt{V_{a_{i,k}}} \cos\beta_{i,k} \frac{\Omega_{i,k}}{\sqrt{Z_i}} \right) \tag{2.30}$$

Assuming the V_a is constant for all charge species and all channels allows the acceleration voltage to be undistributed. However, if discharge voltages between channels are unequal, the acceleration voltage must remain inside the summation over all channels. In the case of unequal V_a, the voltage utilization efficiency would not appear as a factor of the total efficiency, because V_{a_k} would remain distributed in $(\sum I_{b_k} \sqrt{V_{a_k}} \cos\beta_{i,k})^2$.

$$T = \sqrt{\frac{2 m_{Xe} V_a}{e}} \sum_{k=1}^{M} \left(I_{b_k} \sum_{i=1}^{N} \frac{\Omega_{i,k}}{\sqrt{Z_i}} \cos\beta_{i,k} \right) \tag{2.31}$$

The assumption of channel-independent current fractions permits the summation over charge species to be a separate factor of the summation over all channels. In Section 6.1, plume data will show that this assumption is correct within 0.02.

Species-independent divergence half-angles, as assumed in the single-channel model, completes the separation of both summations, as shown in Equation 2.32.

$$T = \sqrt{\frac{2m_{Xe}V_a}{e}} \left(\sum_{k=1}^{M} I_{b_k} \cos\beta_k \right) \left(\sum_{i=1}^{N} \frac{\Omega_i}{\sqrt{Z_i}} \right) \tag{2.32}$$

Only two terms became truly coupled in the NHT-variant of the thrust equation: beam current and divergence half-angle. In Section 6.2, measurements will show that divergence half-angle can vary up to 6 degrees between channels and may not always be considered a channel-independent variable. Beam current will naturally vary significantly in a NHT if all discharge channels operate at comparable current densities. For convenience, the product of the two variables for the k^{th} channel will be called the *axial beam current* I_{A_k}, and its sum over all channels will be the *combined axial beam current* I_A.

Using the formulation of thrust given by Equation 2.32, the decomposition of total efficiency for a NHT can proceed. The total efficiency, as shown in Equation 2.33, is a function of the combined anode mass flow rate $\sum \dot{m}_{a_k}$ and the combined discharge power $\sum P_{d_k}$. As a result, cathode and electromagnet efficiencies undergo slight modification with the addition of summations over all channels.

$$\eta_t = \frac{T^2}{2 \sum \dot{m}_{a_k} \sum P_{d_k}} \frac{\sum \dot{m}_{a_k}}{\dot{m}_t} \frac{\sum P_{d_k}}{P_t} = \eta_a \eta_c \eta_{\text{mag}} \tag{2.33}$$

The NHT anode efficiency then expands and simplifies into Equation 2.34 with the assumption that discharge voltage is equal throughout all channels.

$$\eta_a = \left(\frac{\sum I_{b_k} \cos\beta_k}{\sum I_{d_k}} \right) \left(\frac{V_a}{V_d} \right) \left(\frac{m_{Xe} \sum I_{b_k} \cos\beta_k}{eQ \sum \dot{m}_{a_k}} \right) \left[Q \left(\sum_{i=1}^{N} \frac{\Omega_i}{\sqrt{Z_i}} \right)^2 \right] \tag{2.34}$$

$$\eta_a = \eta_{b_A}\eta_v\eta_{m_A}\eta_q \tag{2.35}$$

As shown in Equations 2.34 and 2.35, the voltage and charge utilization efficiencies remain the same, while current and mass utilization efficiencies effectively absorb the divergence efficiency. The coupling of beam current and divergence half-angle create what will be called the *axial mass utilization efficiency* η_{m_A} and the *axial current utilization efficiency* η_{b_A}. η_{m_A} describes the degree of conversion of mass flow through the anode into *axial* ion mass flow in the plume. In a similar manner, η_{b_A} becomes the fraction of the discharge current converted into *axial* ion current. These efficiencies are reiterated separately in Equations 2.36 and 2.37.

$$\eta_{m_A} = \frac{m_{Xe}\sum I_{b_k}\cos\beta_k}{eQ\sum \dot{m}_{a_k}} = \frac{m_{Xe}I_A}{eQ\dot{m}_a} \tag{2.36}$$

$$\eta_{b_A} = \frac{\sum I_{b_k}\cos\beta_k}{\sum I_{d_k}} = \frac{I_A}{I_d} \tag{2.37}$$

2.6 Summary

This chapter provided an overview of Hall-effect thrusters and the motivation for the use of a nested Hall-effect thruster. High-power electric propulsion creates opportunities for new classes of space missions, and the nested Hall-effect thruster is one technology that can provide the maneuvering capability that new missions require. Various organizations considered the use and development of NHTs in the past, but limited data exist on the potential capabilities of NHTs.

The work that follows will use the fundamental performance parameters and Hall-effect thruster efficiency architecture outlined in this chapter. These are existing methods of quantifying the performance of HETs and gaining further insight on processes occurring within the thruster. Measurements of thrust and various plasma

parameters will yield the various utilization efficiencies that compose the total efficiency of the thruster.

CHAPTER III

The X2 Nested Hall-Effect Thruster

The X2 nested Hall-effect thruster belongs to the fourth generation of HETs developed at the Plasmadynamics and Electric Propulsion Laboratory (PEPL) in collaboration with external partners. In the case of this project, sponsorship began with the Air Force Research Laboratory and later folded into the Michigan/Air Force Center of Excellence in Electric Propulsion (MACEEP) under the Air Force Office of Scientific Research (AFOSR). The Air Force Research Laboratory and the Jet Propulsion Laboratory (JPL) also provided support for the LaB_6 cathodes used on the X2.

This chapter provides a description of the X2 nested Hall-effect thruster and the manner in which it was used during testing. Section 3.1 begins with the development of the X2 and modifications made during experiments. Section 3.2 describes the operating modes of the X2, and thruster operation and visual characteristics are described in Section 3.3. Lastly, support equipment used for the thruster are described in Section 3.4.

3.1 X2 Development

Development of the X2 began with some relatively simple objectives:

- Design and fabricate a relatively inexpensive, sub-scale NHT demonstrator

- Determine if the concept does (or does not) function as a viable space propulsion device
- Determine NHT performance capabilities
- Identify unique operating characteristics

For the exploration of an untested concept, the design of the X2 emphasized simplicity while leveraging past experience. Two concentric discharge channels form the most basic NHT and minimizes the complexity of the magnetic circuit design. Design principles and lessons learned from the H6 HET were employed during the design of the X2. The H6 was collaboratively developed by UM, AFRL, and JPL and became the testbed for multiple studies on HET physics [32–34, 39, 40, 54–59].

The design included a central cylindrical cavity for an internally-mounted hollow cathode in case both channels required separate cathodes in close proximity. However, Initial testing demonstrated that both channels could share the same internally-mounted cathode, and following the initial experiments, only a single internal cathode was used. A previous study showed that internal mounting of cathodes, as opposed to the more traditional external mounting, results in optimal efficiency [54].

The magnetic circuit of the X2 was designed to support two simultaneously operating discharge channels and therefore two simultaneous magnetic lens topologies, as shown in Figure 3.1. The use of this magnetic field topology was based off of previous work on HETs [12, 38, 41]. In order for quasi-radial magnetic fields to form across both channels, the magnetic field direction flipped between channels. As a result, a cusp forms at the middle pole, and the Hall currents formed by both channels counterrotate due to the switch in $\vec{E} \times \vec{B}$ directions. During the experiments conducted for this work, the radial magnetic field direction pointed radially inward for the inner channel and radially outward for the outer channel. The choice of these directions was strictly for convenience and was otherwise arbitrary.

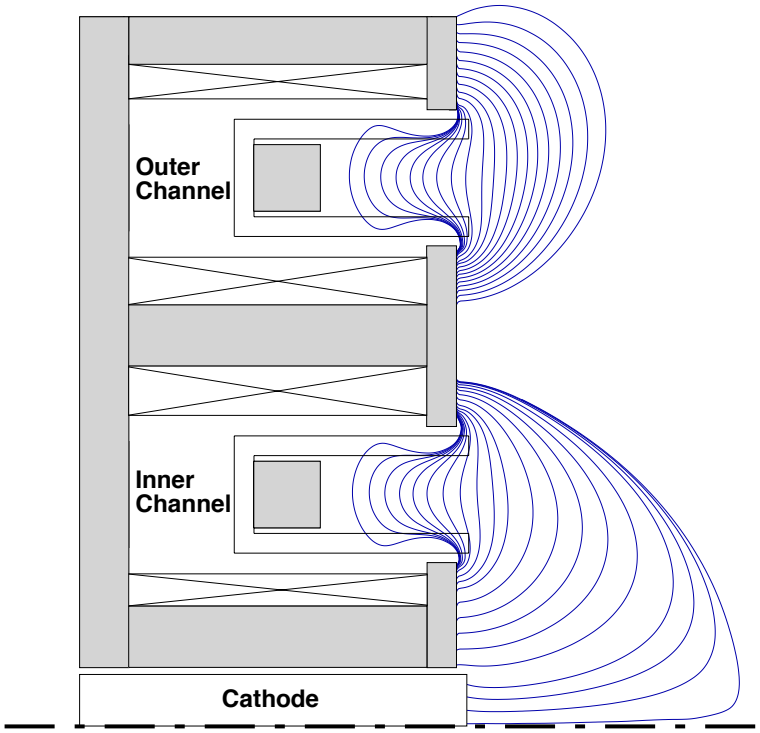

Figure 3.1: **X2 design magnetic field topology**

The X2 remained in the configuration shown in Figure 3.2(a) for the majority of the experiments shown in this work. This initial configuration featured no external protection for the magnetic circuit. However, during the final set of experiments, metallic deposits were found underneath one of the diffusers of the outer-channel anode. These deposits built up over time and began to introduce nonuniformities in the outer discharge. The origin of the deposits were traced to the front poles, although the exact transport mechanism remains unknown. To provide a sacrificial layer of protection, the X2 underwent modification with a boron nitride spray coat, as shown in Figure 3.2(b).

The Air Force Research Laboratory and the Jet Propulsion Laboratory (JPL) provided the LaB_6 cathodes used on the X2. Goebel and Watkins give a thorough description of these hollow cathodes in Ref. [60]. The first LaB_6 cathode used on the X2 had a graphite cathode tube and already underwent several years of HET testing before the X2. Unfortunately this first cathode needed replacement after

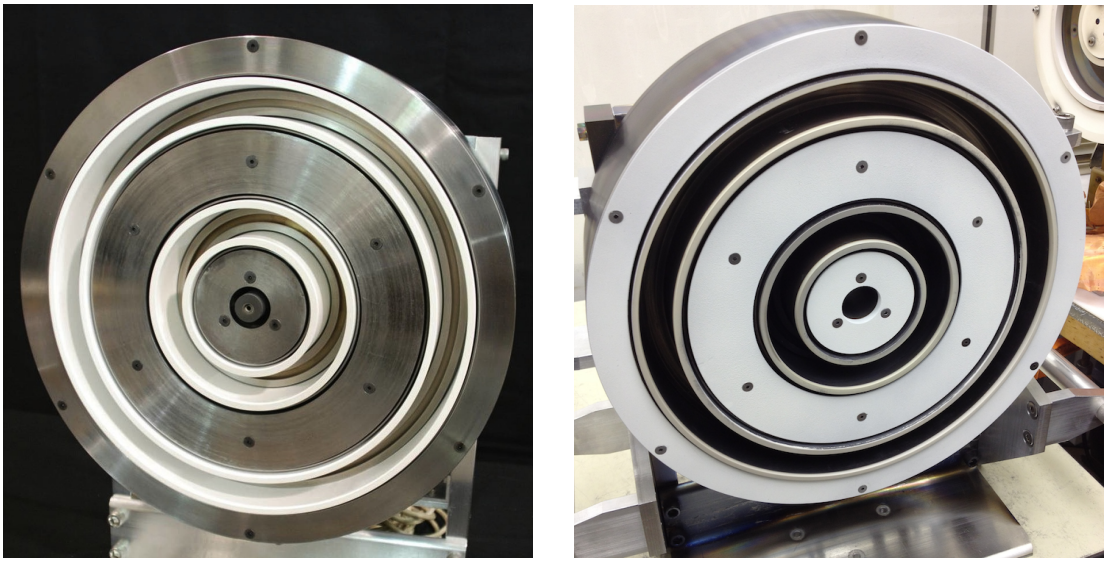

(a) Initial (b) Modified

Figure 3.2: **X2 after initial assembly and after modification to pole surfaces**

approximately 25 hours of testing on the X2, and an updated version of the LaB_6 cathode with a refractory tube was used afterwards. Initially installed with a sheathed heater, the second cathode required a heater change during the final experiments for this work. The new heater was based on a design by Goebel [60] with a filament material suggested by Michael McDonald. Shown in Figure 3.3, the bifilar heater filament was made of rhenium and was held in place by a double-threaded boron nitride sleeve.

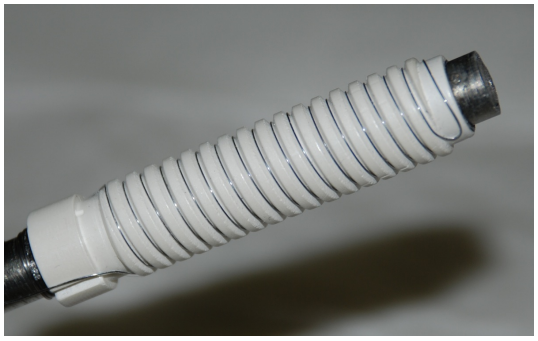

Figure 3.3: **Updated heater on the second LaB_6 cathode.**

3.2 Operating Modes

The X2 had three distinct operating modes used in this work. Two of those modes were typical for HET operation and were comprised of the inner-channel mode and outer-channel mode. In both cases, only one of the discharge channels were firing. The X2's most unique feature was the dual-channel mode, where both channels fired simultaneously on a shared internal cathode. Each mode offered different channel exit areas, allowing different mass flow rate ranges to be available.

One of the desired capabilities for the X2 was operation over a wide range of I_{sp} at constant power by utilizing the multiple exit areas to expand the range of mass flow rates. Figure 3.4 illustrates the constant-power throttling scheme where the inner channel serves as the high-I_{sp} mode and both channels serve as the low-I_{sp}, high T/P mode. Discharge voltage is the primary means of changing specific impulse. At low discharge voltage, the increased mass flow rate drives up the discharge current in order to maintain constant power, and the opposite applies for high-voltage conditions. HET efficiency is known to maximize at a certain flow rate (or current density) [41,61], so for each channel of a NHT, an optimal mass flow rate is expected to exist. This throttling method exploits the multiple exit areas by allowing each channel to remain near its optimal mass flow rate while using different modes to obtain different total mass flow rates.

3.3 Thruster Operation and Visual Characteristics

Operation of the X2 in single-channel mode was nearly identical to typical HET operation, while dual-channel operation of the X2 involved the addition of several adjustable parameters. Startup in any mode was performed with the required cathode heating sequence and ignition of the cathode plasma using the keeper. Propellent flow was then applied to one of the discharge channels with no applied magnetic field.

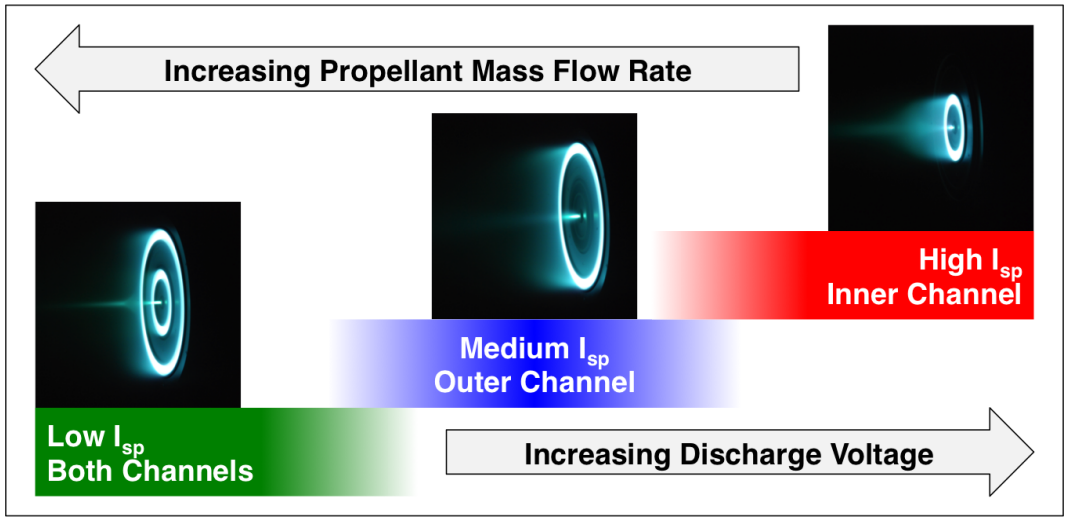

Figure 3.4: **Constant-power throttling method.**

Ignition of the first discharge channel typically occurred between 50 V and 100 V. A single-channel condition was then established regardless of the ultimate operating mode. Discharge voltage was increased to at least 150 V and the relevant magnet settings were applied to the active channel.

Dual-channel startup built upon the steps mentioned above. After reaching a predetermined single-channel condition, all four electromagnets were energized. Applying a magnetic field across the inactive channel was done for convenience, as ignition of the second channel occurred very easily with the application of 20-30 V to the second anode. The second discharge voltage could then be increased as needed. After establishing the discharge in either one or both channels, the cathode heater and keeper were typically turned off.

An alternate method of dual-channel startup is to leave the magnets off for the inactive channel while establishing a glow discharge. After breakdown occurs in the formerly inactive channel, the magnet currents can be increased until the second discharge power supply goes into voltage control. This was the sequence first used to start up the X2, as shown in Figures 3.5(a) - 3.5(d).

Tuning the X2 in both dual-channel mode and single-channel mode involved ad-

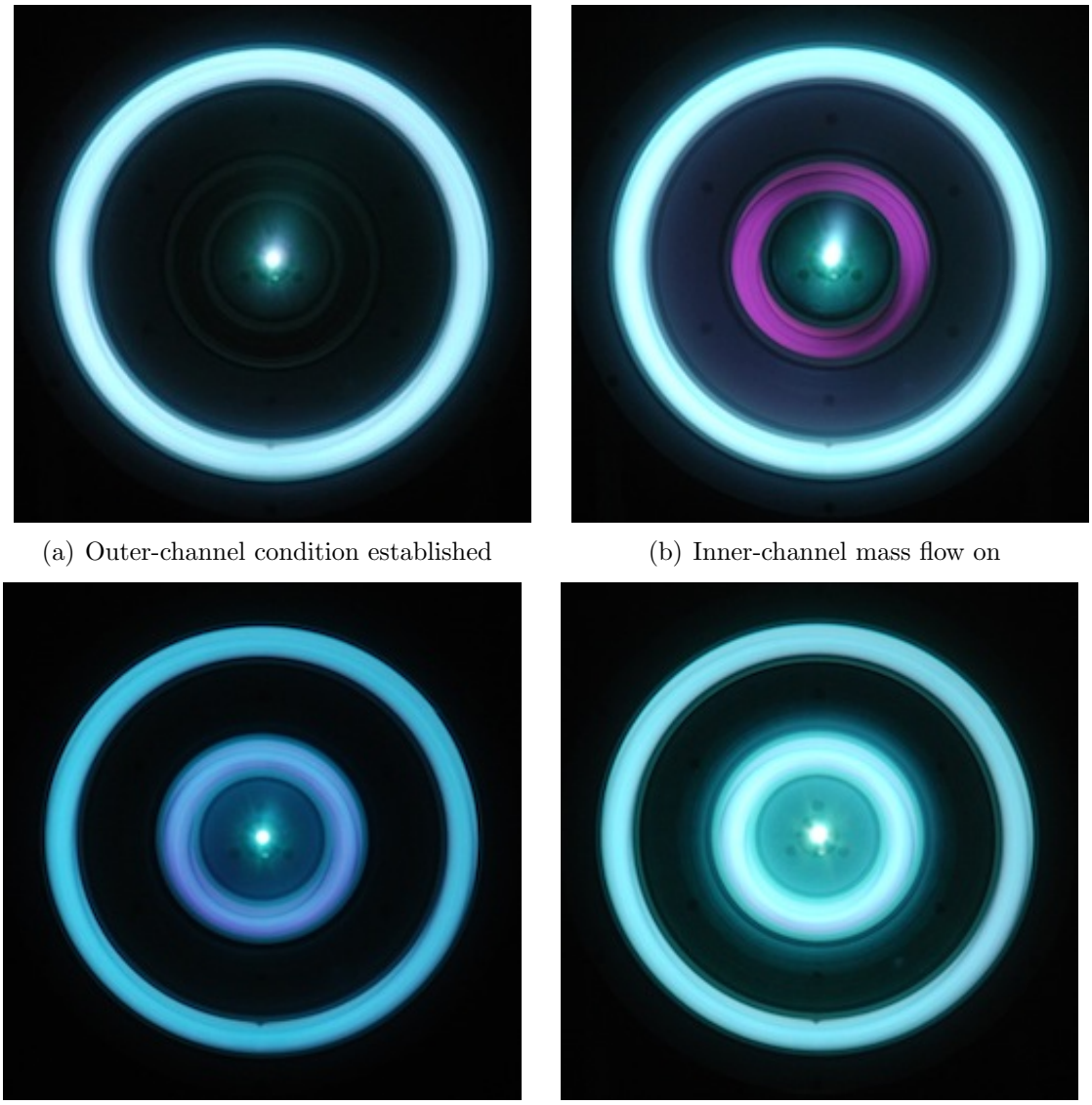

(a) Outer-channel condition established

(b) Inner-channel mass flow on

(c) Inner-channel ignition

(d) Dual-channel condition

Figure 3.5: **First startup of the X2 in dual-channel mode.** Peter Y. Peterson operated the X2 during its first ignition, and Adam Shabshelowitz captured all four phases on camera.

justing the current through each magnet in order to maximize efficiency and thrust-to-power ratio. Live monitoring of parameters that were proportional to η_a and T/P was possible with the use of the Agilent 34970A data acquisition unit. Using local minimums in discharge current to find the neighborhood of maximum η_a was not always possible, as the discharge current would sometimes plateau. In this case, the current through each magnet was increased until the discharge current stopped responding to variations in the magnetic field.

Tuning of the inner channel was typically performed using the inner and outer magnets of the inner channel, IM_1 and OM_1, and the inner magnet of the outer channel, IM_2. All four magnet coils had an influence on the performance of the inner channel, though η_a and T/P were typically maximized using only the three previously mentioned magnets. The two magnets of the outer channel behaved like external trim magnets for the inner channel.

Operation of the inner channel with three or more active magnets consistently yielded better performance than operation with only the two primary inner-channel magnets (IM_1 and OM_1). Initial attempts at stable operation of the inner channel at 400 V and above with only two magnets were unsuccessful. All subsequent tuning of the inner channel was performed with at least three active magnets: IM_1, OM_1, and IM_2.

A change in plume structure due to the number of activated magnets was also apparent, as shown in Figures 3.6(a), 3.6(b), and 3.6(c). The plume appears to be more collimated in the vicinity of the exit plane with three or more active magnets. Just downstream of the exit plane, the most luminous part of the plume forms a horn-like structure, most visible in Figure 3.6(c), before focusing to a point. A less luminous, more typical Hall thruster plume is also present in the background, though it was not captured by the camera in Figures 3.6(a), 3.6(b), and 3.6(c).

Operation of the outer channel was typically performed only with two magnets:

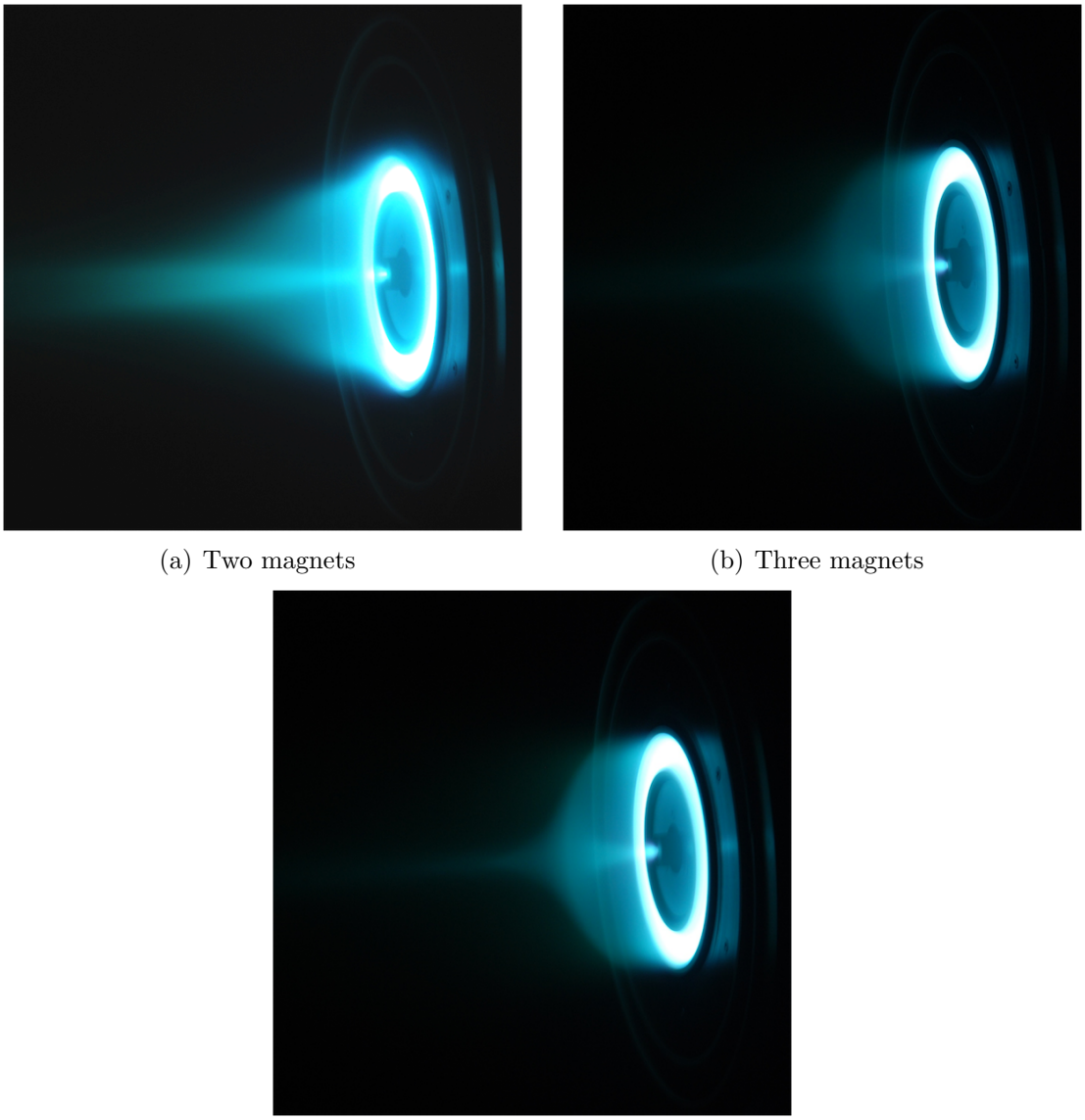

(a) Two magnets

(b) Three magnets

(c) Four magnets

Figure 3.6: **Comparison of inner channel plumes with two, three, and four activated magnets at 300 V discharge voltage**

IM_2 and OM_2. Initial attempts at using IM_1 and OM_1 resulted in instantaneous drops in anode efficiency and thrust-to-power ratio. All subsequent tuning of the outer channel was performed only with the outer channel's two magnets, except for conditions attempting to replicate the outer channel's behavior in dual-channel mode. In these cases, as shown in Section 5.1 and Chapter VI, outer-channel conditions based on dual-channel modes used all four magnets under the same current settings.

Dual-channel operation involved adjusting all four magnets, as expected. In some dual-channel conditions, anode efficiency could be maximized by minimizing both discharge currents with the magnets. However, there were also cases where increasing the current in one magnet resulted in one discharge current increasing and the other decreasing. In such cases, the magnets were still set to maximize efficiency by minimizing the sum of the discharge currents.

During dual-channel conditions, the horn-like structure seen in Figure 3.6(b) becomes even more luminous. Figure 3.7(a) and 3.7(b) show images of the X2 in dual-channel mode at 300 V and 400 V, respectively. With increasing voltage, the horn extends away from the exit plane and its edges become well-defined.

As the horn appears to be highly dependent on the applied magnetic field, a side view of the thruster was superimposed with a simulated magnetic field using MagNet 6. Figure 3.8 shows a 150-V dual-channel condition with the magnetic field lines in red. It becomes clear that the horn forms in the cusp between the inner-channel and outer-channel magnetic fields and corresponds to the separatrix surface in the magnetic field.

3.4 Support Equipment

During testing at PEPL, both anodes and the cathode had separate stainless steel propellant feed lines with viton isolators at the thruster. MKS Model 1179A mass flow controllers regulated propellant flow through the outer anode and the cathode,

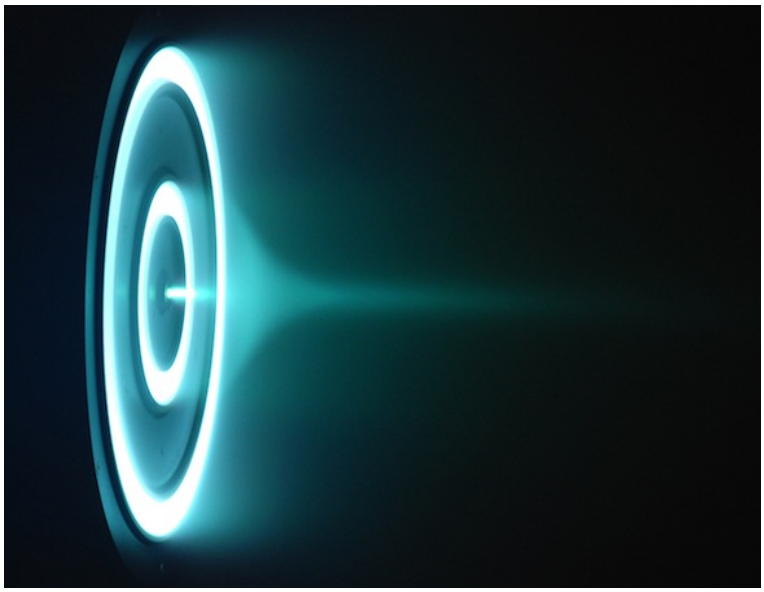

(a) 300 V, 7.0+17.4 mg/s

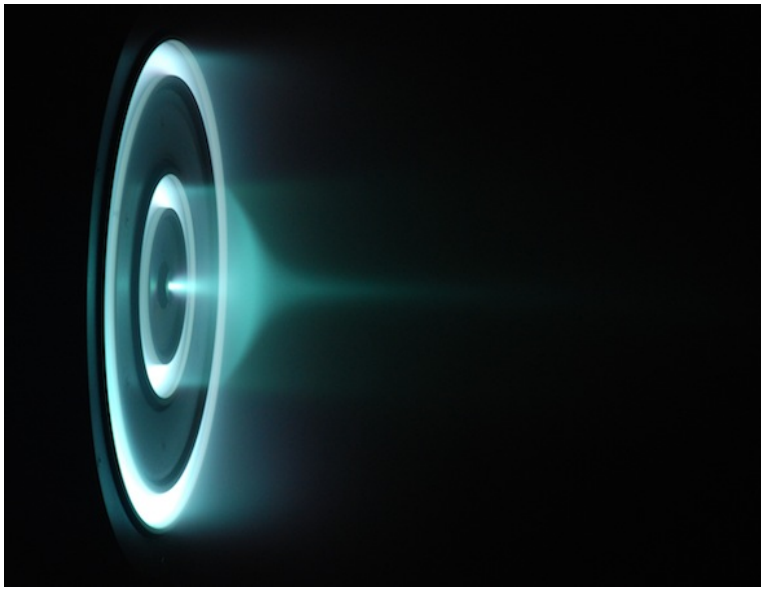

(b) 400 V, 3.9+9.4 mg/s

Figure 3.7: **Appearance of dual-channel plumes.**

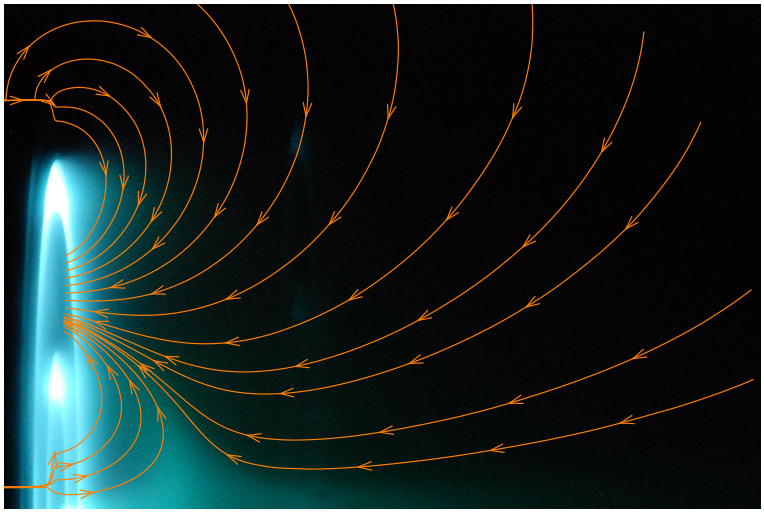

Figure 3.8: **Overlay of the simulated magnetic field with a side view of the X2.**

and an MKS Model 1159B mass flow controller was used for the inner anode. All three mass flow controllers were connected to an MKS Model 247C 4-channel readout and calibrated using a constant volume method that included compressibility effects. The manufacturer-specified accuracy of the mass flow controllers is 1% of full scale. Research grade xenon at 99.999% purity was used throughout testing.

Electrical connections for the X2 were made such that each channel had a separate discharge power supply, and the common for both discharge circuits was connected to the shared internal cathode, as shown in Figure 3.9. This electrical configuration was based on previous work performed at PEPL on clustered Hall thrusters with a shared hollow cathode [42, 62]. Operation of both channels of the X2 is also possible with a single, shared discharge power supply, as discussed in Appendix A.

The thruster was electrically grounded to the facility ground during testing, and discharge voltages were measured from contacts at the back of the X2. Measurements of the DC component of the discharge currents utilized Isotek RUG-Z current shunts. Discharge current oscillations were measured using F.W. Bell NT-series current sensors placed in series with the anodes and downstream of the discharge filter. Initially, the discharge filter included two 73-μF capacitors placed in parallel with

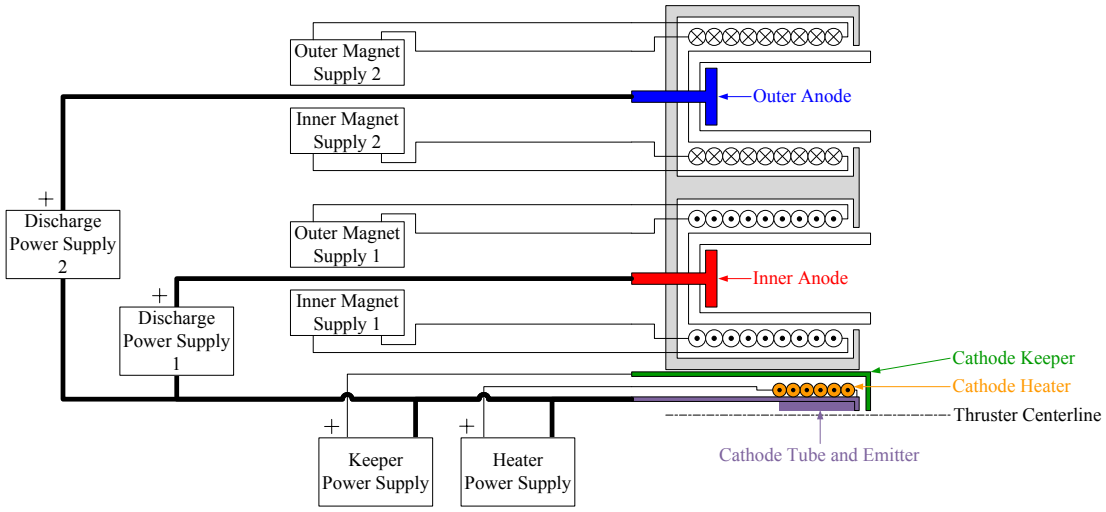

Figure 3.9: **Dual-channel NHT electrical schematic with a shared hollow cathode. The thruster is represented as a half-section.**

each discharge power supply and was later upgraded to two 220-μF capacitors. The discharge filter, current shunts, voltage dividers, and power protection diodes were housed inside a fan-cooled acrylic and fiberglass enclosure, as seen in Figure 3.10

The inner channel discharge was powered by a Sorensen PRO 600-16T while the outer channel discharge was powered by an American Reliance HPS 1000-100-K027. Power for the magnets was provided by three EMI EMS 60-10 power supplies and one EMI EMS 100-10. The two trim coils were powered by a Sorensen DCS 60-18E and a DCS 600-1.7. Cathode keeper power was provided by an EMI EMS 600-1.6, and heater power was provided by a Sorensen DCS 33-33.

3.5 Summary

This chapter summarized the design goals of the X2 along with its features and support equipment. Its operating modes permit constant-power operation over a wide range of specific impulse while utilizing all three combinations of exit area. Startup sequences for dual-channel mode were also discussed, and descriptions of the

Figure 3.10: **Enclosure housing the discharge filter, current shunts, voltage dividers, and protection diodes**

dual-channel plume were provided. Chapter IV will provide descriptions of all the measurement devices and diagnostics used during experiments.

CHAPTER IV

Experimental Apparatus

After establishing the motivation for developing a NHT in Chapter II and describing the thruster in Chapter III, a description of various instruments utilized in this NHT investigation can be given. Chapter II established that virtually no performance or plume data exist for NHTs in open literature, so as a first study on NHT performance and characteristics, many common diagnostics and techniques were employed.

Overviews of instrumentation begins in Section 4.1 with the thrust stand used for all performance measurements. The description of the plasma diagnostics begins with the far-field probes in Section 4.2 and continues with the near-field and internal probes that are described in Section 4.3. Lastly, Section 4.4 describes the vacuum facility in which all measurements occurred.

4.1 Inverted Pendulum Thrust Stand

In order to determine the feasibility of NHTs as propulsion devices, the X2 was first placed on a thrust stand to determine its performance capabilities. Thrust measurements were taken on an inverted-pendulum thrust stand designed by NASA Glenn Research Center and replicated at PEPL, as shown in Figure 4.1 [63, 64]. This type of thrust stand is sufficiently sensitive to measure thrust down to 1 mN while maintaining a compact structure. During testing, the thrust stand was operated in

null mode, where any displacement of the thrust stand's moving plate is cancelled out by an internal electromagnet assembly called a null coil. Zero displacement is maintained by closed-loop proportional-integral-derivative (PID) control with linear position of the moving plate as the input signal.

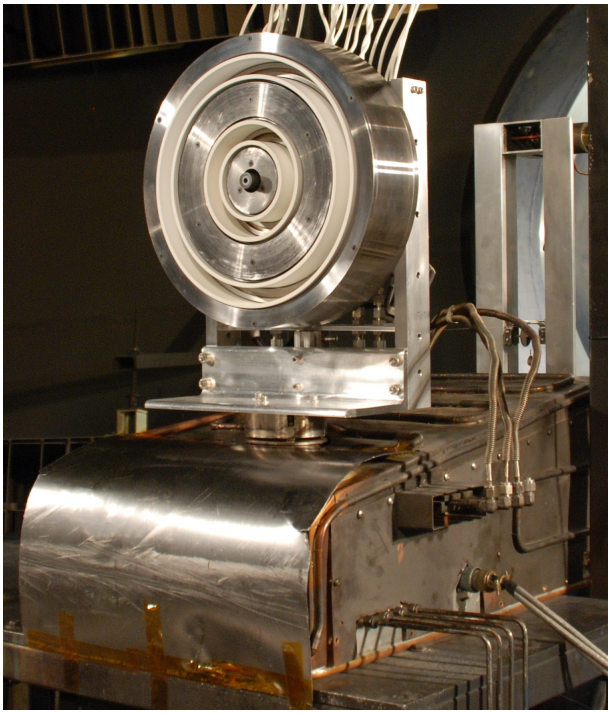

Figure 4.1: **X2 installed on the inverted-pendulum thrust stand**

Displacement of the thrust stand was measured using a Linear Variable Differential Transformer (LVDT) through a Schaevitz ATA-2001 LVDT amplifier. A single, water-cooled null coil was powered by a Trust Automation TA105 amplifier that received the control signal from a Stanford Research Systems SIM960 PID controller. The LVDT and PID output signals were recorded on a Cole-Parmer K-80550-30 flatbed recorder. The PID output signal was also recorded by an Agilent 34970A data logger for redundancy.

Calibration of the thrust stand was performed before and after each day of performance testing using fishing weights that provided a simulated full-scale thrust of 1.129 N. The calibration slope, which is the conversion fractor from the PID output

voltage to thrust, changed only by a fraction of a percent over the course of a day. The PID signal corresponding to zero thrust (the "zero") was periodically measured by shutting off all power and propellant flow to the thruster. Thrust measurements were always taken between two zeros, where the change in zero was assumed to be linear with time. At the time of a particular operating condition, the zero-thrust reference voltage was determined by linear interpolation between two zeros. The instantaneous difference between the interpolated reference voltage and the PID output voltage was converted into thrust *a posteriori* using the thrust stand calibration.

4.2 Far-Field Diagnostics

Through the use of various diagnostics, the utilization efficiencies of a HET, as discussed in Chapter II, can be calculated. These measurements provide useful information on the manner in which a HET operates. Two far-field probes were employed on the X2 to determine the distribution of ion charge states and the voltage distribution of ions. The first probe was an E×B probe, otherwise known as a Wien filter, and the second was a Retarding Potential Analyzer (RPA).

4.2.1 E×B Probe

The most basic function of an E×B probe is that of an ion velocity filter. At a given setting for the internal electric and magnetic fields, ions of all but one particular velocity are prevented from reaching a collector inside the probe, as shown in Figure 4.2. Varying the internal electric field allows ions of a range of velocities to be collected. The distribution of charge states is studied using the simple assumption that ions of higher charge states are moving faster than those at lower charge states. The inherent assumption is that all charge species experience the same accelerating potential drop.

A typical E×B measurement is shown in Figure 4.3. Groups of ions at different

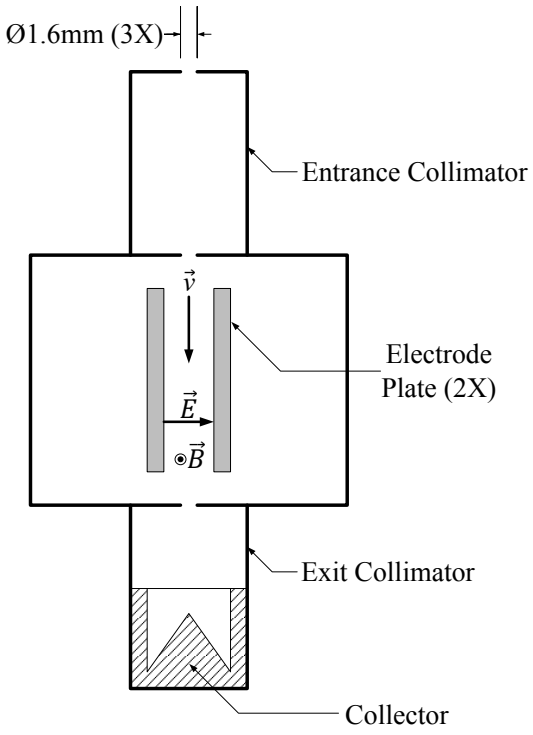

Figure 4.2: **E×B probe schematic (not to scale)**

charge states, and therefore different velocities, manifest themselves are peaks in collected current. The relative sizes of these peaks are used to determine the species fractions. The method for analysis used in this work originated from Shastry *et al* [65].

Inside an E×B probe, beam ions passing through the test section are subjected to crossed electric and magnetic fields, resulting in the application of the Lorentz force as described in Equation 4.1. Ions at a particular velocity experience a net zero force, allowing them to pass completely through the test section. An ammeter is typically attached to the collector at the back of the probe, allowing the amount of ions with that particular velocity to be quantified in the form of a current. The E×B probe used in this study was designed by NASA Glenn Research Center and is more thoroughly described in previous work by Reid *et al* [66].

$$\vec{F} = eZ\left(\vec{E} + \vec{v} \times \vec{B}\right) \tag{4.1}$$

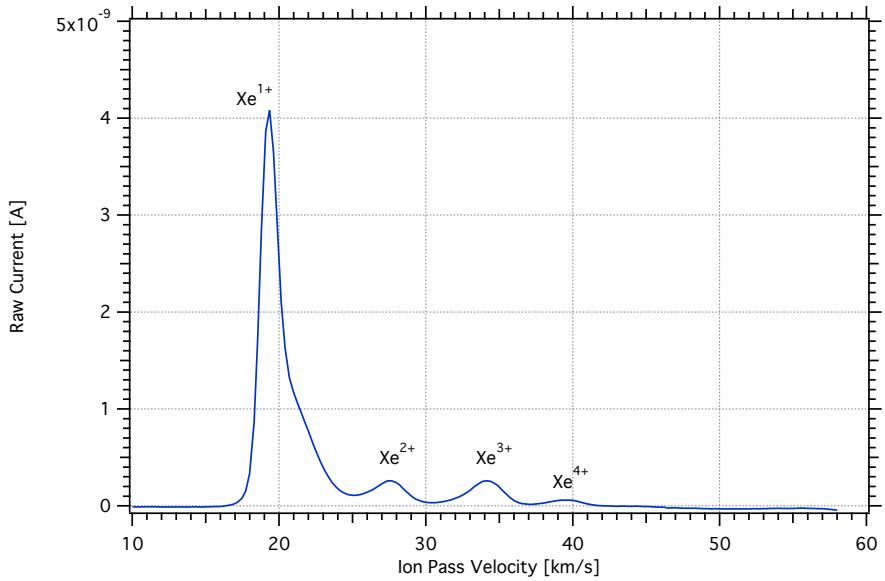

Figure 4.3: **Sample E×B measurement**

The collimators on the $E \times B$ probe obstruct most ions that do not travel axially down the length of the probe. As a result, the ion velocity $\vec{v}$, electric field $\vec{E}$, and magnetic field $\vec{B}$ form a three-dimensional, mutually orthogonal vector set, as shown in Figure 4.2. As such, Equation 4.1 can be simplified into scalar form and the force can be set to zero for ions that pass through the test section. Using the coordinate system shown in Figure 4.2, the ion pass velocity can be quantified as a simple ratio of the electric and magnetic fields.

$$v_{\text{pass}} = \frac{E}{B} = \frac{V_{\text{plate}}}{B d_{\text{plate}}} \tag{4.2}$$

The probe features a 150-mm-long test section with 75-mm-long entrance and exit collimators. Aperture diameters for the entrance orifice and the collimating orifices were all approximately 1.6 mm. The internal magnetic field was created by sintered hard ferrite permanent magnets, while the internal electric field was generated by a Keithley 2410 Sourcemeter via two parallel conducting plates. Ions that passed through the test section were collected by a cone-and-cylinder collector with a tungsten spray coat to reduce secondary electron emission. A Keithley 6485 Picoammeter

measured the current on the cone-and-cylinder collector.

4.2.2 Retarding Potential Analyzer

A retarding potential analyzer is a voltage filter and utilizes a series of grids to indirectly measure the ion voltage distribution. The first grid in the stack floats with the surrounding plasma to minimize perturbations. The second grid repels electrons from the collector so that mostly beam ions are measured by the probe, and the last grid is actively biased to filter beam ions. A cross-sectional diagram of this assembly is shown in Figure 4.4. The RPA used in this study was originally designed and built by the Air Force Research Laboratory and is described in further detail in separate documents by Reid and Hofer [38, 39].

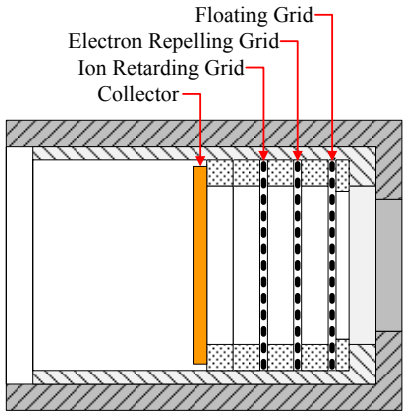

Figure 4.4: **Retarding Potential Analyzer (RPA) schematic (not to scale)**

The grids and the collector of the RPA are separated by macor spacers that are housed within a macor sleeve and stainless steel shell. In order to repel electrons, the electron repelling grid was biased to -30±0.1 V with respect to facility ground by an Kukusui PAD 110-1.5L power supply. The voltage applied to the ion retarding grid was swept relative to facility ground by a Keithley 2410 Sourcemeter, and the collected current was measured by a Keithley 6485 Picoammeter.

Figure 4.5 shows a sample measurement from the RPA for a 400-V operating

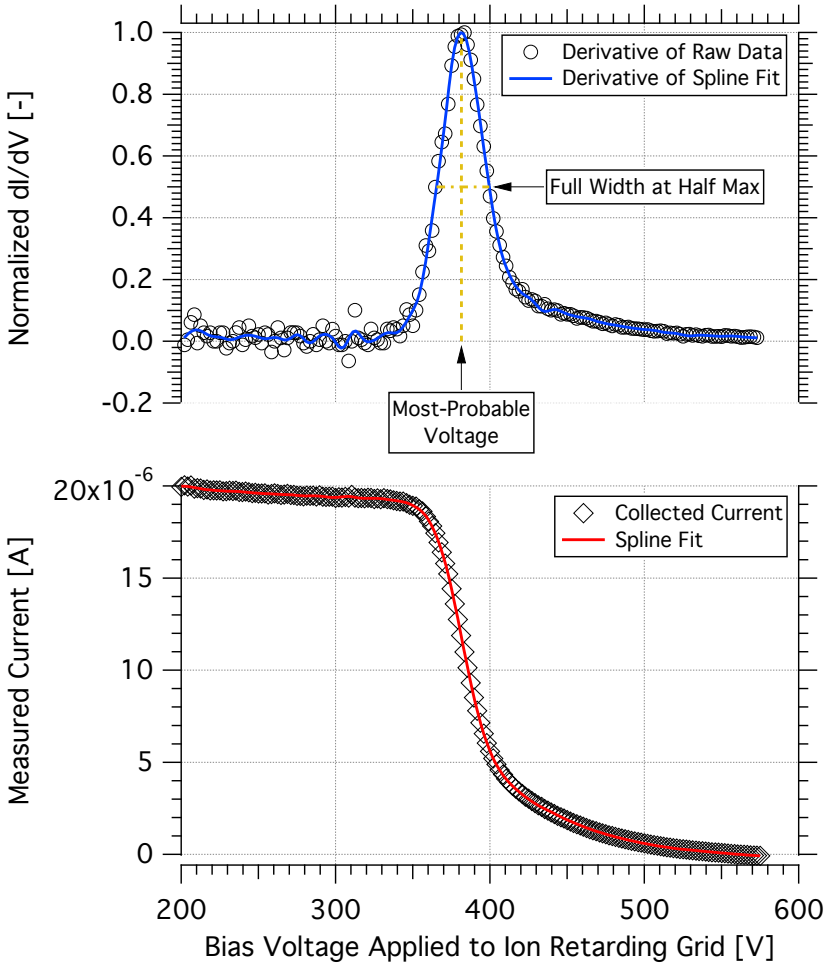

Figure 4.5: **Sample RPA measurement**

condition. At lower voltages, many ions are collected in the form of current I, and as the ion repelling voltage V approaches and exceeds the accelerating voltage, fewer ions reach the collector. The negative of the first derivative of raw data is also shown in the upper half of Figure 4.5. The peak in $-dI/dV$ occurs at the most-probable ion voltage V_{mp}. King points out that $-dI/dV$ would be proportional to the ion energy distribution as long as all ions have the same mass and possess the same charge state [67].

Measurements from the RPA often contained some noise, so analysis required some smoothing in order to obtain clean derivatives. Spline fitting yielded a smoothed I-V curve, and numerical differentiation of the spline fit generated $-dI/dV$. No smoothing occurred after differentiation in order to minimize artificial peak broadening. The lower half of Figure 4.5 shows the raw measurement and subsequent spline fit. The upper half of Figure 4.5 compares the numerical differentiation of the raw data and the fitted data.

The ion retarding voltage must be corrected for the local plasma potential in order to convert the most-probable voltage into the acceleration voltage, V_a. The voltage applied to the ion retarding grid is typically sourced with respect to facility ground, but ion acceleration occurs with respect to the downstream plasma potential. The voltage correction is a simple subtraction of the local plasma potential from the retarding grid voltage with both voltages taken with respect to facility ground.

To make this corrective measurement, a cylindrical Langmuir probe was placed adjacent to the RPA to determine the local plasma potential with respect to facility ground. The Langmuir probe was composed of a 0.25-mm diameter tungsten wire that protruded 5.7 mm from a 1.5-mm diameter alumina tube. The probe tip was biased with respect to facility ground by a Kepco Model BOP 500M bipolar operational power supply that was controlled by an Agilent 33220A waveform generator. Measurements of the bias voltage V and collected current I utilized Analog Devices

AD210BN isolation amplifiers. The measured currents at all bias voltages assemble the $I-V$ characteristic of the single, cylindrical Langmuir probe, as shown in Figure 4.6.

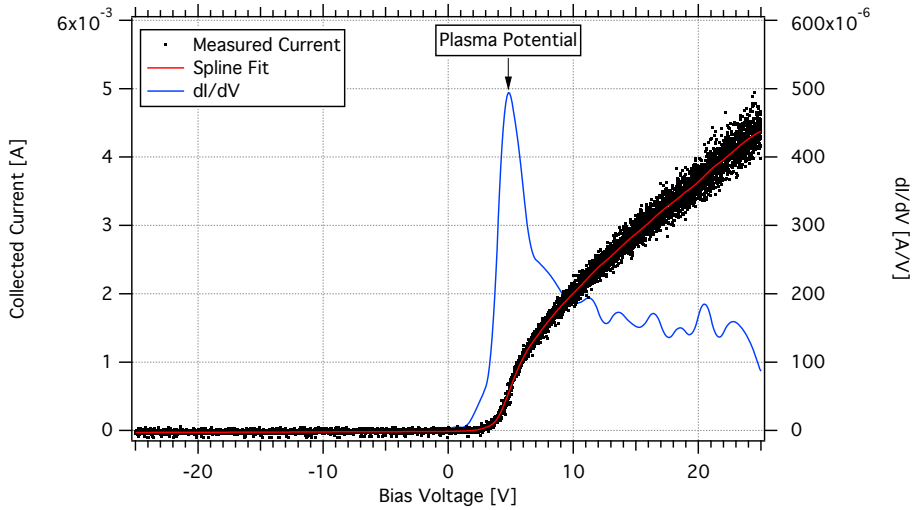

Figure 4.6: **Sample Langmuir probe measurement**

Determination of the plasma potential was performed by numerical differentiation of the spline-fitted I-V characteristic of the Langmuir probe. The voltage at the maximum dI/dV corresponds to the plasma potential V_p [68]. Prior to differentiation, the raw data underwent smoothing by boxcar averaging and then cubic spline fitting. Figure 4.6 shows sample plots of this process leading to the identification of the plasma potential.

4.2.3 Far-Field Probe Motion

The E×B probe, RPA, and Langmuir probe were placed 2.1 m downstream of the exit plane to minimize probe heating and perturbations to the thruster. The probes were vertically aligned with the thruster midplane and were radially translated to the two channel centerlines, as shown in Figure 4.7. Alignment and positioning along the channel centerline has been shown to provide accurate single-point E×B measurements with HETs [66]. This principle was applied to each channel centerline

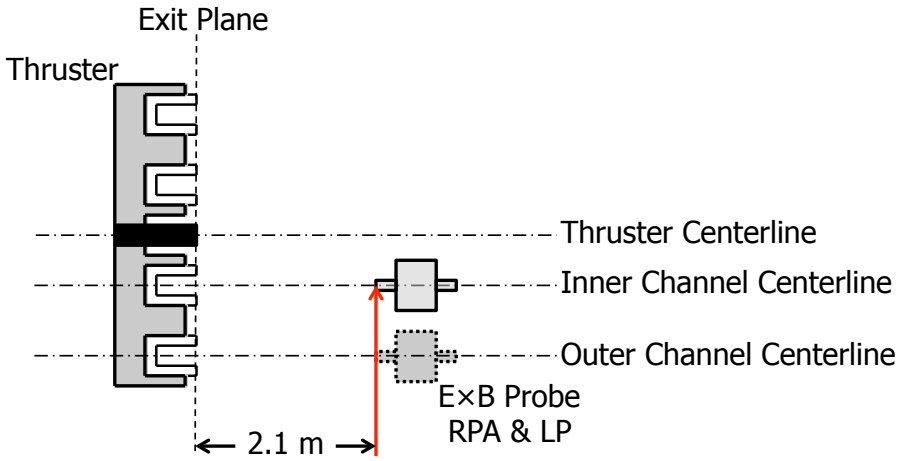

Figure 4.7: **E×B probe, RPA, and LP actuation (not to scale)**

of the X2. Measurement with the RPA occurred at these locations for consistency.

Protective devices were necessary for the longevity of the far-field probes in HET plumes. Graphite plates protected the E×B probe at its front and plume side to prevent overheating of the probe body. The RPA was protected by a grafoil shutter and the shadow of the E×B probe when the probe array was not in use.

Radial actuation was provided by a 1.5-m linear translation stage, allowing each of the probes to be placed directly downstream of the individual centerlines of the inner channel and outer channel. For all measurements using the far-field probes, the axial position did not change, although a radial positioning stage was mounted to an axial stage. The radial position uncertainty was approximately ±1 mm.

4.3 Near-Field and Internal Diagnostics

In addition to the far-field diagnostics, near-field and internal probes were utilized to gather additional information on the X2 plume and complete the evaluation of utilization efficiencies. These measurements involved the use of a high-speed positioning system that minimized the time each probe spent in the most energetic parts of the plasma.

4.3.1 High-Speed Axial Reciprocating Probe (HARP) System

All near-field and internal measurements were performed using a magnetically-driven linear actuation system known as the High-Speed Axial Reciprocating Probe (HARP). Originally developed at PEPL by Haas [69], the HARP quickly injects and retracts various probes into plasmas to minimize long-term thruster perturbations and probe heating. For the purposes of the experiments on the X2, the HARP injected probes axially toward the thruster. Figure 4.8 shows a side view of the HARP with its protective graphite shell.

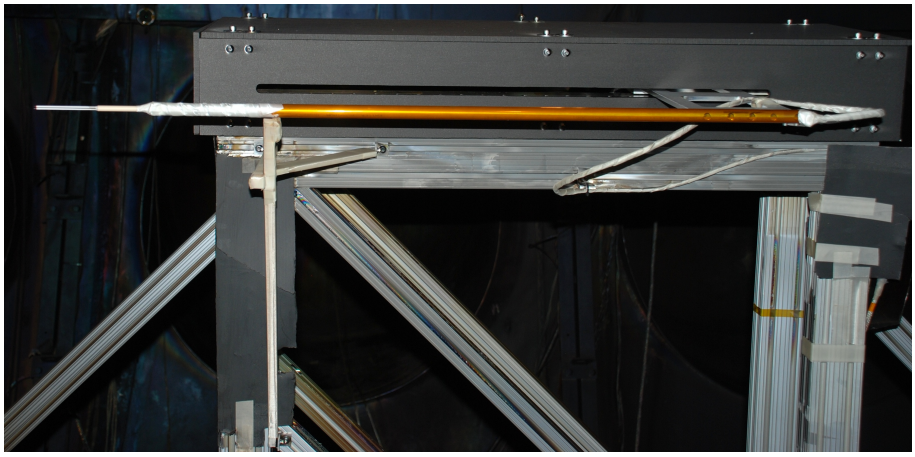

Figure 4.8: **Side view of the High-Speed Axial Reciprocating Probe (HARP) System with a double probe**

Updates have been made to the HARP hardware since the original incarnation of the positioning system. The analog encoder has been replaced by a Renishaw LM10 (1-μm option) digital encoder. The minimum resolution of the HARP position during these experiments was 0.7 mm, based on the discretization of the encoder's position signal. The HARP's magnetic linear actuator was controlled and powered by an Aerotech CP20. At the time of these experiments, the peak speed of the HARP was 2.7 m/s before the actuator began to slip at full extension.

4.3.2 Near-Field Faraday Probe

Measurements of the near-field ion current density utilized a planar, guard-less Faraday probe, as illustrated in Figure 4.9. The probe design was based off of previous work by Reid [39] with some modifications by Shastry [56] and does not feature a guard ring due to the very small sheath sizes in the near-field. The collector consisted primarily of a molybdenum disc with an outer diameter of 4.78 mm, an inner diameter of 1.55 mm, and a thickness of 0.5 mm. A tungsten rod with an outer diameter of 1.59 mm is mated to the molybdenum disc by interference fit. A telescoping pair of alumina tubes covered the length of the tungsten rod up to the aft face of the molybdenum disc. The sides and the aft face of the molybdenum disc were then covered with a ceramic adhesive (Cermabond 571) to prevent current collection on all but the front face of the collector.

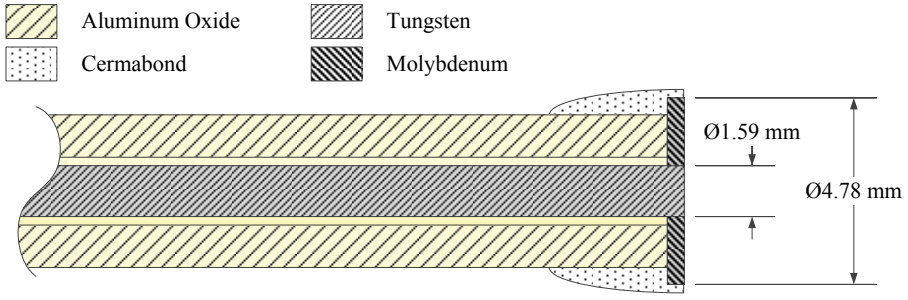

Figure 4.9: **Near-field Faraday probe construction (not to scale)**

Figure 4.10 shows an electrical schematic for the near-field Faraday probe measurement. The probe was biased to -60 V below facility ground (-54 V to -47 V below cathode floating potential) using a Kikusui PAD 110-1.5L. Ion saturation was verified by injecting the probe along the outer channel's centerline at various bias voltages. The collected current was measured using a 29.3 Ω shunt resistor placed in series with the probe. The voltage drop across the shunt was recorded by an Agilent DSO-X 3024A oscilloscope via an Analog Devices AD210BN isolation amplifier.

The method for processing the measured near-field current density was similar to

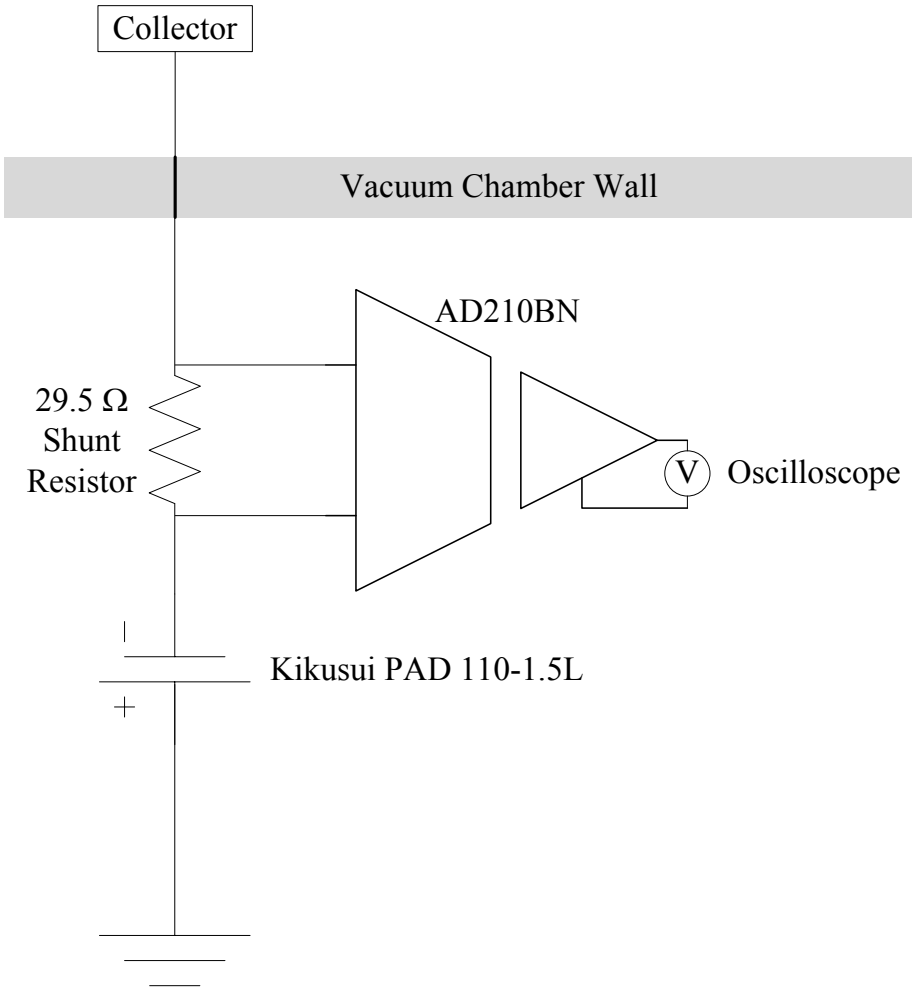

Figure 4.10: **Electric schematic for the near-field Faraday probe**

that used by Reid but with some modifications for the X2 plume geometry [39, 70]. Determination of the beam current I_b, as shown in Equation 4.3, involved the cylindrical integration of radial variation of ion current density j at fixed axial positions z with the assumption of an axisymmetric plume.

$$I_b(z) = \int_0^{2\pi} \int_{r_1}^{r_2} j(r,z) r dr d\phi = 2\pi \int_{r_1}^{r_2} j(r,z) r dr \tag{4.3}$$

The radial integration limits r_1 and r_2 significantly impact the magnitude of the integrated beam current. A comparison of three different sets of radial limits is given by Reid [70], and the method used here is Reid's "dynamic integration", which assigns r_1 and r_2 to the locations where the current density falls to $1/e$ of the peak for fixed axial position. Figure 4.11 illustrates these limits on a dual-channel condition for the X2. As noted by Reid, the dynamic integration method makes the radial limits of integration nearly the same as the discharge channel walls for current density profiles close to the exit plane. While the plumes expand, the radial limits expand accordingly. When $j_{\max}/e$ becomes obscured due to plume blending, integration of the current density profiles stops because individual beam currents no longer exist, as discussed further in Section 6.2.

Equation 4.3 yields beam current as a function of axial position, so obtaining a value for I_b requires spatial consistency in $I_b(z)$. Figure 4.12 shows a sample of the inner and outer beam currents at multiple axial positions before the occurrence of significant plume blending. Beam currents for the X2 typically remained consistent from 0 to $0.20 d_{OC}$ of the exit plane, and the final values were the averages of the beam currents within this spatial range.

The divergence half-angle β also depends on the integration limits, as shown in Equation 4.4. This formulation of β also originates from Reid's method developed on the H6. The definition of $\beta(z)$ uses the outside radial limit r_2 to minimize the

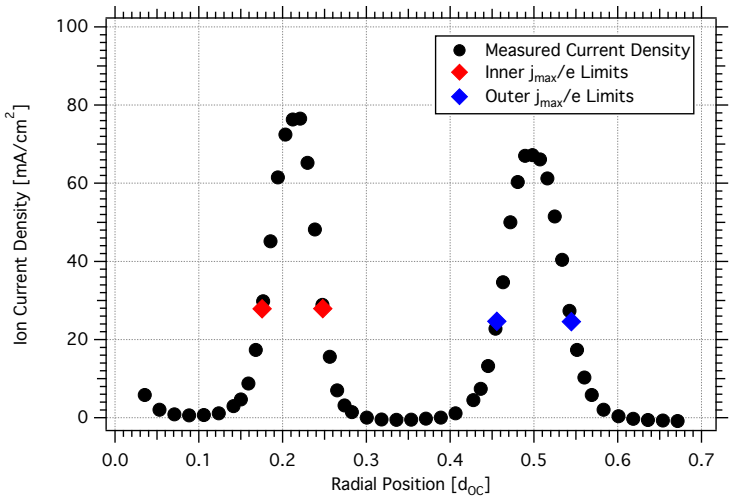

Figure 4.11: **Limits of integration for a dual-channel plume according to Reid's dynamic integration method using data for 200 V, 7.0+17.4 mg/s at 0.04d_{OC}**

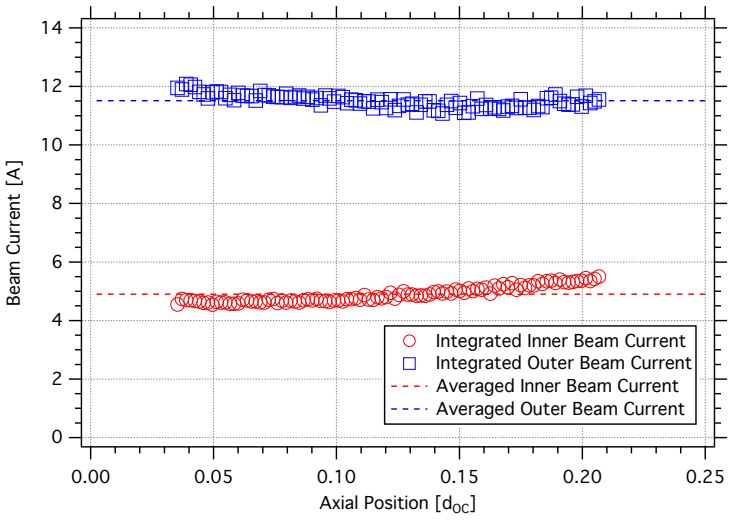

Figure 4.12: **Sample of integrated beam currents as a function of axial position for 200 V, 7.0+17.4 mg/s**

influence of plume merging on the calculation of divergence angle. Of course, the effects of plume merging are unavoidable for the inner channel during dual-channel operation, but Equation 4.4 permits the calculation of $\beta(z)$ for the outer channel at more axial positions.

$$\beta(z) = \text{atan}\left(\frac{r_2 - r_{\text{max}}}{z}\right) \tag{4.4}$$

Due to its definition, the calculated values of $\beta(z)$ are excessively high near the exit plane due to the small values for z, as shown in Figure 4.13. Determination of a final β required the evaluation of $\beta(z)$ at multiple axial positions, and the value to which $\beta(z)$ converges with increasing z was the final β for a given channel and operating conditions. As performed with beam current, the calculation of divergence angle for either channel terminates at the points where the j_{max}/e point becomes obscured by plume merging and expansion.

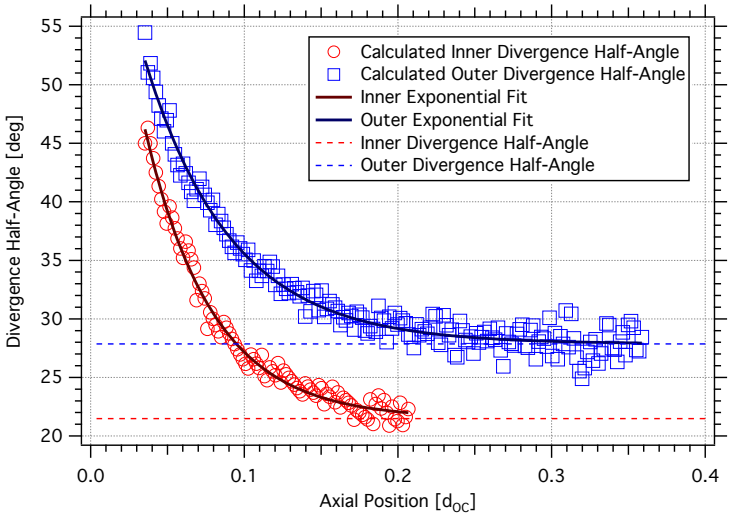

Figure 4.13: **Sample of divergence half-angles as a function of axial position for 200 V, 7.0+17.4 mg/s**

4.3.3 Floating Emissive Probe

Measurements of the plasma potential distribution utilized a floating emissive probe based on prior measurements by Reid [39] and Haas [69]. This technique underestimates the local plasma potential by approximately $1.5T_e$ [71, 72] and therefore requires a corrective measurement of electron temperature. Swept emissive probes can provide higher accuracy, as shown by Sheehan and Hershkowitz [71], but the implementation of swept emissive probes for spatial maps would involve the synchronization of voltage sweeps at multiple filament currents. More importantly, measurements with the floating emissive probe showed decreasing perturbations to the discharge as the floating emissive probe approached the limit of large emission. At small emission currents, the emissive probes would sometimes destabilize the discharge during internal shots, as shown in Figure 4.14(a). The perturbation to the thruster at large emission currents, shown in Figure 4.14(b), proved much less violent.

Each emissive probe featured a half-loop filament made of 0.125-mm diameter, 1% thoriated tungsten wire, as illustrated in Figure 4.15. The filament was crimped to copper EDM electrode tubes that measured approximately 0.399 mm in outer diameter and 0.127 mm in inner diameter. The filament and tube assembly was housed in 1.59-mm dual-bore aluminum oxide tubing that had a layer of protective boron nitride paint. Due to shocks, vibration, and heating, small portions of the boron nitride paint eventually cracked and separated, but enough of the BN coating remained intact to protect the probe. No probe measurements showed any effects from the damaged coating.

The support electronics for the floating emissive probe, as illustrated in Figure 4.16, consisted primarily of a floating filament power supply and a voltage divider. A computer provided the analog input signal to varying the filament current sourced by the Kepco ATE 25-4m. Based on recommendations from Goebel, the filament current remained low between injections (standby) to maximize filament lifetime.

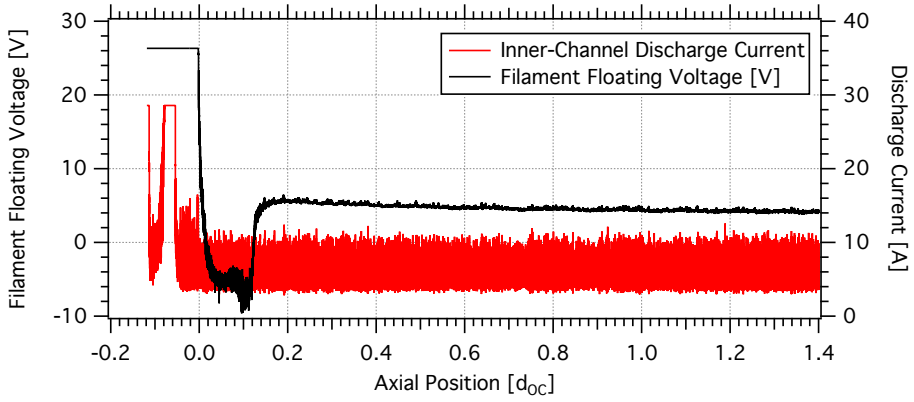

(a) Small Emission Current (2.10 A)

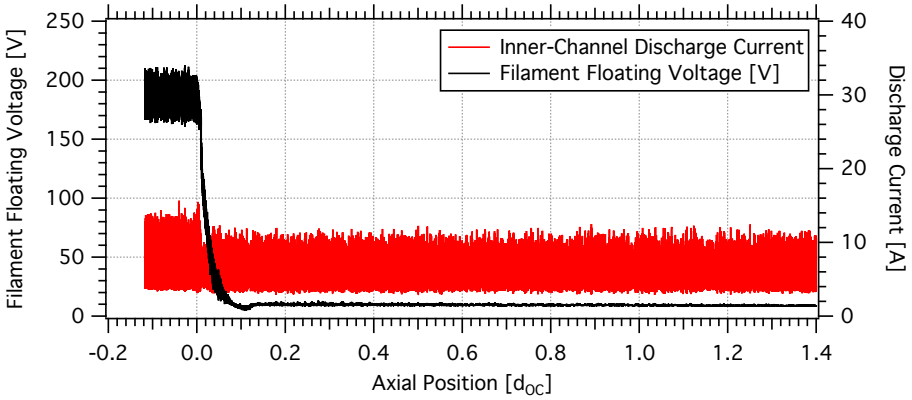

(b) Large Emission Current (3.30 A)

Figure 4.14: **Thruster response to the injection of an emissive probe at small and large emission currents along the centerline of the inner channel**

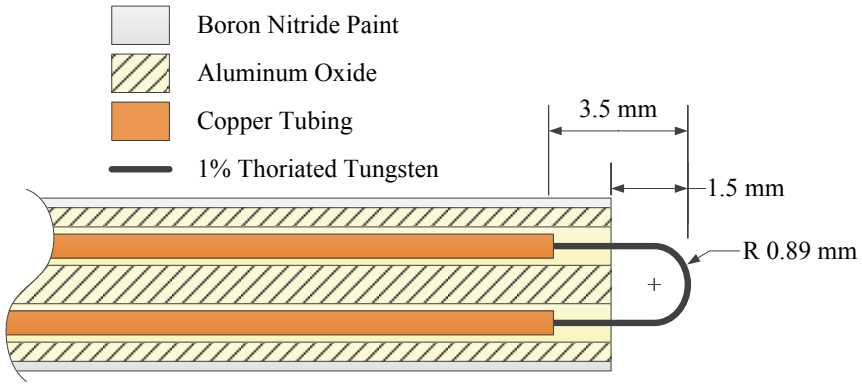

Figure 4.15: **Floating emissive probe construction (not to scale)**

Prior to an injection by the HARP, the computer commanded the filament current to ramp up to provide sufficient power to achieve large emission. The voltage divider provided a measure of the potential at the center of the filament by providing the average potential between the input and output sides of the floating power supply. An API 610-10-2 voltage probe measured potential difference between the center of the voltage divider and facility ground. An Agilent DSO-X 3024A oscilloscope recorded the filament floating voltage along with the cathode-to-ground voltage and both discharge currents.

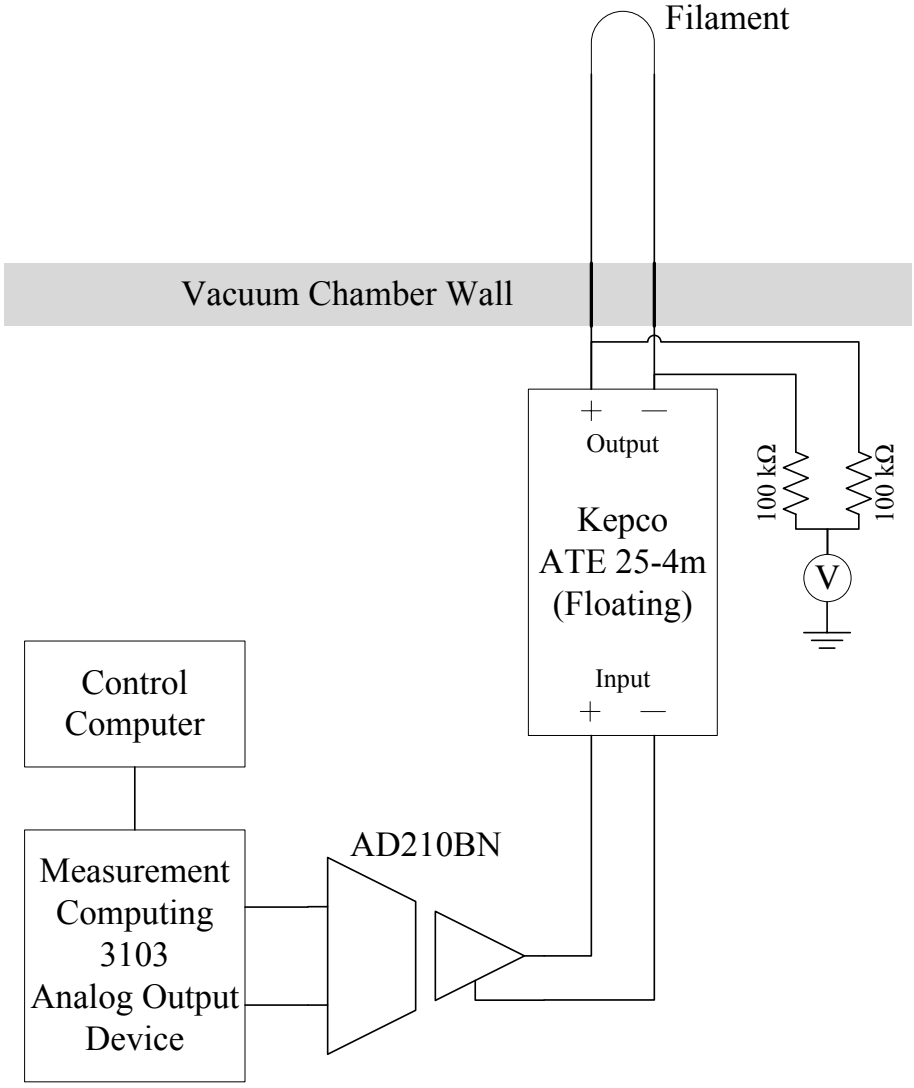

Figure 4.16: **Electrical schematic for the floating emissive probe**

4.3.4 Asymmetric Floating Double Langmuir Probe

The implementation of the floating double probe was similar to previous work by Haas [69] and Herman [73] with the exception of the asymmetric geometry. Based on the observations from the emissive probe measurements (Figure 4.14(a)), a floating probe provided the lowest level of thruster perturbations, so a floating double probe became a suitable choice for measuring electron temperature. However, this technique only samples electrons with the highest velocities (on the "tail" of the distribution) [74]. The use of asymmetric collectors permits the measurement of more bulk electrons, with infinite asymmetry essentially providing the results of a single Langmuir probe.

The design of the double Langmuir probe leveraged some of the design features of the floating emissive probe. Illustrated in Figure 4.17, the double probe utilized 0.24-mm and 0.53-mm diameter tungsten wires in 1.59-mm aluminum oxide tubes. The ratio of collection areas between the large and small collectors was 2.2:1. A protective layer of boron nitride paint covered the external surfaces of both aluminum oxide tubes. During measurements, the small collector was above the vertical midplane of the thruster while the large collector was below such that the midplane bifurcated the two electrodes.

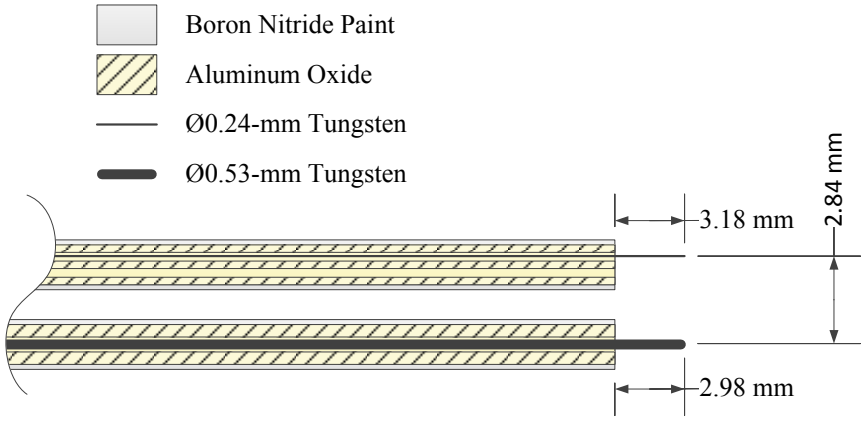

Figure 4.17: **Floating double Langmuir probe construction (not to scale)**

The double probe electronics, as shown schematically in Figure 4.18, held the double probe at constant bias voltage during a single axial shot of the HARP. Sweeping the probes during shots became impractical due to line capacitance and the resulting capacitive current. Instead, a floating 67.5-V battery powered a TPS7A4001 variable DC voltage regulator that biased the two probes. An external potentiometer provided adjustment of the DC output voltage, while a double pole, double throw switch controlled the bias polarity. Isolation amplifiers provided real-time signals for both the small probe current and bias voltage to an Agilent DSO-X 3024A.

Analysis of double probe measurements first required assembly of I-V traces from each axial shot of the HARP and then utilized methods developed by Johnson and Malter [75, 76] and described by Chen [74]. Assuming no changes in the plasma potential or random current densities between the electrodes, the electron temperature T_e from a double Langmuir probe is given by (using Chen's notation):

$$\frac{k_B T_e}{e} = \left(\left. \frac{dI}{dV} \right|_{V=0} \right)^{-1} \frac{I_{1+} I_{2+}}{I_{1+} + I_{2+}} \tag{4.5}$$

where I_{1+} and I_{2+} are the ion currents to probes 1 and 2, respectively, after extrapolation of both ion saturation curves to V=0. $\left. \frac{dI}{dV} \right|_{V=0}$ is the slope of the I-V characteristic at $V = 0$. Figure 4.19 illustrates this process on a sample data set.

4.4 Vacuum Facility

Experiments on the X2 were performed in the Large Vacuum Test Facility (LVTF) in PEPL. LVTF is a cylindrical vacuum chamber that measures 6 meters in diameter and 9 meters in length. Seven CVI model TM-1200 cryopumps with liquid nitrogen shrouds are used to achieve a base pressure on the order of 1×10^{-7} torr. The nominal pumping speed for xenon is 245,000 l/s with all seven cryopumps operating.

Pressure was measured using a Varian UHV-24 nude ionization gauge and a Varian

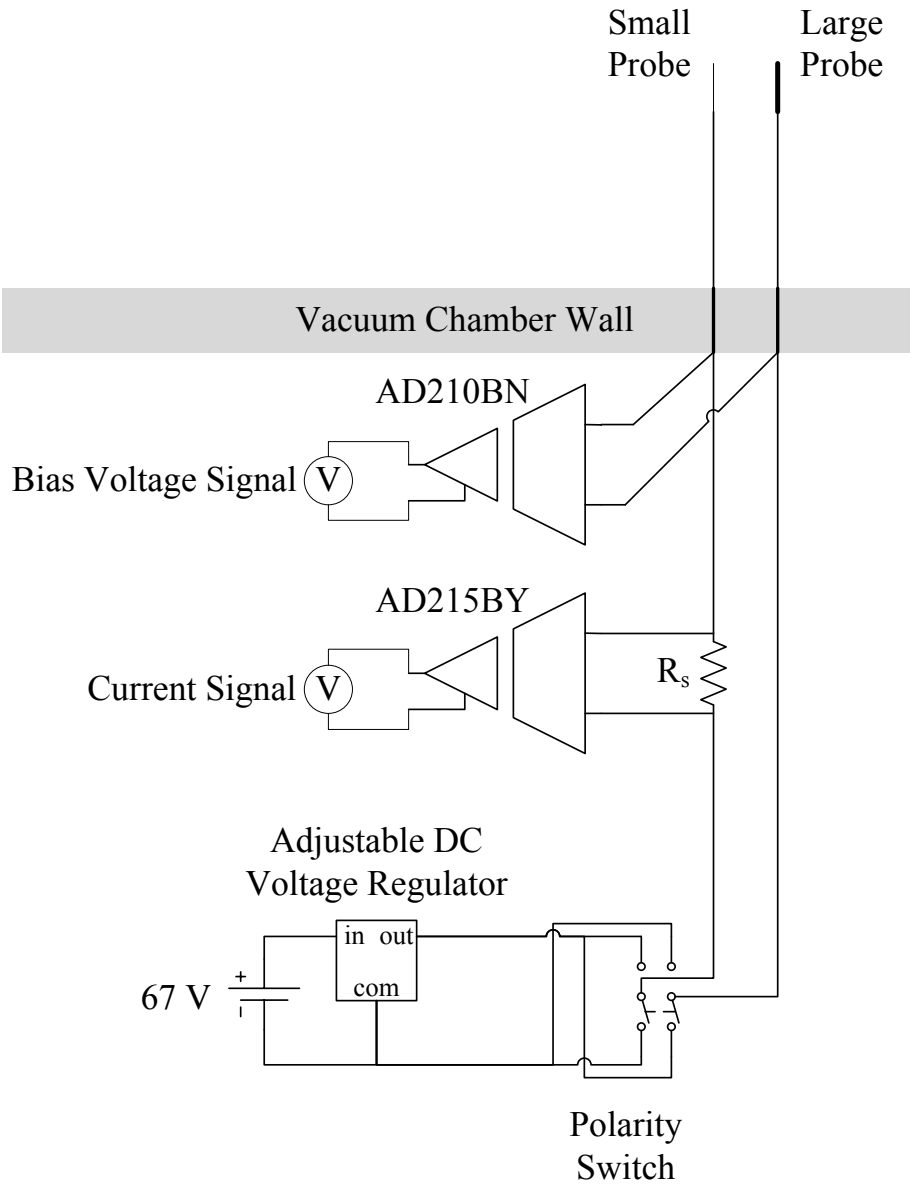

Figure 4.18: **Electrical schematic for the floating double Langmuir probe**

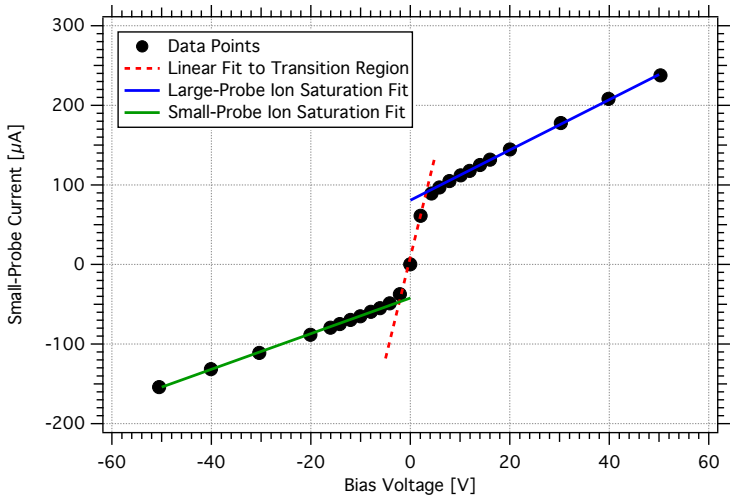

Figure 4.19: **Sample analysis of double probe data from 200 V, 7.0+17.4 mg/s**

model 571 Bayard-Alpert ionization gauge connected to a Varian XGS-600 gauge controller. Both ionization gauges mated to flanges on the wall and near the top of the vacuum chamber. The reported background pressures are an average of the pressure measurements taken by the two gauges. Typical accuracy for ionization gauges is approximately ±20% according to Agilent [77].

$$p_c = \frac{p - p_b}{2.87} + p_b \tag{4.6}$$

As measurements from the ionization gauges were calibrated for air, corrections were made for xenon according to Equation 4.6 [78]. The corrected background pressure p_c is determined using the indicated pressure p, the base pressure p_b, and a correction factor of 2.87. During experimentation, the base pressure p_b was updated every morning following an overnight period of inactivity.

4.5 Summary

This chapter described the instruments and diagnostics used in the study of the X2 NHT. An inverted-pendulum thrust stand measured the thrust produced by the

X2 in a closed-loop controlled null mode. A retarding potential analyzer and E×B probe were placed in the far field to determine the most-probable ion voltage and ion charge states. Measurements were performed with a near-field Faraday probe to determine beam current and divergence angle. All of these measurements will be used to study how efficiently the X2 is operating as a propulsion device.

Measurements with a floating emissive probe and a double probe were also utilized to study how the acceleration of ions changes with a NHT. The floating emissive probe was used to spatially map the plasma potential internally and in the near field. Electron temperature measurements from the double probe were used to correct the emissive probe measurements. These probes, along with the near-field Faraday probe, were actuated by the HARP to minimize perturbations to the thruster.

CHAPTER V

Performance of a Nested Hall-Effect Thruster

As discussed in Chapter II, the nested Hall-effect thruster is a relatively unexplored propulsion concept. This lack of study led to the development of the X2 NHT and the utilization of diagnostics described in Chapters III and IV.

This chapter shows the results of measurements performed on the X2 in order to describe the capabilities of this thruster as a propulsion device. Section 5.1 discusses the performance measurements of the X2 in its three operating modes at the constant mass flow rate. These measurements served to both shake down the thruster and to determine the general capabilities of all three modes of operation. Section 5.2 discusses performance measurements of the X2 at constant discharge power. This will demonstrate the ability for NHTs to throttle from high thrust-to-power to high specific impulse while fully utilizing a fixed amount of available power.

Performance measurements on the X2 NHT utilized the inverted-pendulum thrust stand along with measurements of power and propellant mass flow rate. These measurements can be separated into three sets:

- Single-channel operation at constant mass flow rate
- Dual-channel operation at constant mass flow rate
- Single-channel and dual-channel operation at constant discharge power

The first set of performance measurements were a natural starting point for the X2 following initial assembly. These measurements verified that each channel operated as a functional HET. While throttling discharge voltage, the mass flow rate through one of the anodes and the cathode were held constant. Discharge voltage was varied from 150 V up to 550 V, and the magnets were tuned at each discharge voltage setting. The second set of measurements occurred in a similar manner but with both channels firing simultaneously.

Constant power measurements were performed at 5 kW and 6 kW between 125 V and 600 V. This third set of measurements chained together dual-channel conditions with single-channel conditions to span a wide I_{sp} range at constant power. At each condition, the discharge voltage, mass flow rates, and magnet currents were all adjusted for optimal anode efficiency.

5.1 Performance Measurements at Constant Mass Flow Rate

A typical day of performance measurements began with a warm-up period of at least one hour. If the thruster had been exposed to atmosphere prior to startup, the warm-up period would also bake out any water that absorbed into the ceramic walls. Toward the end of the tests involved with this work, the magnets were energized during pumpdown to heat up the thruster and bake out the water before thruster startup. The X2 was then fired after approximately 8 hours of heating under the magnets with no significant temporary increase in discharge current magnitude or oscillation amplitude.

5.1.1 Single-Channel Performance Measurements at Constant Mass Flow Rate

The nominal mass flow rates for the inner channel and outer channel were 9.3 mg/s and 23.2 mg/s, respectively. Flow rates tested were 50%, 75%, 100%, and 125% of the

nominal values, as shown in Table 5.1. Cathode flow fractions (CFF) during single-channel operating conditions were originally held at 7%. However, after the first dual-channel operating conditions appeared to favor higher CFF, most subsequent conditions, including single-channel conditions, were performed at 10% CFF.

Table 5.1: **Flow rates for single-channel conditions**

Inner Anode Mass Flow Rate [mg/s]	Outer Anode Mass Flow Rate [mg/s]	Percent Nominal Flow Rate
4.7	-	50%
7.0	-	75%
9.3	-	100%
11.7	-	125%
-	11.6	50%
-	17.4	75%
-	23.2	100%
-	29.0	125%

Figures 5.1(a) and 5.1(b) show the thrust produced in single-channel mode as a function of discharge voltage. The typical uncertainty for thrust is ±3 mN. As mass flow rate was fixed, discharge voltage was the independent variable for these measurements. With increasing discharge voltage, beam ions reached increasingly higher exit velocities. This naturally resulted in thrust increasing with discharge voltage at constant mass flow rate. The inner channel produced from 31 mN up to 303 mN, while the outer channel produced 71 mN up to 547 mN. At all mass flow rates, the thrust increased monotonically with discharge voltage. This serves as one of several signs that each channel of the X2 functioned as its own thruster

Specific impulse measurements, shown in Figures 5.2(a) and 5.2(b), provide insight into how effectively each channel used propellant to produce thrust. The inner channel demonstrated $I_{sp,a}$ of 682 s to 2696 s, while the outer channel $I_{sp,a}$ varied from 682 s to 2326 s. As typical for a HET, the $I_{sp,a}$ increases with increasing discharge voltage. For both channels, the 50% nominal flow rates have generally lower $I_{sp,a}$ than the

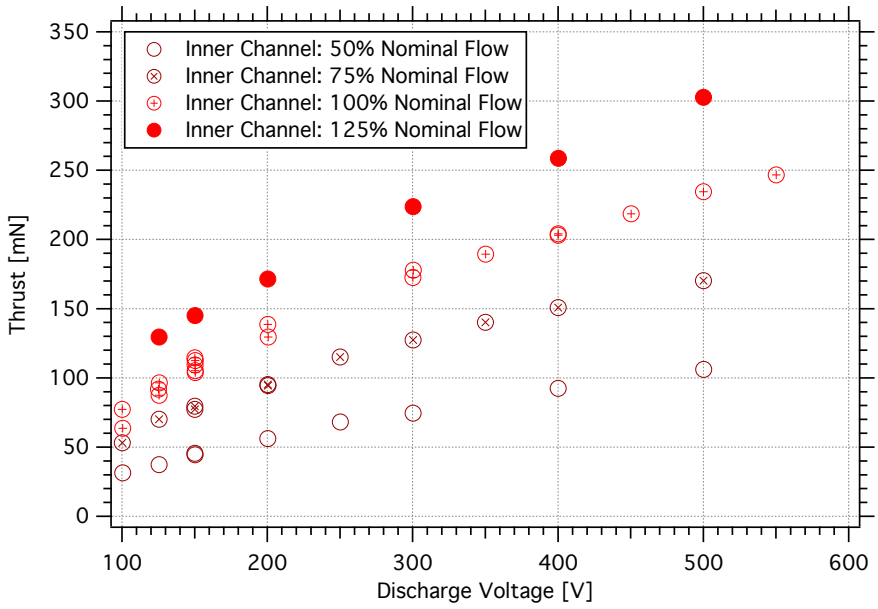

(a)

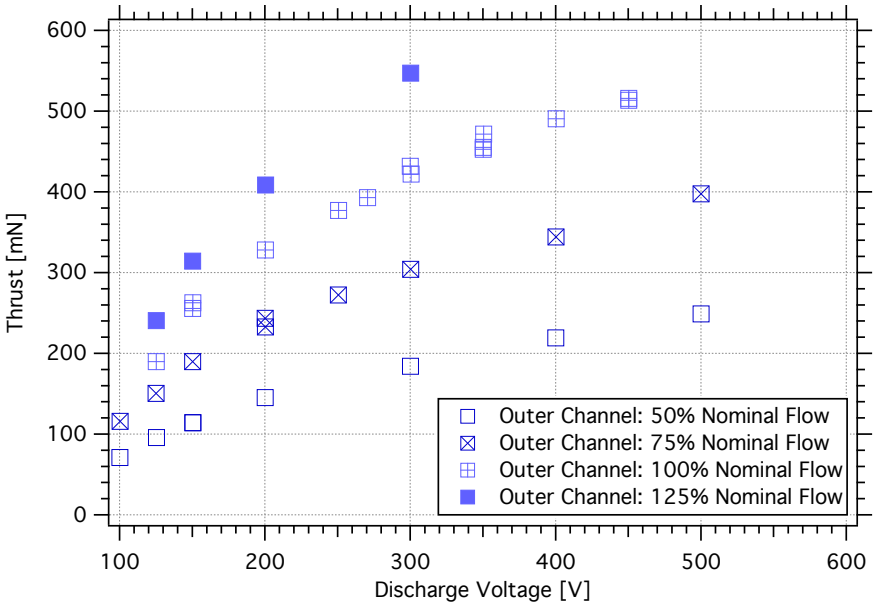

(b)

Figure 5.1: **Thrust produced in single-channel modes at constant mass flow rate.** Thrust uncertainty is typically ±3 mN and is smaller than the marker size.

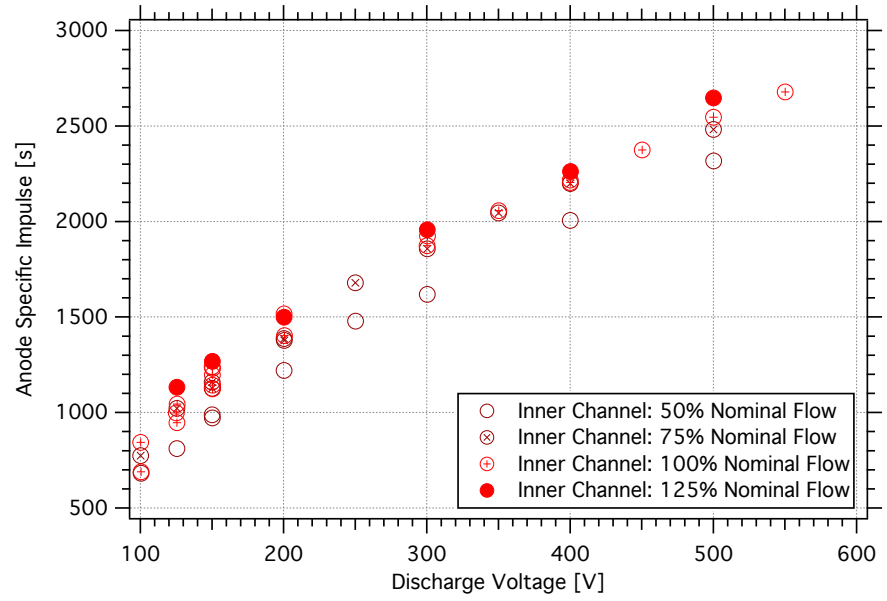

(a)

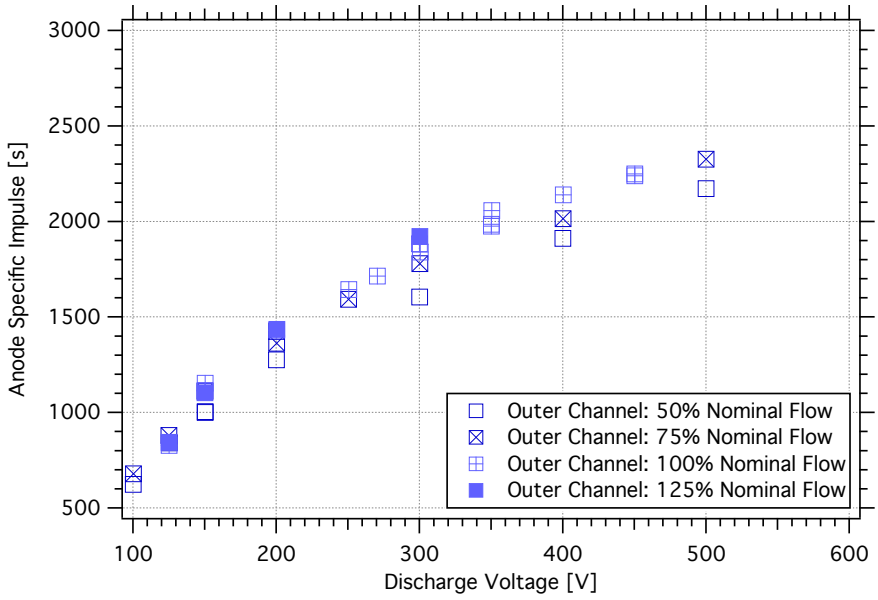

(b)

Figure 5.2: **Anode specific impulse from single-channel modes at constant mass flow rate.** The uncertainty for the inner-channel conditions at 50% and 75% nominal mass flow rate was ±200 s. Otherwise, the uncertainty is ±100 s.

other mass flow rates.

A comparison of the two data sets also reveals that the outer channel does not produce as high $I_{sp,a}$ as the inner channel at higher discharge voltages. This is one indication that the outer channel does not operate as effectively at high discharge voltages in comparison to the inner channel. This will become even more apparent in the anode efficiency data.

To avoid obscuring the data, the uncertainty in $I_{sp,a}$ was not shown in Figures 5.2(a) and 5.2(b). For the two conditions with the lowest flow rates (50% and 75% nominal on the inner channel), the relative uncertainty in mass flow rate becomes sufficiently high for the uncertainty in $I_{sp,a}$ to be approximately $\pm$200 s. Otherwise, the uncertainty is typically below $\pm$100 s.

Figure 5.3(a) and 5.3(b) show the anode efficiencies measured for the single-channel conditions at constant mass flow rate. Both channels exhibit increasing η_a as discharge voltage increases from 100 V to 300 V. Above 300 V, anode efficiency for the inner channel begins to plateau, reaching a maximum of 68%. However, anode efficiency for the outer channel begins to drop above 300 V, except at 50% of the nominal flow rate. The maximum anode efficiency obtained by the outer channel is 63%, and the maximum occurs from 300 V to 350 V.

The uncertainty in η_a was also omitted from Figures 5.3(a) and 5.3(b) for clarity. Typically, the uncertainty is below $\pm$3% absolute. For the conditions with the lowest flow rates (50% and 75% nominal on the inner channel), the uncertainty is as high as $\pm$6% absolute.

To this point, each channel of the X2 demonstrated functionality as single-channel HETs. Reasonably high anode efficiencies were obtained by both channels, and most trends as a function of discharge voltage were fairly typical. For X2, the characterization of each channel is important, as they are the fundamental building blocks for the dual-channel conditions. The only concern from the single-channel performance

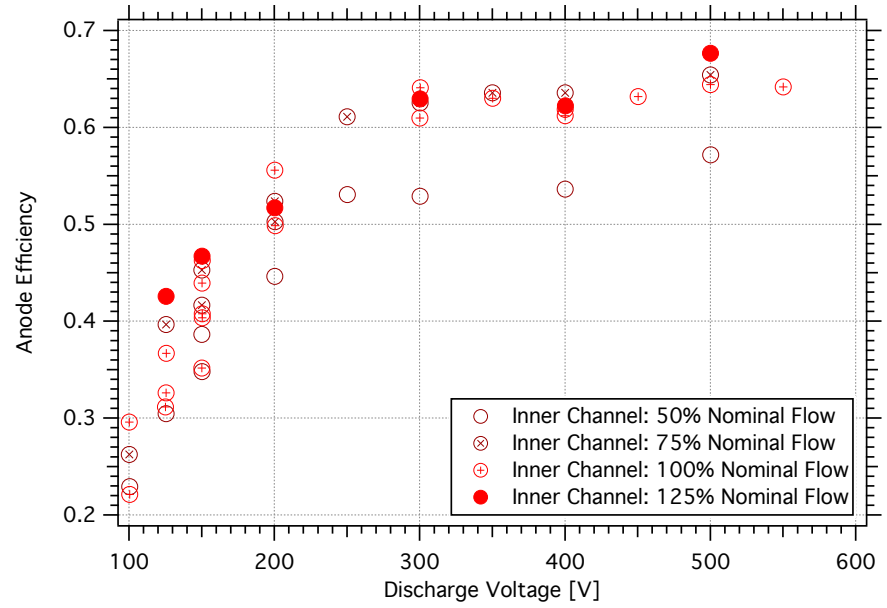

(a)

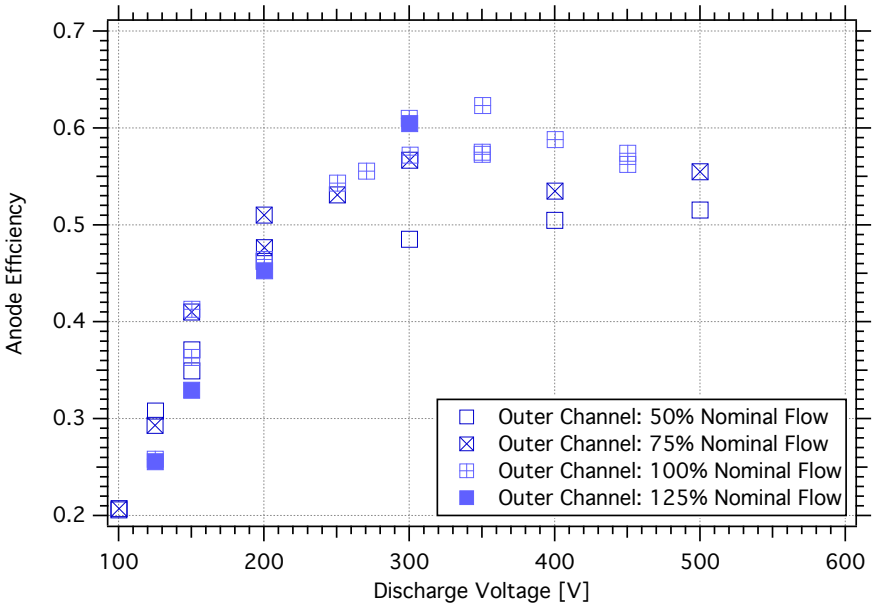

(b)

Figure 5.3: **Anode efficiencies from single-channel modes at constant mass flow rate.** The uncertainty for the inner-channel conditions at 50% and 75% nominal mass flow rate was ±6% absolute. Otherwise, the uncertainty is ±3% absolute.

data was the reduced efficiency of the outer channel above 300 V, and this will have an impact on the performance of the X2 in dual-channel mode.

5.1.2 Dual-Channel Performance at Constant Mass Flow Rate

Dual-channel conditions occurred with mass flow rates at the same fractions with respect to their nominal values, as shown in Table 5.2. To avoid confusion, the combined mass flow rate in dual-channel conditions is denoted as $\dot{m}_1 + \dot{m}_2$. This communicates the mass flow rates through each anode and allows calculation of the total mass flow rate and the flow split ratio (1:2.5). Tuning of the magnets was performed as described previously in Section 3.3.

Table 5.2: **Flow rates for dual-channel conditions**

Combined Mass Flow Rate [mg/s]	Percent Nominal Flow Rate
4.7+11.6	50%
7.0+17.4	75%
9.3+23.2	100%
11.7+29.0	125%

The constraints on throttling in dual-channel mode are worth noting at this point. Due to the number of adjustable parameters with the X2, a dual-channel throttling table can quickly grow into a multidimensional problem. The discharge voltage to each channel, mass flow rate to each anode, and the cathode flow rate are all independently adjustable. For a NHT, this leads to the possibility of operation with mixed discharge voltages and/or mixed current densities. These modes were quickly explored but are mostly out of the scope of this work.

To simplify throttling the X2, a number of constraints were introduced to the inputs to the thruster. As shown in Table 5.3, the discharge voltages applied to each channel were equal. The mass flow rates to each anode were set to a fixed ratio, and the cathode flow rate was a fixed percentage of the combined anode mass flow rate.

Table 5.3: **Throttling constraints for dual-channel conditions**

Discharge Voltages	Equal
Mass Flow Rates	1:2.5 (Inner:Outer)
Cathode Flow Fraction	10% of Combined Anode $\dot{m}$
Magnet Currents	Tuned at Every Condition

During the time of these measurements, the X2 exhibited visible oscillations at 300 V. Several adjustments were made toward the end of this work that made high-voltage operation more stable. These include spray coating the middle pole with boron nitride and fixing the cathode flow rate to a value that is better for its life and operation [59]. However, those efforts could not be a part of this initial study of NHTs.

Under these constraints, thrust measurements were made on dual-channel conditions and are shown in Figure 5.4. In dual-channel mode, the X2 produced 112 mN to 720 mN. From 100 V to 250 V, thrust generally increases with increasing discharge current at constant flow rate. Above 200V, thrust begins to plateau or drop, indicating a significant loss in efficiency at those voltages. As the outer channel is the dominant of the two channels in terms of size and flow rate, this drop in efficiency at 300 V is attributed to its lower efficiencies at higher voltages as a stand-alone thruster. However, for low-voltage, high thrust-to-power operation, the dual-channel mode appears to operate well.

Figures 5.5 and 5.6 show the anode specific impulse and anode efficiencies for the dual-channel mode at constant flow rate. Both $I_{sp,a}$ and η_a vary with discharge voltage as expected from 100 V to 200 - 250 V. Anode specific impulse up to 1850 s and anode efficiencies up to 71% were achieved. Once again, good performance is observed up to 250 V for most flow rate combinations, while performance decreases above that threshold voltage.

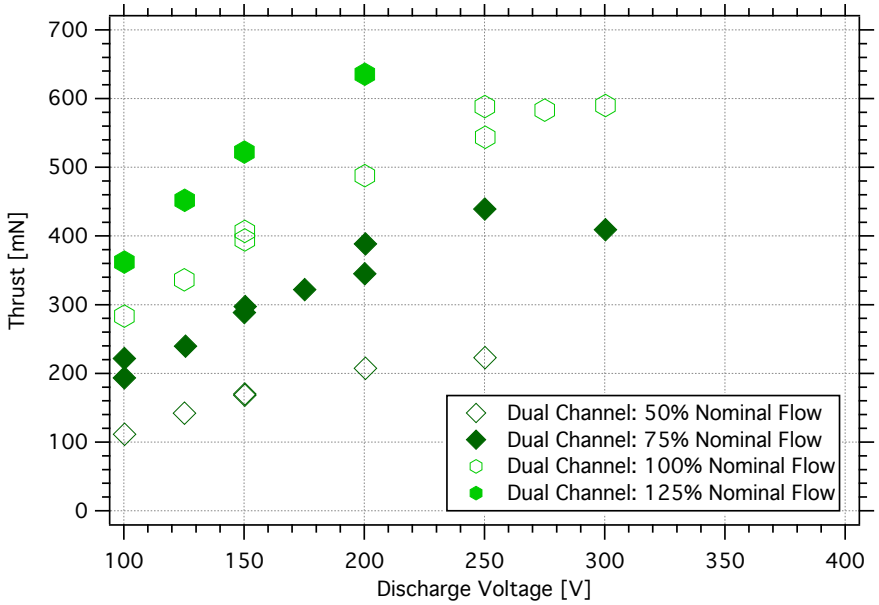

Figure 5.4: **Thrust produced in dual-channel mode at constant mass flow rate.** Thrust uncertainty is typically ±3 mN and is smaller than the marker size.

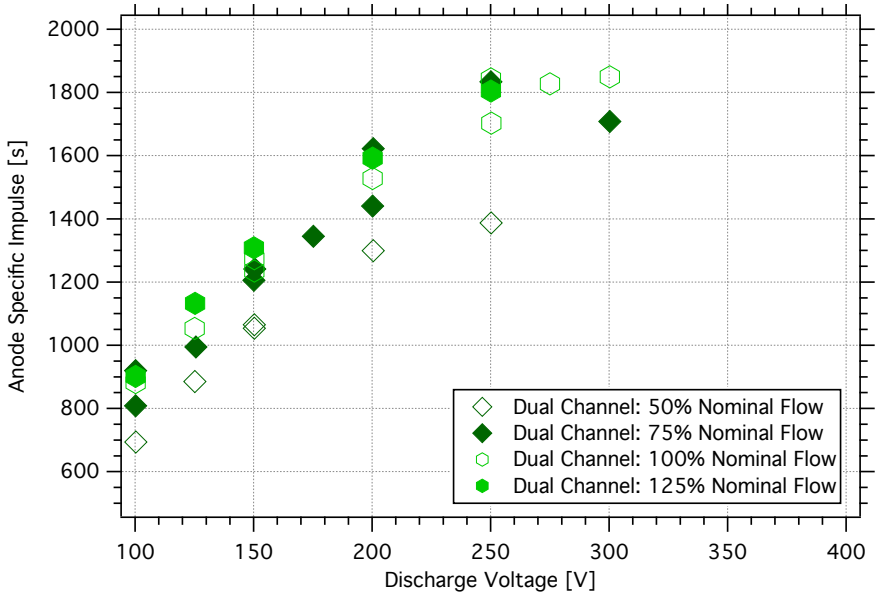

Figure 5.5: **Anode specific impulse in dual-channel mode at constant mass flow rate.** The associated uncertainty was ±50 s.

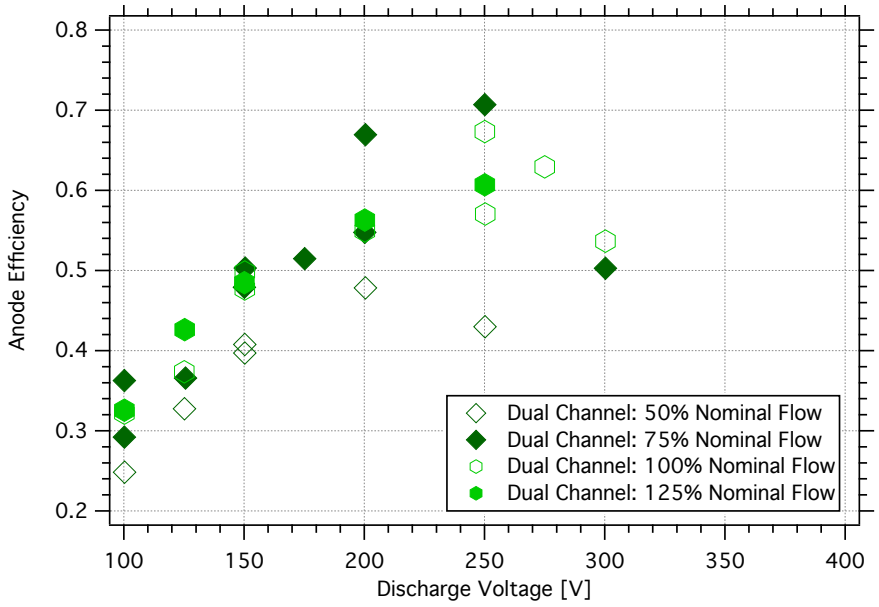

Figure 5.6: **Anode efficiency in dual-channel mode at constant mass flow rate.** The uncertainty in anode efficiency for these data points were ±2% absolute.

5.1.3 Comparison of Single-Channel and Dual-Channel Performance

For a direct comparison of dual-channel performance to single-channel performance, thrust-to-power ratio, anode specific impulse, and anode efficiency for all three modes are shown in Figures 5.7, 5.8, and 5.9, respectively. To reduce clutter, only the 75% and 100% nominal flow combinations are shown, as those conditions provide the best thrust-to-power ratio and anode specific impulse.

As discussed in Section 3.2, the dual-channel mode of the X2 was designed for low-voltage, high thrust-to-power operation, and as shown in Figure 5.7, this mode excels above the single-channel modes in this operating regime. After approximately 55 hours of cumulative operation, the X2 demonstrated 84 mN/kW at 200 V, 75% nominal flow rate in dual-channel mode. The points at 100 V, 150 V, and 200 V were revisited after an additional 55 hours on the inner channel and 40 hours on the outer channel. In all cases, T/P_d decreased as the channel geometries changed due to erosion. The decrease in performance over the first 110 hours is illustrated

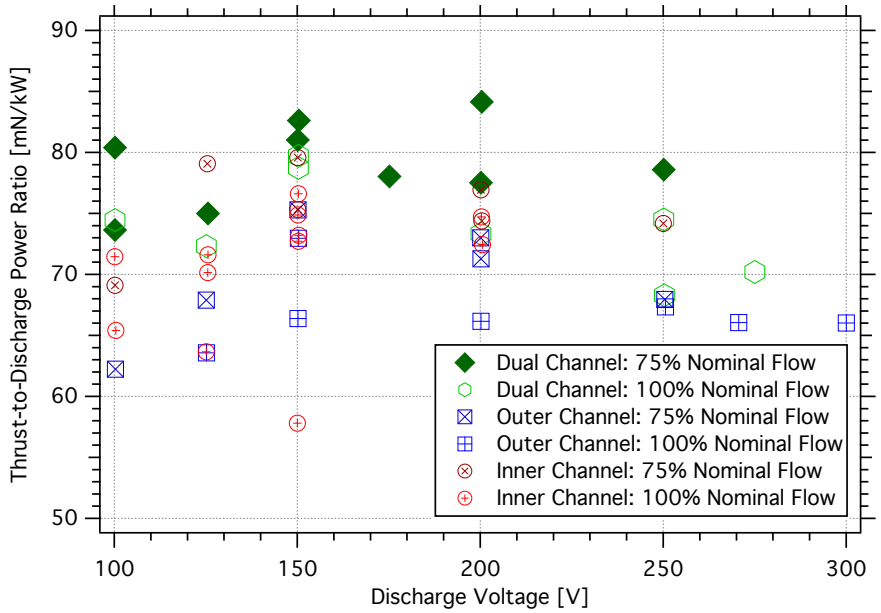

Figure 5.7: **Comparison of thrust-to-power ratios between dual-channel and single-channel modes.** The uncertainty in thrust-to-power ratio is no greater than 2 mN/kW.

in the two sets of dual-channel operating points at 75% nominal mass flow rate in all performance plots at constant mass flow rate. After 110 hours, the magnets were retuned to maximize efficiency, resulting in T/P_d to maximize at 150 V and 81 mN/kW. The uncertainty in T/P_d was no greater than ± 2 mN/kW.

Figure 5.8 shows single-channel and dual-channel $I_{sp,a}$ in the same discharge voltage range. Given uncertainties up to ± 100 s, all three operating modes produced comparable anode specific impulse from 100 V and 200 V. The conditions at 250 V show marginal improvement in I_{sp} in dual-channel mode.

Anode efficiencies are also relatively comparable between operating modes, with the exception of a few conditions at 75% nominal flow. Shown in Figure 5.9, the dual-channel mode produced anode efficiencies comparable or better than the single-channel modes. The uncertainties were again up to $\pm 6\%$, absolute.

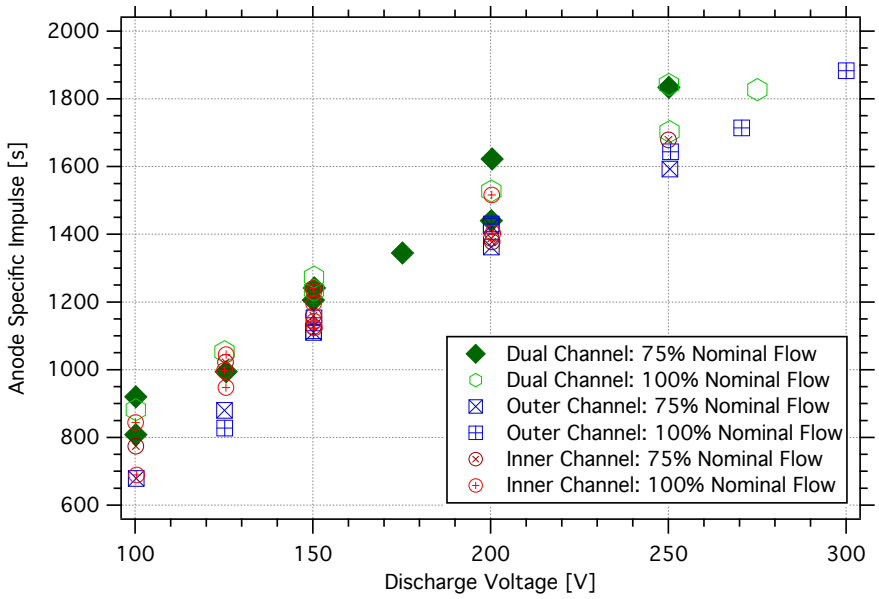

Figure 5.8: **Comparison of anode specific impulse between dual-channel and single-channel modes.** The uncertainty in anode specific impulse is up to ±100 s.

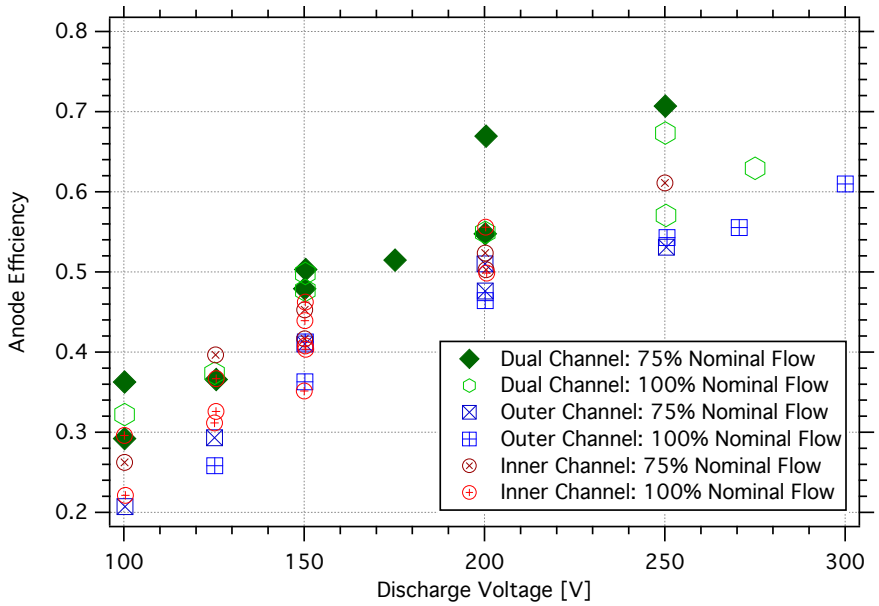

Figure 5.9: **Comparison of anode efficiencies between dual-channel and single-channel modes.** Uncertainty in anode efficiency does not exceed ±6% absolute.

5.1.4 Facility Effects on Comparison of Single-Channel and Dual-Channel Performance

The ingestion of neutrals inside a vacuum chamber can alter the thrust from a HET, as the thruster can ionize and accelerate particles that would otherwise not be present in space [50, 79–82]. Dual-channel conditions naturally operate at higher background pressures where the background neutral density would be higher than that of a single-channel condition. As a result, the increased performance in the dual-channel mode may be a result of increased ingestion of background neutrals.

Investigation of this effect involved simply running single-channel conditions at the same background pressure as a dual-channel condition. This method does not correct the thrust for neutral ingestion but, instead, maintains the facility effect to the same degree between operating modes. Three dual-channel conditions were chosen at 150 V at three different flow rates: 50%, 75%, and 100% of nominal. The background pressures, measured by an average of a nude ion gauge and an external ion gauge on the chamber wall, were $1.1{\cdot}10^{-5}$, $1.6{\cdot}10^{-5}$, and $2.1{\cdot}10^{-5}$ torr-Xe, respectively and were held within $\pm 0.1{\cdot}10^{-5}$ between operating modes. Each dual-channel condition preceded two single-channel conditions with the same magnet settings and cathode flow fraction. Increased background pressure in the single-channel conditions came from diverted propellant flow that would have gone to the inactive channel. A rudimentary injector and diffuser introduced xenon approximately 2.5 m downstream of the thruster.

The thrust measurements show that the increased performance observed in dual-channel mode is more than just a background pressure effect. Figure 5.10 shows the results of these thrust measurements. p_c was constant for each set of inner-channel, outer-channel, and dual-channel conditions, not for all nine conditions. At each flow rate combination, the superposition of the single-channel thrusts repeatedly falls short of the measured dual-channel thrust. The percent increase from the superposition to

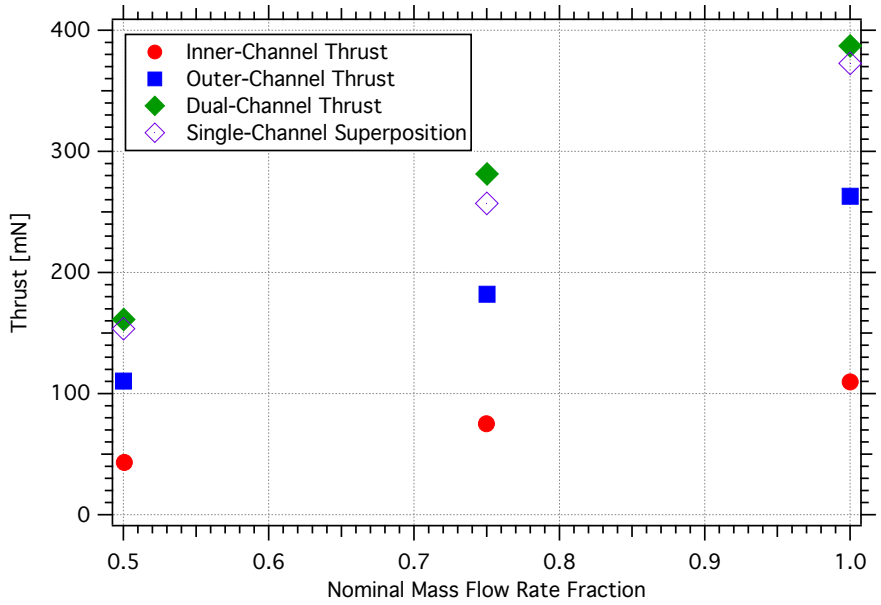

Figure 5.10: **Thrust decomposition for three dual-channel conditions at constant background pressure.** Measurements of thrust in this figure are accurate to ±1 mN and is not visible due to the marker size. Comparison between the superimposed single-channel data and the dual-channel data shows that dual-channel firings introduce 4% to 9% increase in thrust.

dual-channel thrust varied from 4% to 9%. Observing improved dual-channel performance at constant background pressure indicates that the ingestion of background neutrals alone is insufficient to account for the increases in dual-channel performance.

At constant pressure, the discharge currents are nearly constant between operating modes with a maximum observed variation of 3.4%. Shown in Figure 5.11, the outer-channel discharge currents are higher in single-channel mode, while the inner channel exhibits the opposite behavior in all but the nominal mass flow rate condition. The increase in outer discharge current from dual-channel to single-channel mode is between 0.15 A and 0.33 A (0.9% and 1.4%) and is only slightly greater than the measurement uncertainty of ±0.1 A. For the inner channel, discharge current rises between 0.14 A and 0.08A (3.4% and 1.2%) at 50% and 75% nominal $\dot{m}$ and falls 0.04 A (-0.4%) at nominal $\dot{m}$. Relative to the measurement uncertainty, the changes in discharge current between operating modes are negligibly small.

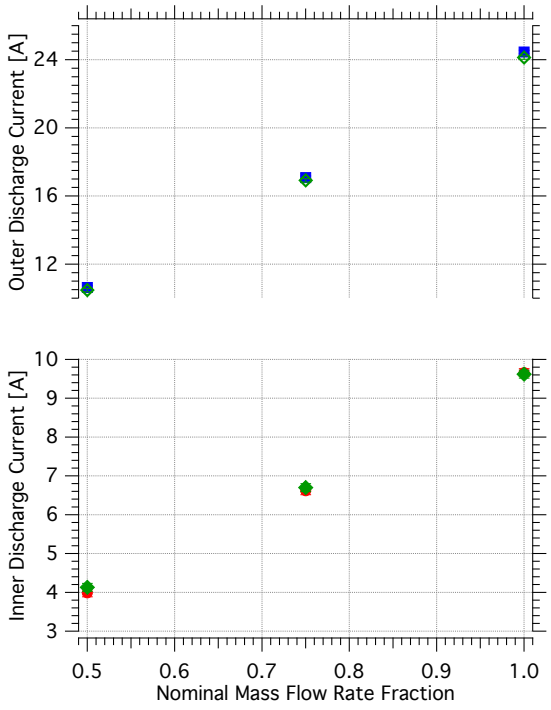

Figure 5.11: **Discharge currents at constant background pressure.** Measurement of discharge current is typically accurate to ±0.1A.

5.1.5 Summary of Performance Measurements at Constant Flow Rate

The measurements at constant flow rate served two purposes. Naturally, the first purpose was to verify the proper operation of both discharge channels while firing individually and while firing simultaneously. The second purpose was to explore how the dual-channel mode compared to the two single-channel modes. When comparing thrust-to-power ratios in particular, the dual-channel mode appears to provide small improvements in performance, even after consideration for neutral ingestion effects. This is the first indicator that operating two nested discharge channel can provide a performance benefit, and the increase has been observed at a low-voltage, high thrust-to-power condition.

These performance measurements also demonstrated that the performance of multi-channel modes of a NHT relies on the performance of each discharge channel as an individual thruster. As seen in the performance data at and above 300 V, a

poorly performing outer channel affects the operation of the thruster in dual-channel mode. This is naturally expected, as the outer channel dominates in both size and mass flow rate. However, the performance decrease due to the outer channel is specific to the X2, and future NHTs can avoid such problems by careful design of each discharge channel.

5.2 Performance Measurements at Constant Discharge Power

As discussed at the beginning of Section 5.1, performance measurements were taken in three sets. This third set features combinations of all three modes of the X2 in order to operate at constant power from 150 V to 600 V. As seen in the performance measurements at constant flow rate, thrust-to-power ratio maximizes around 150 V. Spanning this voltage range therefore allows the X2 to throttle from high thrust-to-power to higher specific impulse at constant power.

The reader should note that constant power is actually constant discharge power in this set of data. Using P_d neglects the magnet power, which is much smaller than the discharge power but can be significant in some cases. The discharge powers shown in this section are 5 kW and 6 kW.

The settings used for the 5-kW and 6-kW operating conditions are shown in Tables 5.4 and 5.5. For all dual-channel conditions, the discharge voltages were the same across both channels, and the division of propellant mass flow rates was held at a ratio of 1:2.4-2.5 between the inner channel and outer channel. Cathode flow fraction was held at 10% of the combined anode mass flow rate during the 6-kW operating conditions. This percentage has been used since the first dual-channel firings of the X2 and has consistently provided stable cathode operation. To investigate if the X2 would operate with less cathode flow, a decreased cathode flow fraction of 7% was used for the 5-kW operating conditions.

Controlling discharge power was performed by iterative adjustment of the mag-

netic field and mass flow rates at a fixed discharge voltage. Tuning of the magnets occurred at every operating condition as described in Section 3.3. Anode mass flow rates were also adjusted with the magnets to achieve the required discharge currents to maintain constant power. The cathode mass flow rate was always adjusted after the magnetic field and the anode flow rates in order to ensure continuously stable cathode operation. The cathode heater and keeper both remained shut off after ignition of the thruster and were not operated during this process.

Table 5.4: **5-kW operating conditions**

Discharge Voltage [V]	Inner Anode Mass Flow Rate [mg/s]	Outer Anode Mass FlowRate [mg/s]	Background Pressure [torr-Xe]
150	9.3	23.0	$2.0 \cdot 10^{-5}$
200	7.5	18.5	$1.6 \cdot 10^{-5}$
350	6.3	15.8	$1.4 \cdot 10^{-5}$
300	5.6	12.9	$1.2 \cdot 10^{-5}$
350	4.5	11.0	$1.0 \cdot 10^{-5}$
400	3.9	9.5	$9.0 \cdot 10^{-6}$
200	-	24.8	$1.7 \cdot 10^{-5}$
250	-	21.4	$1.4 \cdot 10^{-5}$
300	-	18.5	$1.2 \cdot 10^{-5}$
350	-	16.2	$1.1 \cdot 10^{-5}$
400	-	14.4	$9.5 \cdot 10^{-6}$
250	17.6	-	$1.1 \cdot 10^{-5}$
300	16.1	-	$1.1 \cdot 10^{-5}$
400	12.5	-	$8.4 \cdot 10^{-6}$
450	11.4	-	$7.7 \cdot 10^{-6}$
500	10.4	-	$7.1 \cdot 10^{-6}$
550	9.4	-	$6.5 \cdot 10^{-6}$
600	8.7	-	$6.2 \cdot 10^{-6}$

5.2.1 Constant-Power Performance Results

All performance data at 5 kW and 6 kW are compiled into Figures 5.12(a) and 5.12(b). These plots show the tradeoff between thrust and anode specific impulse

Table 5.5: **6-kW operating conditions**

Discharge Voltage [V]	Inner Anode Mass Flow Rate [mg/s]	Outer Anode Mass FlowRate [mg/s]	Background Pressure [torr-Xe]
125	12.0	29.6	$2.7 \cdot 10^{-5}$
150	11.0	27.1	$2.4 \cdot 10^{-5}$
200	9.0	21.8	$1.8 \cdot 10^{-5}$
250	7.5	18.3	$1.6 \cdot 10^{-5}$
300	6.4	15.6	$1.3 \cdot 10^{-5}$
350	5.6	13.6	$1.2 \cdot 10^{-5}$
200	-	28.8	$1.8 \cdot 10^{-5}$
250	-	25.4	$1.6 \cdot 10^{-5}$
300	-	21.7	$1.3 \cdot 10^{-5}$
350	-	18.9	$1.2 \cdot 10^{-5}$
400	-	16.8	$1.0 \cdot 10^{-5}$
300	18.0	-	$1.1 \cdot 10^{-5}$
400	14.7	-	$8.8 \cdot 10^{-6}$
500	12.3	-	$7.3 \cdot 10^{-6}$
600	10.2	-	$6.1 \cdot 10^{-6}$

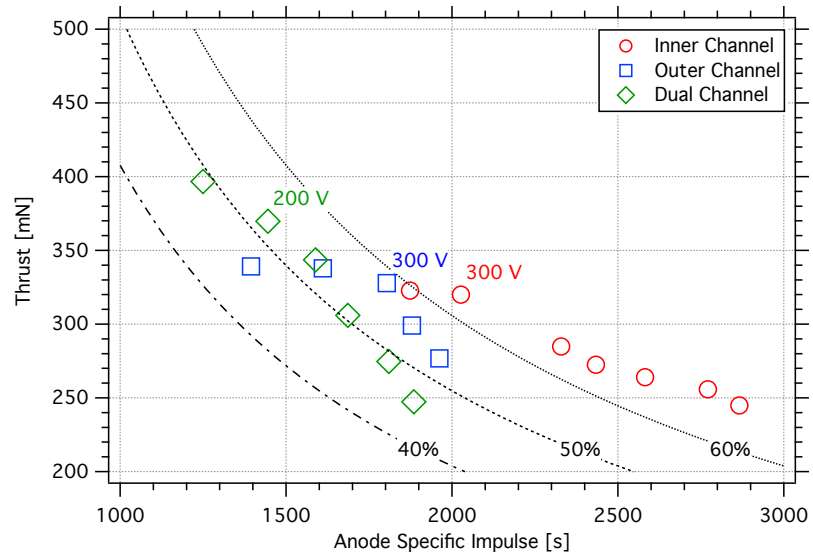

(a) 5 kW

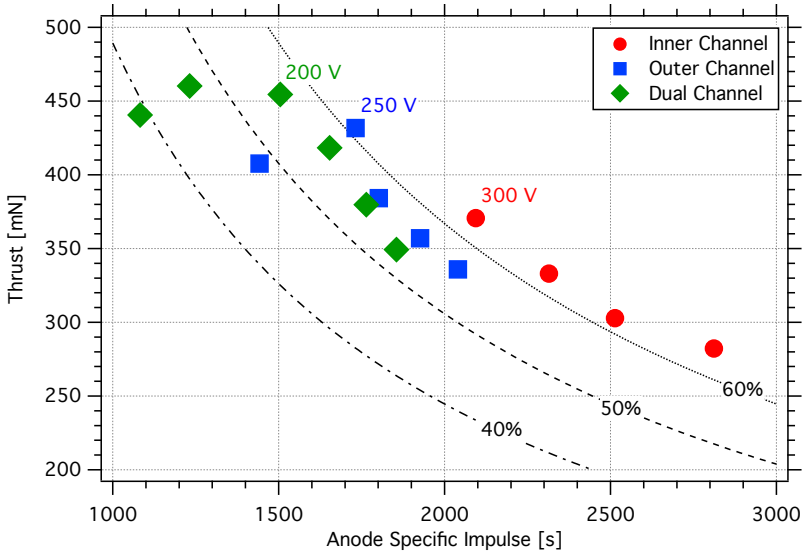

(b) 6 kW

Figure 5.12: **Thrust as a function of anode specific impulse at constant discharge power.** Thrust uncertainty is ±3 mN.

while operating at constant discharge power. Discharge voltages are indicated for one operating condition of each mode for reference. The achieved thrust ranges were 245 mN - 397 mN at 5 kW and 282 mN - 460 mN at 6 kW. Uncertainty in the thrust measurements was ±3 mN and uncertainty in anode specific impulse typically did not exceed ±115 s. Anode efficiency for the constant power data was accurate to ±3% absolute.

Both sets of constant-power data reflect the throttling scheme shown in Figure 3.4 and illustrate the ability of a NHT to transition between modes in order to optimize performance and extend its specific impulse range. Dual-channel operation produced the best performance up to approximately 1600 s $I_{sp,a}$. The range over which the outer channel was best varied with the operating power. At 5 kW, the outer channel took over between 1600 s and 1800 s $I_{sp,a}$, and at 6 kW, this range expands to 1600 s to 2050 s. Beyond 1800 s - 2050 s $I_{sp,a}$, optimal performance was provided by the inner channel. At both 5 kW and 6 kW, the outer channel reached conditions where its thrust began to plateau or decrease with decreasing specific impulse. By transitioning to dual-channel mode for low specific impulse, the limitations of the outer channel were avoided. The use of both channels also expanded the range of anode specific impulse 1000 s below the lowest demonstrated $I_{sp,a}$ of the inner channel, as the dual-channel mode provided up to twice the highest mass flow rate of the inner channel.

To examine the variation of performance at constant power in greater detail, thrust can be examined as a function of the discharge voltage and anode mass flow rate. These parameters were chosen because they were directly adjusted by the operator, as opposed to parameters, such as discharge current, that were indirectly controlled. The reader should note that both V_d and $\dot{m}_a$ were adjusted simultaneously between operating conditions. Figures 5.13(a) and 5.13(b) show the measured thrust as a function of discharge voltage while Figures 5.14(a) and 5.14(b) show thrust as a function of anode mass flow rate.

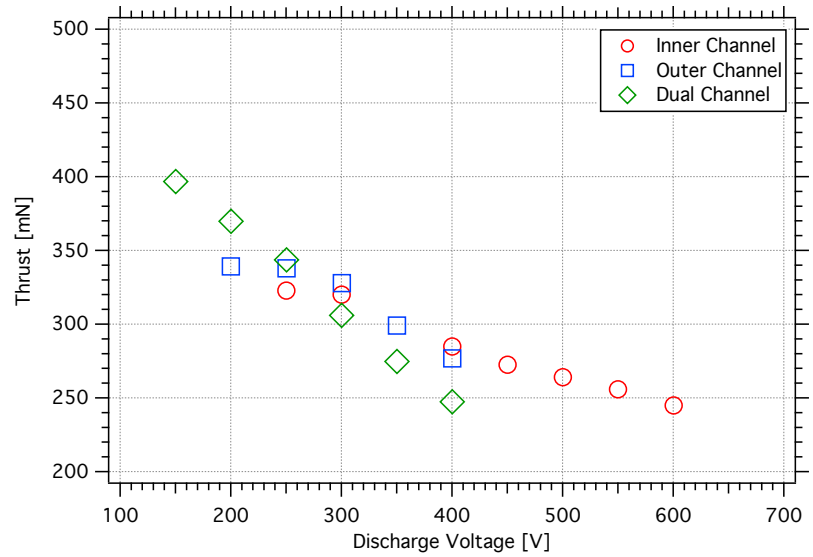

(a) 5 kW

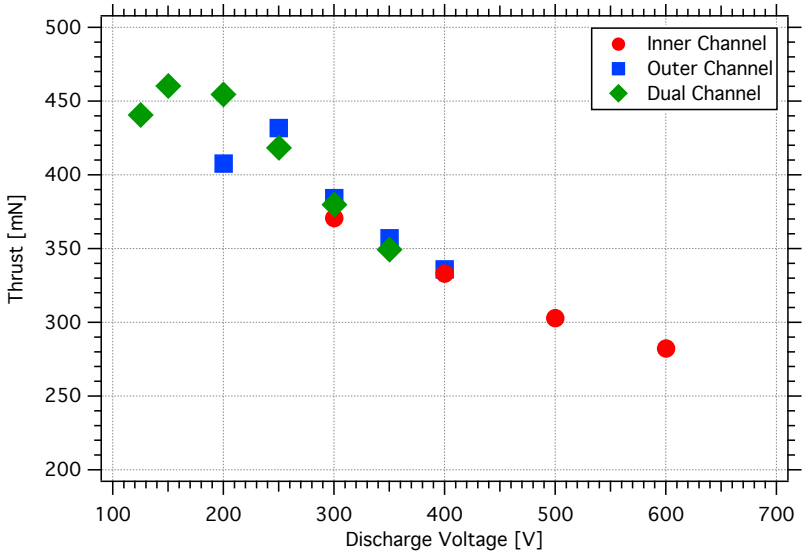

(b) 6 kW

Figure 5.13: **Measured thrust as a function of discharge voltage at constant discharge power.** Thrust uncertainty is ±3 mN.

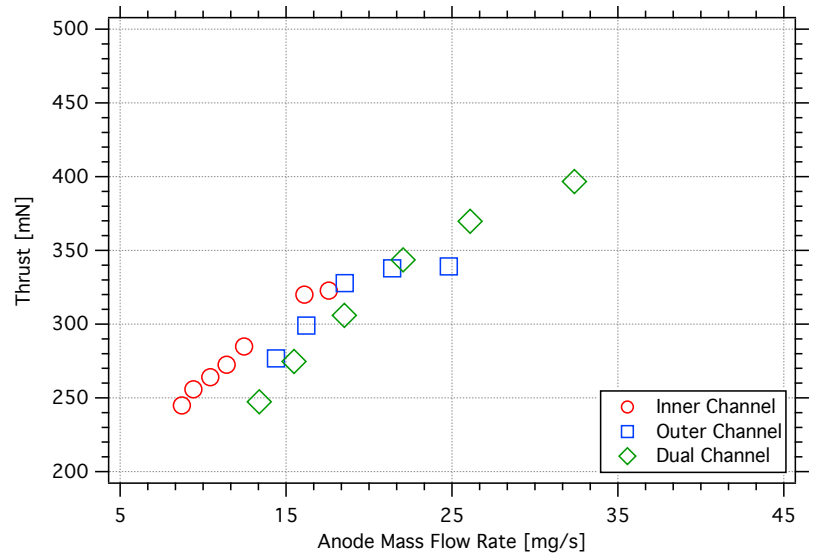

(a) 5 kW

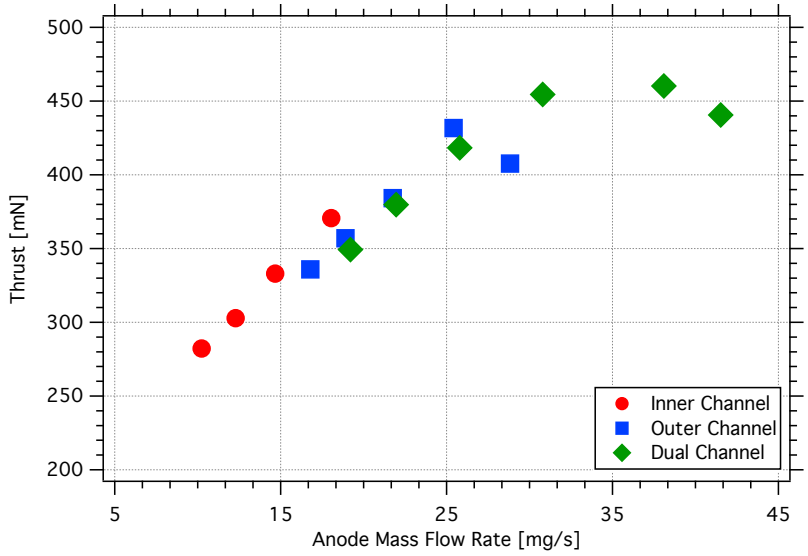

(b) 6 kW

Figure 5.14: **Measured thrust as a function of anode mass flow rate at constant discharge power.** Thrust uncertainty is ±3 mN.

The data in Figures 5.13(a)-5.14(b) provide a means of decomposing the operating ranges of each mode into discharge voltage and the corresponding mass flow rates. For constant-power operation, the dual-channel mode was well-suited for low discharge voltages up to 200 V - 250 V. The corresponding mass flow rates, which varied in magnitude based on the power, spanned the upper 44% of the 5-kW $\dot{m}_a$ range and the upper 50% of the 6-kW $\dot{m}_a$ range. The inner channel provided the best performance above 300 V - 400 V, covering the lower 38% and 28% of the $\dot{m}_a$ range at 5 kW and 6 kW, respectively. The intermediate discharge voltage and mass flow rates were covered by the outer channel.

Figures 5.15(a) and 5.15(b) show the anode efficiency and anode specific impulse for the 5-kW and 6-kW operating conditions. Anode efficiency varies from 39% to 68% while anode specific impulse varies from 1082 s to 2866 s. In general, the inner channel operates with the higher specific impulse than the other two modes of the X2, and therefore, it is particularly suited for high-voltage, high-I_{sp} operation. The inner channel is also more efficient, resulting in a small gap between the inner-channel and outer-channel curves in Figure 5.12(b).

The outer channel of the X2 is meant primarily to increase mass flow rate at low discharge voltages and does not operate the most efficiently at 300 V or above. This is most apparent in the 5-kW efficiency data, where the outer channel's anode efficiency decreases at 300 V and above. At 6 kW, η_a for the outer channel decreases from 250 V to 300 V and plateaus around 56%-58% up to 400 V. As the outer channel is dominant during dual-channel operation, efficiency of the dual-channel mode also decreases above 300 V. However, for more efficient operation, a transition can be made to the inner channel, which is meant for high-voltage operation.

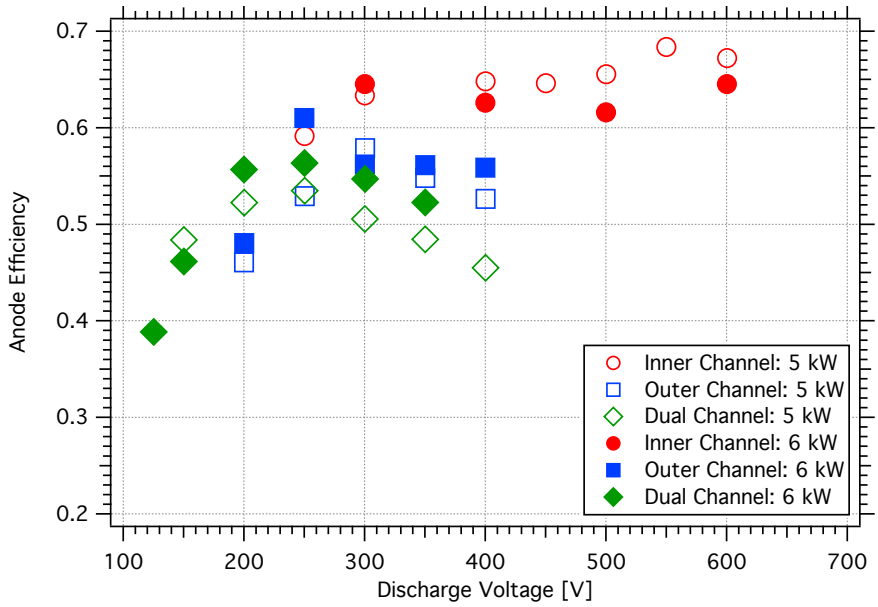

(a) Anode Efficiency

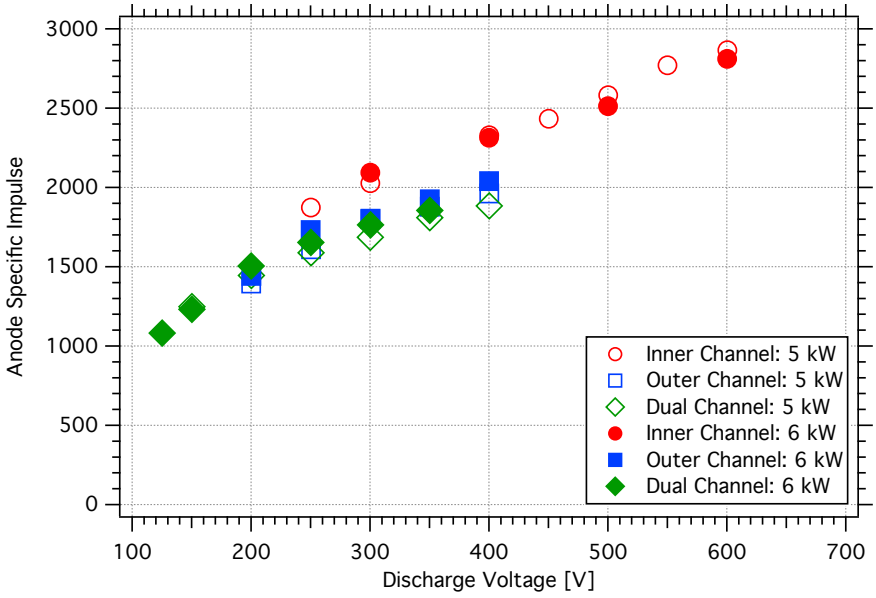

(b) Anode Specific Impulse

Figure 5.15: **Anode efficiency and anode specific impulse as a function of discharge voltage at constant discharge power.** For these data, the uncertainty in anode efficiency is up to ±3% absolute, and the uncertainty in anode specific impulse is no greater than ±115 s.

5.2.2 Summary of Constant-Power Performance Data

The X2 NHT demonstrated constant-power operation at 5 kW and 6 kW between approximately 1080 s and 2860 s anode specific impulse. With three combinations of exit area, the X2 was able to transition between dual-channel mode and two single-channel modes in order to optimize performance and avoid the limitations of any one configuration. For constant-power operation, using nested channels simultaneously was most advantageous in the high thrust-to-power regime at low discharge voltages, where the increased mass flow capability was most needed. Single-channel operation at fixed power was best suited for moderate and high specific impulse.

5.3 Summary

This chapter discussed the performance capabilities of the X2 NHT in both single-channel and dual-channel modes while maintaining constant mass flow rate and constant discharge power. Although some limitations were observed with the outer-channel and dual-channel modes, the high thrust-to-power data shows promising results for NHT operation. Small increases in performance were observed at low voltage, and these increases will become the basis for further investigation with plasma diagnostics, as discussed in Chapter VI.

CHAPTER VI

Plume Properties of a Nested Hall-Effect Thruster

The previous chapter showed the results from some of the first performance measurements on a nested Hall-effect thruster. At low discharge voltage, the X2 displayed small improvements in performance in dual-channel operation in comparison to single-channel operation. The thrust from a dual-channel condition exceeds the combined thrust measured from the component single-channel conditions. In short, the whole appears to be greater than the sum of the parts.

This chapter dives deeper into the dual-channel operating mode by looking at the discharge and plume characteristics. Studying this unique HET configuration prompted the use of the various plasma diagnostics described in Chapter IV. Each diagnostic provides some form of insight into the manner in which the X2 operates in dual-channel and single-channel mode. Section 6.1 shows the results of the RPA and E×B probe placed in the far field, and Section 6.2 discusses the results of the near-field Faraday probe. Internal measurements from the emissive and asymmetrical double Langmuir probe are shown in Section 6.3.

The results of plume measurements will also allow anode efficiency to be broken down into the utilization efficiencies discussed in Section 2.5. The diagnostics related to each efficiency is shown in Table 6.1.

Table 6.2 shows the single-channel and dual-channel operating conditions for which

Table 6.1: **Utilization efficiencies and their associated plume diagnostics**

Calculated Efficiency	Associated Diagnostics	Measurement Region
Charge Utilization	E×B probe	Far-field
Voltage Utilization	RPA and LP	Far-field
Current Utilization	FP	Near-field
Divergence	FP	Near-field
Mass Utilization	E×B probe	Far-field
	FP	Near-field

there are far-field, near-field, and internal measurements. For each dual-channel condition, an inner-channel condition and an outer-channel condition were performed under the same applied magnetic field and cathode flow fraction. The single-channel operating conditions are the closest approximation to how each channel operates during dual-channel mode. However, the influence of the adjacent plasma was naturally missing. Differences in plume properties between the two modes will reveal information about the changes occurring due to dual-channel operation.

This set of operating conditions is centered at the dual-channel condition with the highest thrust-to-power ratio: 150 V and 75% nominal mass flow rate. Discharge voltage and mass flow rate were changed across this condition of interest. Once again, the discharge voltages applied to both channels were the same, and the current densities of the two channels were nearly equal. The cathode flow fraction was kept constant at 10%.

6.1 Far-Field Measurements

Measurements from the E×B probe and RPA will show, respectively, the composition of charge states and ion voltages in the plume of the X2. As described in Section 4.2, each probe pointed directly down the middle of each discharge channel during data collection. The comparisons presented in this section will come in two sets: one set with the probes downstream of the inner-channel centerline and another

Table 6.2: **Plume diagnostic conditions**

Discharge Voltage [V]	Inner Mass Flow Rate [mg/s]	Outer Mass Flow Rate [mg/s]	Percent Nominal Flow Rate	Far-Field RPA and E×B Probe	Near-Field Faraday Probe	Internal and Near-Field Emissive Probe
150	4.7	11.6	50%	•	•	
100	7.0	17.4	75%	•		
125	7.0	17.4	75%		•	
150	7.0	17.4	75%	•	•	
200	7.0	17.4	75%	•	•	•
150	9.3	23.2	100%	•	•	
150	4.7	-	50%	•	•	
100	7.0	-	75%	•		
125	7.0	-	75%		•	
150	7.0	-	75%	•	•	
200	7.0	-	75%	•	•	•
150	9.3	-	100%	•	•	
150	-	11.6	50%	•	•	
100	-	17.4	75%	•		
125	-	17.4	75%		•	
150	-	17.4	75%	•	•	
200	-	17.4	75%	•	•	•
150	-	23.2	100%	•	•	

set with the probes downstream of the outer-channel centerline.

6.1.1 E×B Probe Spectra

Looking for established trends can serve as a good starting point for plumes measurements on a new thruster configuration. The E×B spectra collected on the X2 show many of the expected variations with respect to discharge voltage and flow rate. Figures 6.1(a) - 6.1(f) show measurements with varying discharge voltage at constant mass flow rate combination of 7.0+17.4 mg/s, while Figures 6.2(a) - 6.2(f) display measurements at varying flow rates at 150 V.

With increasing discharge voltage and mass flow rate, the fraction of multiply-charged ions generally increases, but for all operating conditions, singly-charged xenon ions make up the vast majority of beam ions regardless of the source channel or operating mode. Singly- and doubly-charged ions dominate at 100 V, and increasing discharge voltage generally increases the current fractions for multiply-charge species. Quadruply-charged xenon remained largely undetectable until 200 V, where the corresponding current fraction Ω_4 was approximately 0.01.

The variation in current fractions show that the dual-channel conditions tend to create more multiply-charged species, particularly triply-charged ions, but there also exist some dual-channel conditions with comparable or higher fractions of singly-charged ions. Shown as functions of discharge voltage and mass flow rate in Figures 6.3(a)-6.3(d), the singly-charged current fractions are lower for most dual-channel conditions, and measurements along the inner channel show the most consistent increases in triply-charged ions in dual-channel mode. The effect of operating mode on the current fraction of doubly-charged ions is less clear, as the dual-channel mode does not consistently create more or less Xe^{2+}.

Examination of species fractions shows similar trends to the data shown on current fractions. However, current fractions will determine both average charge and charge

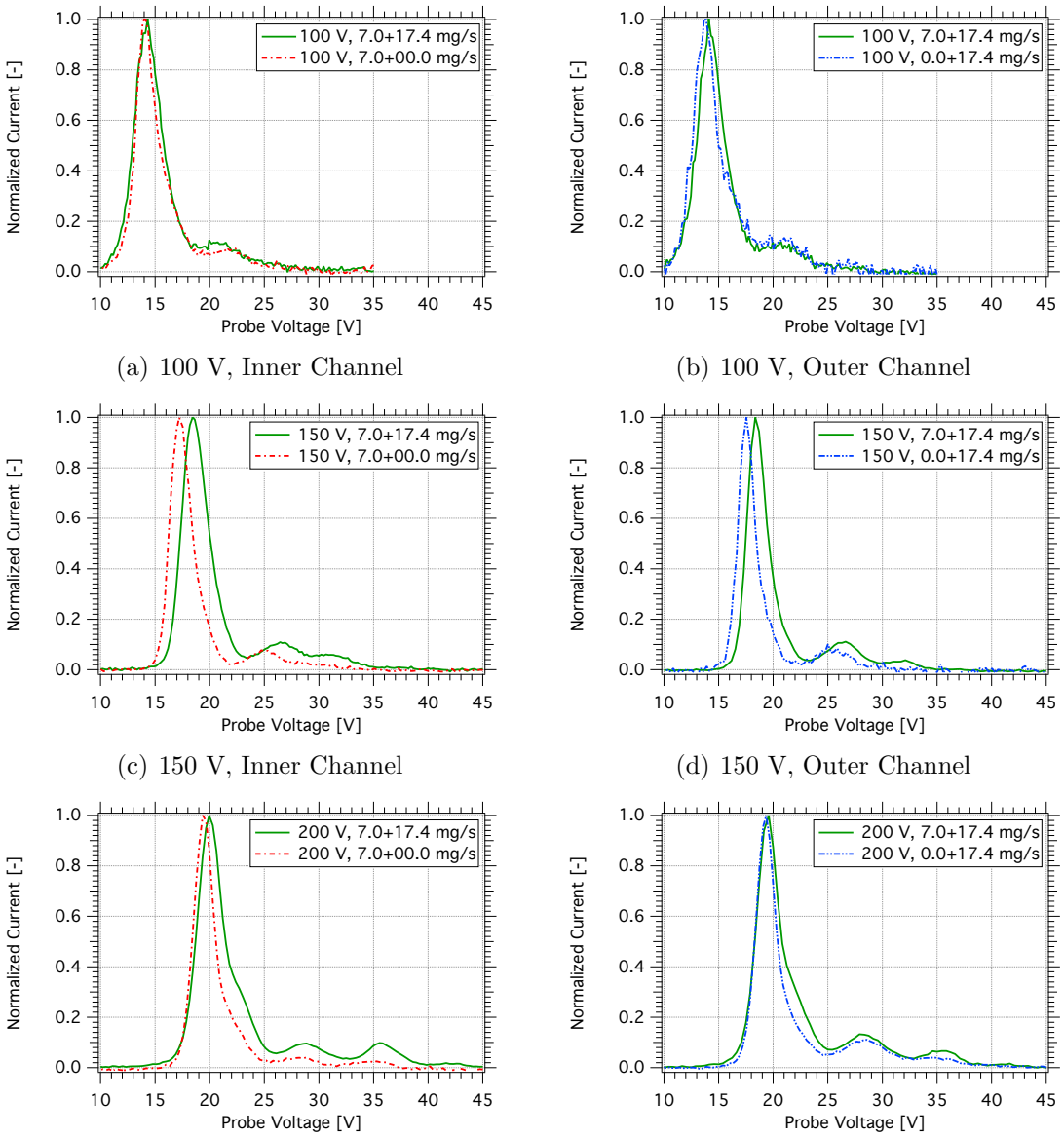

(a) 100 V, Inner Channel

(b) 100 V, Outer Channel

(c) 150 V, Inner Channel

(d) 150 V, Outer Channel

(e) 200 V, Inner Channel

(f) 200 V, Outer Channel

Figure 6.1: **Single-channel and dual-channel E×B probe spectra at fixed flow rate (75% nominal).**

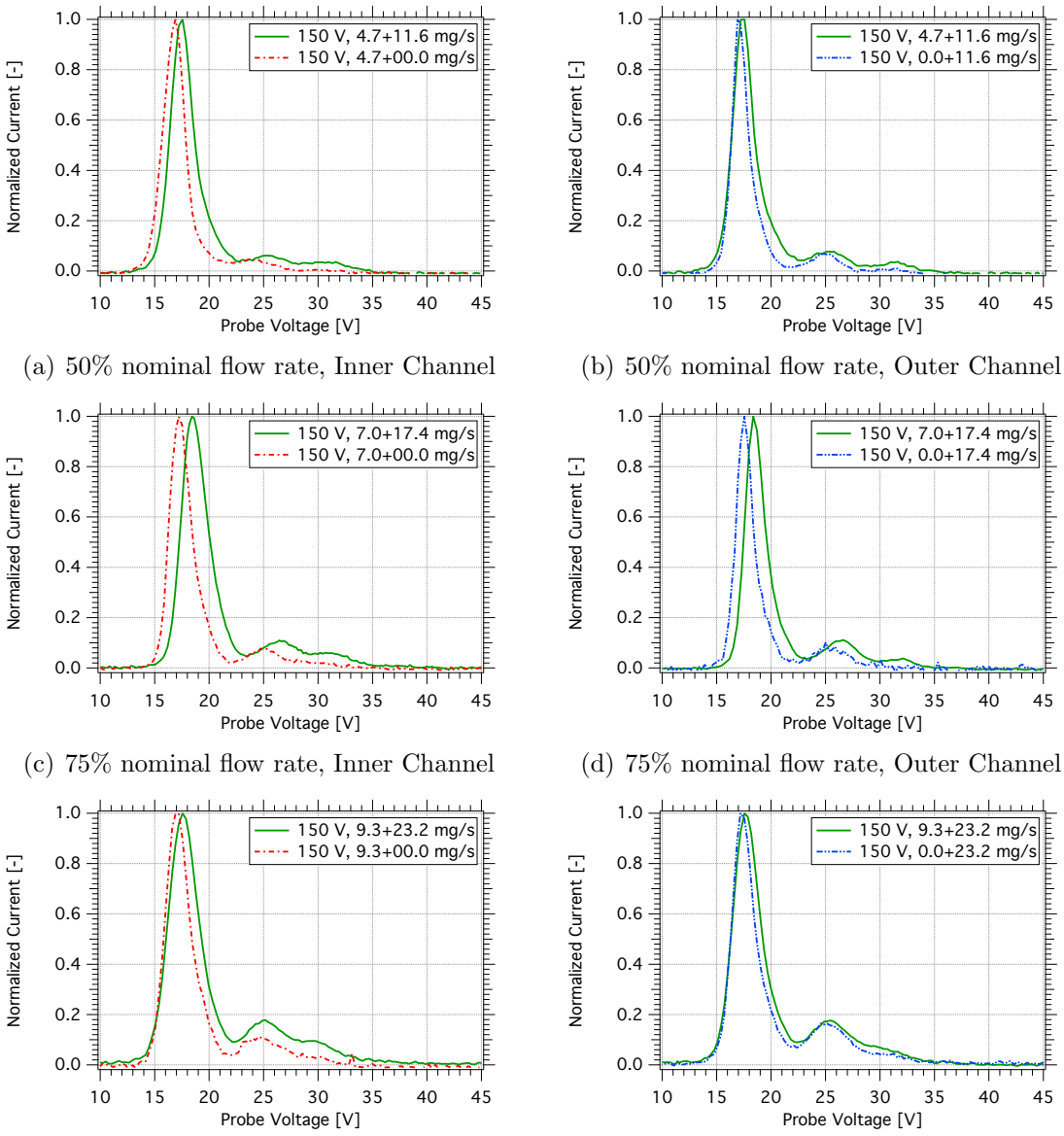

(a) 50% nominal flow rate, Inner Channel

(b) 50% nominal flow rate, Outer Channel

(c) 75% nominal flow rate, Inner Channel

(d) 75% nominal flow rate, Outer Channel

(e) 100% nominal flow rate, Inner Channel

(f) 100% nominal flow rate, Outer Channel

Figure 6.2: **Single-channel and dual-channel E×B probe spectra at fixed discharge voltage (150 V).**

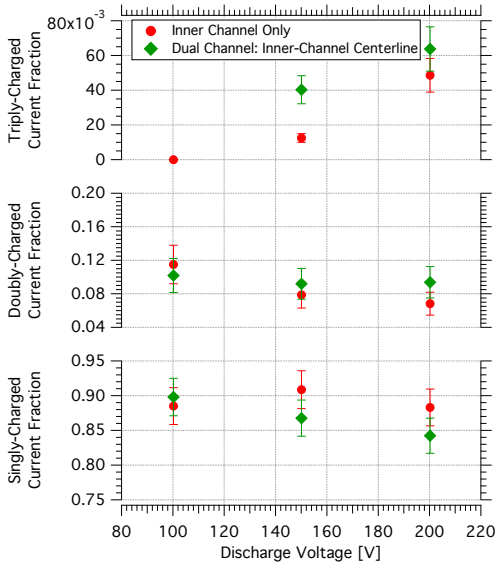

(a) Inner-Channel Variation with Voltage

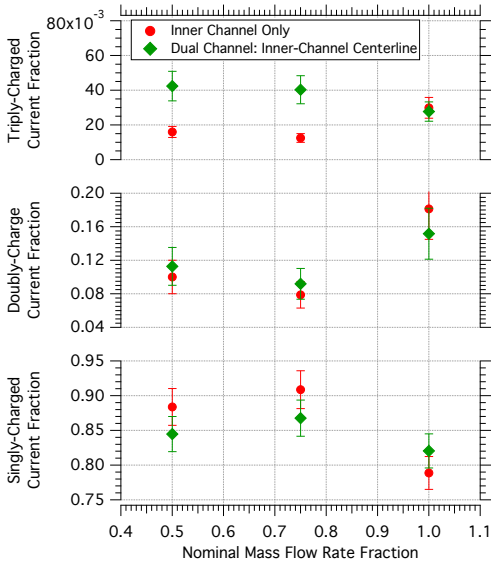

(b) Inner-Channel Variation with Mass Flow Rate

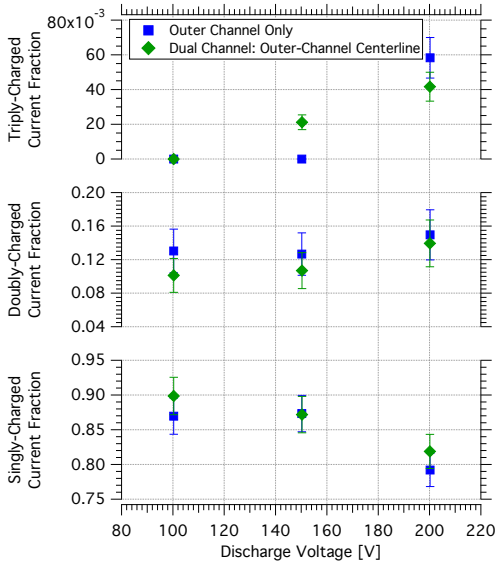

(c) Outer-Channel Variation with Voltage

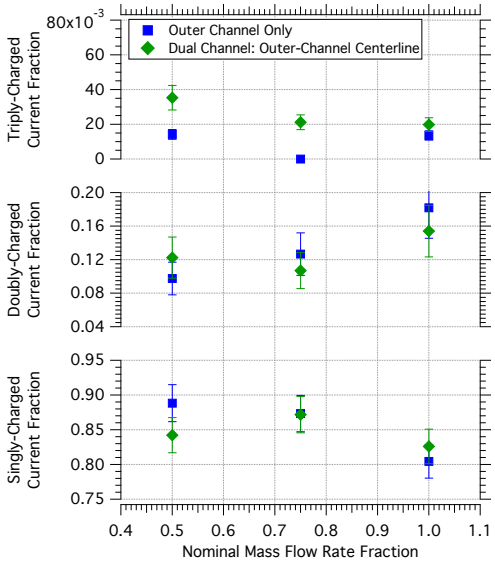

(d) Outer-Channel Variation with Mass Flow Rate

Figure 6.3: **Current fractions measured with the E×B probe along inner-channel and outer-channel centerlines**

utilization efficiency. As such, the discussion of current fractions is marginally more relevant.

Depending on the operating condition, small variations in the charge species composition can exist within a dual-channel plume. Figures 6.4(a) and 6.4(b) show two examples of E×B spectra in dual-channel mode. Measurements taken at 150 V, 4.7+11.6 mg/s show negligible differences between the inner channel and outer channel, but the spectra from 200 V, 7.0+17.4 mg/s show small shifts in the probe voltage and relative amplitudes in the multiply-charge species peaks. As shown in Equation 4.2, shifts in voltage indicate changes in the ion pass velocities.

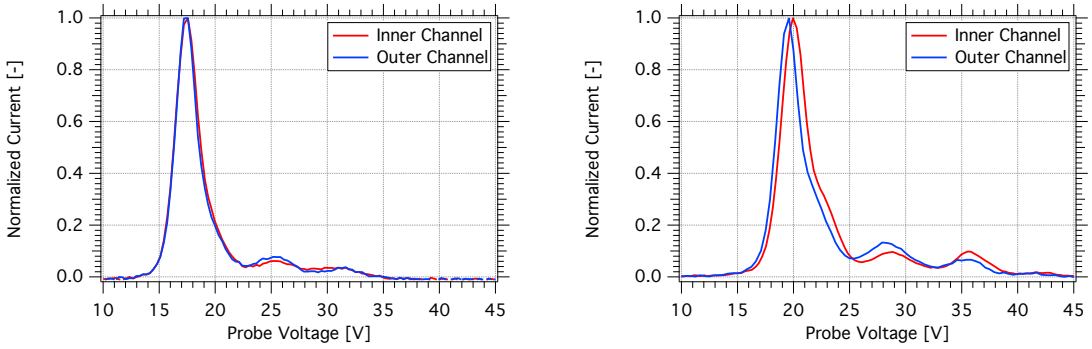

(a) 150V, 4.7+11.6 mg/s

(b) 200 V, 7.0+17.4 mg/s

Figure 6.4: **Dual-channel E×B probe spectra**

The differences between the discharge channels are ultimately small after converting the data in these spectra into physical quantities. For the 200 V condition, the difference in the singly-charged ion pass velocities is approximately 200 m/s, which is less than 2% of the absolute pass velocities of 12.8 km/s and 12.6 km/s for the inner and outer channel, respectively. Current fraction and species fraction variation is also small. Of all the conditions from Table 6.2, the greatest variation between two channels in dual-channel mode was 3% in current fraction and 1% in species fraction.

Relative to the corresponding single-channel spectra, most of the dual-channel spectra are also shifted to higher applied voltages. As noted in Equation 4.2, the applied voltage is proportional to the velocity of the ions passing through the test sec-

tion. This shift in the peaks of all charge species suggests that the ions arriving from the thruster are moving faster during dual-channel operation than in single-channel operation. This is one indication that improved ion acceleration may contribute to the performance gains observed on the thrust stand.

6.1.2 Ion Voltage Distributions

Measurements from the RPA also show many expected trends seen in HET ion voltage distributions. The ion acceleration voltage increases with discharge voltage, as expected for a device that accelerates ions electrostatically. Figures 6.5(a) - 6.5(f) show the ion voltage distributions at constant mass flow rate and increasing discharge voltage, while Figures 6.6(a) - 6.6(f) show data with increasing mass flow rate at constant discharge voltage. The value of V_a is less sensitive to mass flow rate and appears to maximize at the 75% mass flow rate combination in dual-channel mode. Single-channel conditions show almost no change in V_a with respect to mass flow rate, with the exception of the inner channel at 50% nominal mass flow rate. The reduced voltage utilization efficiency at 50% nominal $\dot{m}$, along with its odd ion voltage utilization, most likely originate from poor coupling to the cathode due to the low flow rates. Calculation of the cathode coupling voltages in Section 7.1 shows that the highest V_c occur at the lowest flow condition.

In a manner similar to the E×B spectra, the ion voltage distributions show only small changes between channels in dual-channel modes. Due to the large acceptance angle of the RPA, discrimination between inner-channel ion and outer-channel ions is not possible. Figures 6.7(a) and 6.7(b) show comparisons at 150 V and 200 V at the 75% nominal mass flow rate combination. Differences in V_a between channels did not exceed 2.2 V for all dual-channel conditions. When compiled with the internal measurements in Section 6.3, these measurements show that the difference in V_a between channels with the same V_d is no greater than 2 V.

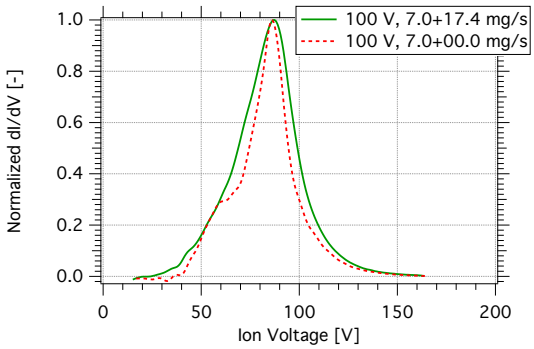

(a) 100 V, Inner Channel

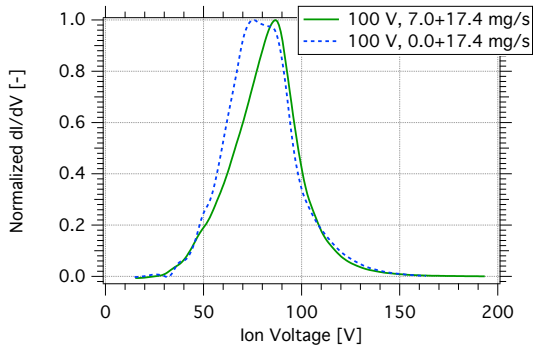

(b) 100 V, Outer Channel

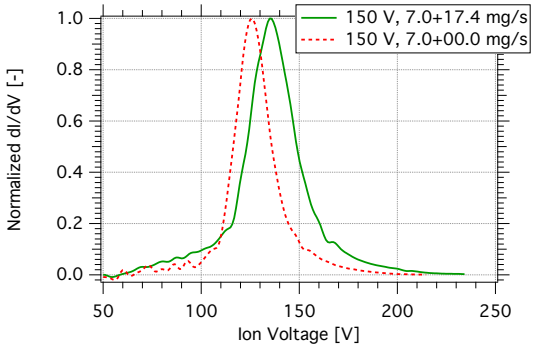

(c) 150 V, Inner Channel

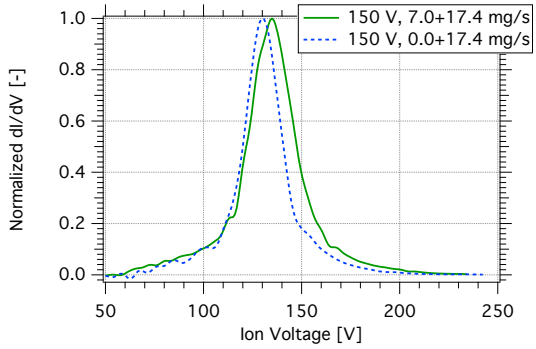

(d) 150 V, Outer Channel

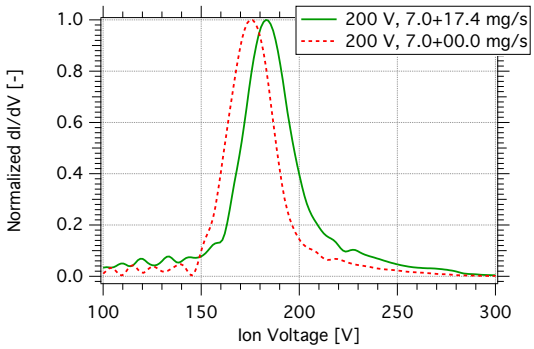

(e) 200 V, Inner Channel

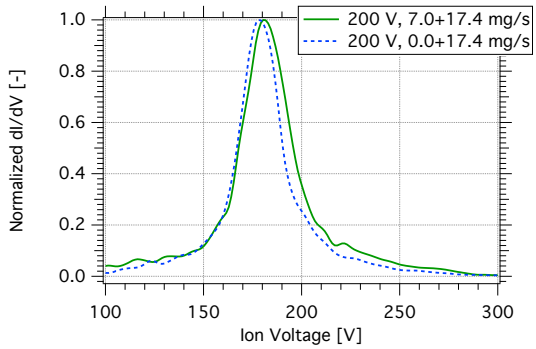

(f) 200 V, Outer Channel

Figure 6.5: **Single-channel and dual-channel ion voltage distributions at fixed flow rate (75% nominal).**

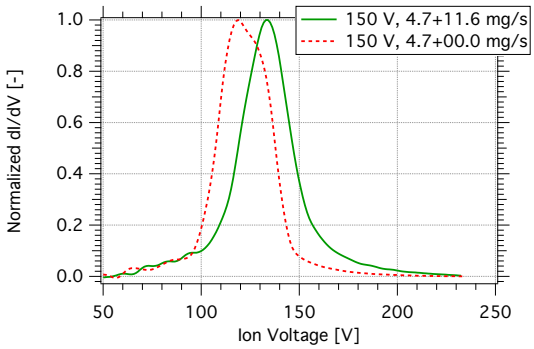

(a) 50% nominal flow rate, Inner Channel

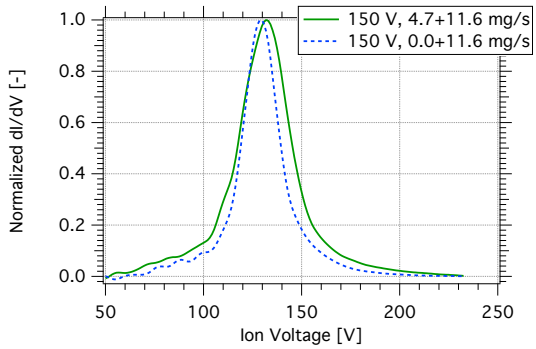

(b) 50% nominal flow rate, Outer Channel

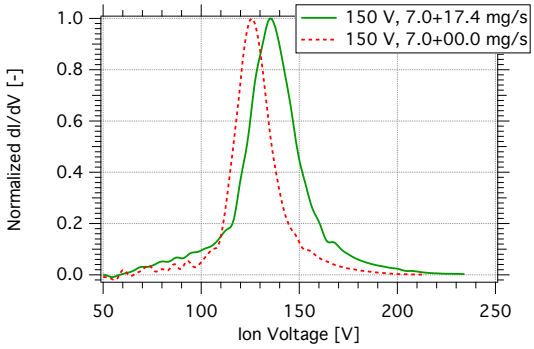

(c) 75% nominal flow rate, Inner Channel

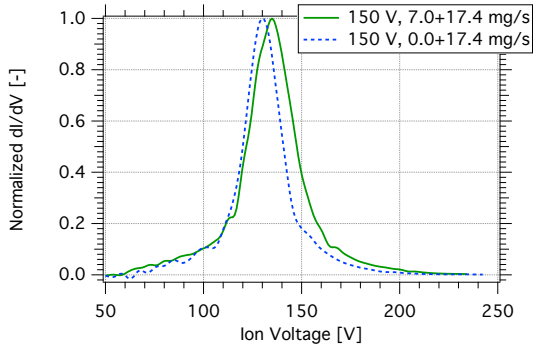

(d) 75% nominal flow rate, Outer Channel

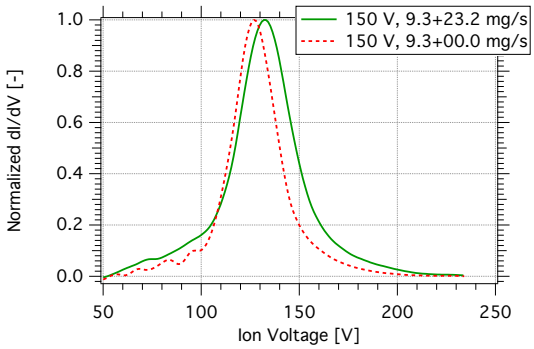

(e) 100% nominal flow rate, Inner Channel

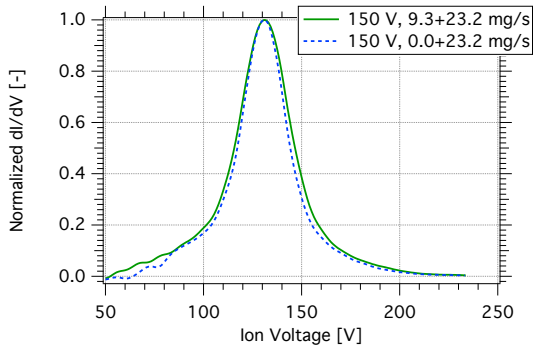

(f) 100% nominal flow rate, Outer Channel

Figure 6.6: **Single-channel and dual-channel ion voltage distributions at fixed discharge voltage (150 V).**

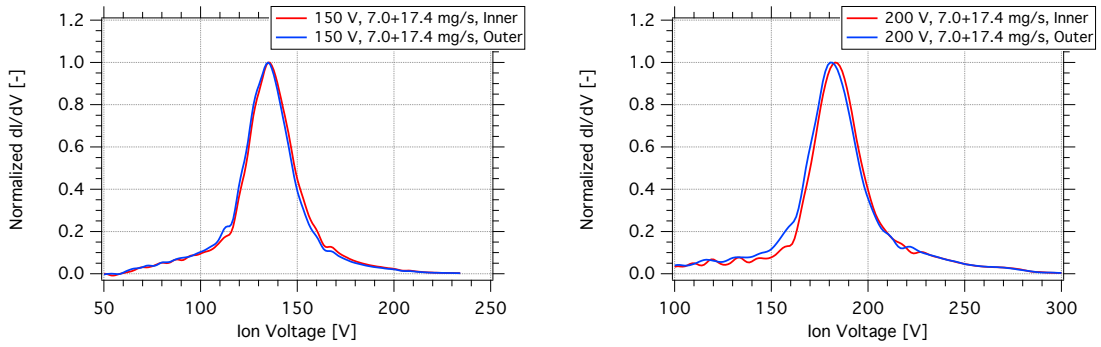

(a) 150V, 7.0+17.4 mg/s

(b) 200 V, 7.0+17.4 mg/s

Figure 6.7: **Dual-channel ion voltage distributions**

Comparisons between the single-channel and dual-channel ion voltage distributions reflect the trends observed in the E×B spectra. In all cases, the dual-channel conditions displayed acceleration voltages that were comparable or greater than those for the corresponding single-channel conditions. Once again, improved ion acceleration appears to be a contributing factor to the performance increases in dual-channel mode.

6.1.3 Measurements under Mixed-Voltage Operation

To this point, ions in a dual-channel plume appear to be very similar in both charge species composition and their acceleration voltage, regardless of the source channel. The discharge voltage applied to each channel was the same, so significant differences between channels would be unexpected. However, at unequal discharge voltages, the channels should produce ions with different exhaust velocities and perhaps even varying fraction of multiply-charge species, depending on the voltage difference.

Figures 6.8(a) and 6.8(b) show data from measurement collected to test this small hypothesis. The mass flow rate combination is 7.0+17.4 mg/s at 10% CFF. In this case, the inner-channel discharge voltage was 150 V and the outer channel was at 300 V. All probes pointed down the center of the inner channel during collection of the data shown in these figures.

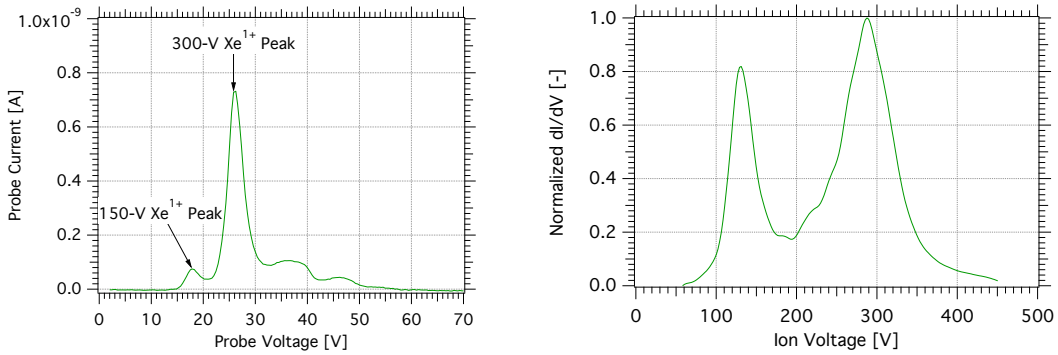

(a) E×B probe spectrum

(b) Ion voltage distribution

Figure 6.8: **E×B probe spectrum and ion voltage distribution from a mixed-voltage condition: 150V, 7.0 mg/s on the inner channel, 300V, 17.4 mg/s on the outer channel**

Ions from both channels clearly reached the far-field probes, which was expected for the RPA and unexpected for the E×B probe. The E×B probe's front collimator has an acceptance angle of 1.3 deg, and the acceptance cone projected onto the exit plane is not sufficiently large to encompass both discharge channels. As a result, ions from the outer channel must have undergone sufficient scattering to enter the E×B probe.

Under mixed-voltage operation, singly-charged ions from the inner channel appear in the E×B probe spectrum as a minor peak before the outer channel's dominant singly-charged peak. The shift in probe voltage accounts for the difference in ion velocities due to the difference in discharge voltages. Multiply-charged species from the inner channel become drowned out by the outer channel's singly- and multiply-charged ions, which are greater in number and energy.

The ion voltage spectrum from the RPA illustrates the bimodal distribution of beam ions. The peaks indicate the two populations from the separate channels while also showing the wide acceptance angle of the RPA. Both the inner-channel and outer-channel primary peaks are well-defined and indicate acceleration voltages at 87% and 96% of the applied inner- and outer- discharge voltages.

The performance of this mixed-voltage condition is not particularly special but does demonstrate a unique NHT capability. If both channels operated at 200 V for the same mass flow rate combination, anode efficiency would rise approximately 3% and the T/P_d would increase 12 mN/kW in comparison to the 150V/300V mix. However, should some application require two (or more) ion populations, a NHT may be a viable solution.

6.1.4 Summary

Measurements in the far-field revealed some details on the changes in thruster operation between single-channel and dual-channel mode. Generally, operating both channels increases the production of multiply-charge ions, indicating additional ionizing collisions in the plasma. The acceleration voltage also increases in dual-channel mode, and the higher ion velocities appear in the E×B probe spectra.

Both far-field probes indicate that improved ion acceleration is a contributing factor to the increased performance when firing both channels simultaneously. Additional energy is also spent ionizing propellant to higher charge states. These effects will be discussed further in Chapter VII, particularly in Section 7.2.

6.2 Near-Field Current Density

Measurements using the method described by Reid [70] produced spatial maps of the near-field ion current density j. The extent and resolution of these maps show details of the near-field plume structure of the X2 in both operating modes. The individual beam currents and divergence angles of each channel are of particular interest, as these data will permit more direct comparisons between single-channel and dual-channel modes.

For the near-field current density measurements, 125-V operating conditions replaced the 100-V operating conditions at the 75% nominal mass flow rates. The

original intent was to replace all measurements at 100 V with data at 125 V in order to characterize the X2 in a regime with better performance. The mass flow rate combinations remained the same for 125 V, and new magnet settings were determined by minimization of the discharge current. Unfortunately, time restrictions precluded performance and far-field measurements at the 125-V conditions, but the availability of beam currents and divergence angles will allow the observation of trends with respect to discharge voltage.

Figures in this section will display data with normalized axial and radial dimensions. The outer-channel mean diameter d_{OC} is the reference length, as the outer channel is naturally the more dominant source of beam ions. For reference, the ratio of the mean diameters d_{IC}/d_{OC} is approximately 0.4.

6.2.1 Evolution of a Dual-Channel Plume

Near-field measurements on single-channel HETs show different stages of blending of beam ions, and the X2 plume exhibits a number of the same characteristics in dual-channel mode. The region nearest to the exit plane shows distinct peaks corresponding to the ion current from each individual channel. As each individual plume expands, two forms of blending occur: centerline and inter-channel. The first type of blending is common to single-channel HETs, even between those with a center-mounted cathode [56, 70, 83] and an external cathode [84]. Inter-channel blending is naturally a product of the nested configuration and occurs within the same axial domain as the blending on centerline. In the furthest region of the near-field (typically beyond 0.4-0.6 d_{OC}), all the current density peaks combine into a single plume.

Figure 6.9 shows the radial distribution of ion current density at three axial positions for 200 V, 7.0+17.4 mg/s. The profile at $0.12d_{OC}$ shows the region nearest to the exit plane where the peaks along the centerline and the two channels are clearly distinguishable. At $0.24d_{OC}$, the plumes from each channel are already in the pro-

cess of merging together along with the peak along centerline. By $0.50d_{OC}$, only the centerline peak remains as a distinguishing feature in the plume.

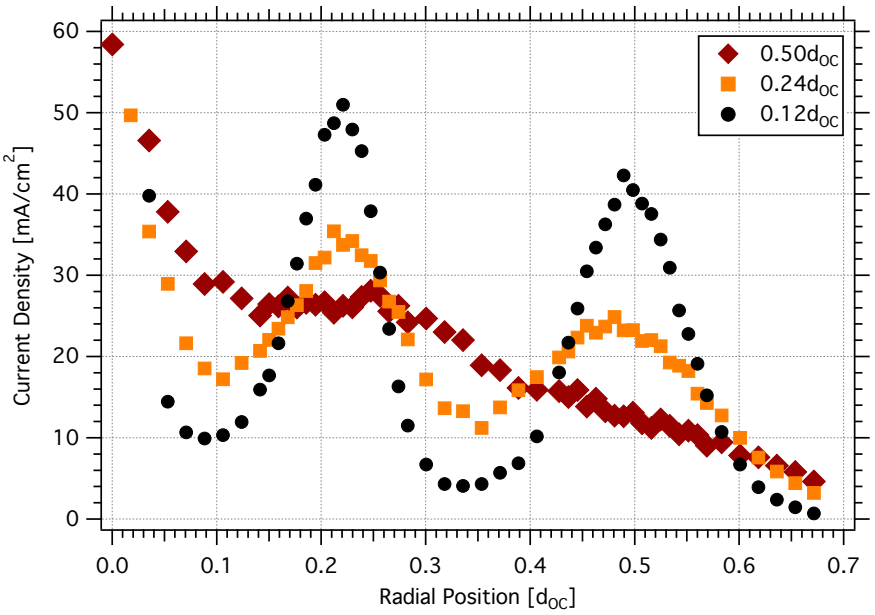

Figure 6.9: **Radial current density profiles at three axial distances from the exit plane**

The changes in the near-field ion current density become the most interesting when the channel plumes merge together in front of the inner channel. Shown in Figure 6.10, the inner-channel peak at Z = $0.24d_{OC}$ becomes elevated well above the outer-channel peak as well as the peaks measured in the single-channel modes. Fits to the dual-channel radial ion current density profile resemble a cascade of Gaussian peaks. Both channels produce expanding beams of ion current, and at sufficient axial distances from the exit plane, ion current originating from one channel will pass in front of the other channel. As the outer beam current is more than twice the inner beam current, the expansion of outer ion current inward dominates and elevates the inner channel peak. This effect produces the cascading Gaussian distribution seen at Z = $0.24d_{OC}$.

Integration of the radial current density profiles becomes less straightforward as the individual channel plumes begin to merge together. The single-channel profiles

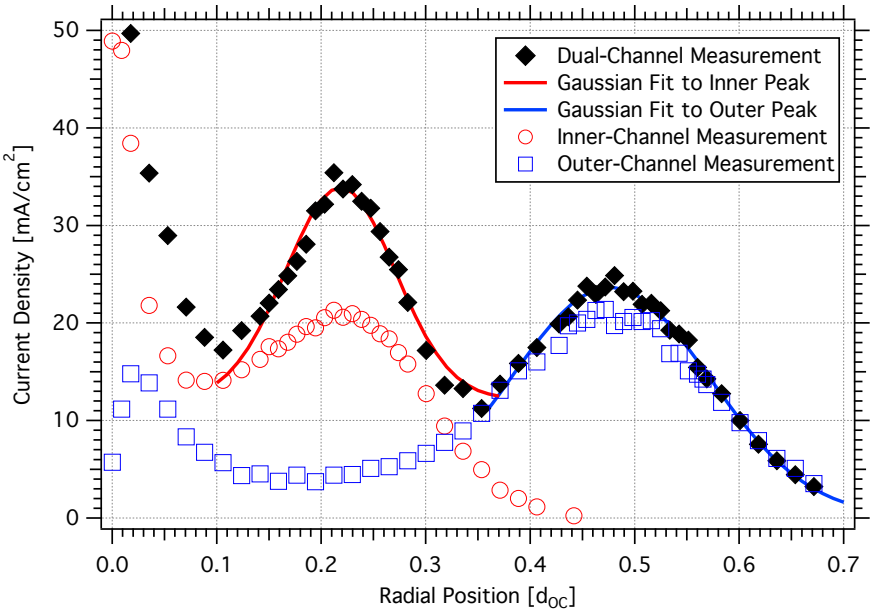

Figure 6.10: **Radial current density profile showing elevated inner-channel ion current density. All data are from the same axial position of Z = 0.24d_{OC}**

in Figure 6.10 show ion current from one channel will expand into the domain of the other channel, and there will exist an axial position beyond which the ion beam cannot be considered spatially separated. This expansion makes radial limits of integration insufficient to isolate one channel's beam current from the other channel's beam current. To avoid such ambiguity, the integrated beam currents shown in this section will originate from the region before peak blending becomes sufficiently significant to obscure $j_{k,\text{peak}}/e$. This region occurred within axial distances between $0.16d_{OC}$ and $0.21d_{OC}$ for the operating conditions shown here.

6.2.2 Consideration for Neutral Ingestion of Background Gas

The increases in ion current density are also evident close to the exit plane, where each channel's plume is well-defined and spatially isolated. Figure 6.11 provides the current density distribution at $0.04d_{OC}$ for 200 V, 7.0+17.4 mg/s for all modes. When operating individually, the current densities of both channels are nearly equal at 65

mA/cm^2 close to the exit plane. In dual-channel operation, the inner-channel peak increases by 13.2 mA/cm^2 while the outer-channel peak increases by 5.8 mA/cm^2 at $0.04d_{OC}$. In a similar manner to the profile at $0.24d_{OC}$, the inner-channel peak increases more than the outer-channel peak between operating modes.

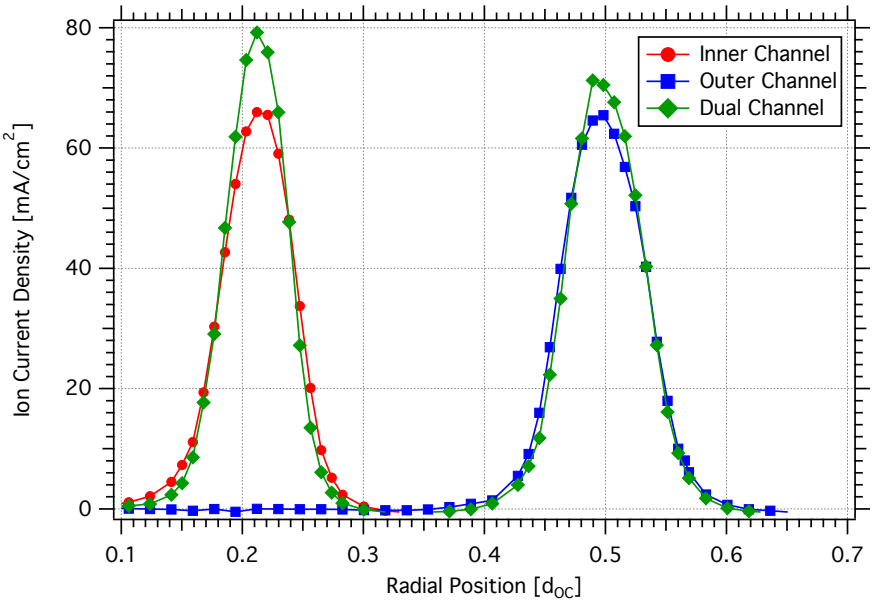

Figure 6.11: **Radial current density profiles for all operating modes at $0.04d_{OC}$.**

Considering that the anode mass flow rates remained the same between modes, each channel required another source of neutrals to create the additional beam ions. Significantly increased production of multiply-charged ions is another possible cause of the increased current densities, but measurements from the E×B probe in Section 6.1 do not show consistent and significant increases in multiply-charge species in dual-channel mode. As a result, neutral ingestion becomes the most probable cause of the elevated ion current densities. The leading sources of additional neutrals would be the adjacent channel and the background gas. Additional flow also originates from the cathode operating at constant CFF, but the change in cathode mass flow rate is much smaller than the change in anode mass flow rate. The following analysis will consider the effect of the background gas alone on the ion current density measurements.

Based on prior work by Randolph [79], a kinetic model for the ingestion or entrainment of background neutrals can provide estimates on the increase in current density due to increased facility neutral density. Previous use of this method by Walker [62] and Reid [39] required the use of an effective ingestion area in order to convert mass flux into mass flow rate or discharge current. Reid introduced the use of a hemispherical ingestion area, as the exit area tended to underestimate the entrained discharge current. This discussion of entrained background particles will stay in flux quantities (particle flux and charge flux) due to insufficient data to determine an effective, nested ingestion area.

Assuming a Maxwellian background neutral gas, the random (entrained) particle flux into the thruster is:

$$\Phi_{en} = \frac{1}{4} n_b \sqrt{\frac{8 k_B T}{\pi m_{Xe}}} \tag{6.1}$$

An equal flux of background particles must move away from the thruster such that there is not an unphysical continuous accumulation of mass. In the most extreme case, all background neutrals would become ionized and leave as additional ions, hereafter called entrained ions. As the majority of neutrals injected from the anode become singly charged, a reasonable assumption would be a singly-charged ionization state for ionized entrained neutrals. These entrained ions would form an outward current density j_{en} equal to:

$$j_{en} = e\Phi_{en} = \frac{1}{4} e n_b \sqrt{\frac{8 k_B T}{\pi m_{Xe}}} \tag{6.2}$$

Equation 6.2 estimates the absolute entrained current density, but given the comparison of operating modes shown in Figure 6.10, the change in entrained current density Δj_{en} is more useful, as shown in Equation 6.3.

$$\Delta j_{en} = \frac{e}{4}(\Delta n_b)\sqrt{\frac{8k_BT}{\pi m_{Xe}}} = e(\Delta p_c)\sqrt{\frac{1}{2\pi m_{Xe}k_BT}} \tag{6.3}$$

With the additional assumption of background gas temperatures of 300 K, the estimates of entrained current density for all operating conditions are insufficiently large to completely account for the increases seen in near-field measurements. The inner channel sees the greatest pressure difference between single-channel and dual-channel operation. With the 200-V condition as an example, the pressure difference of $8.7{\cdot}10^{-6}$ torr results in only 0.25 mA/cm^2 of additional current density, according to Equation 6.3. For the outer channel, the increase would be 0.09 mA/cm^2. Of all operating conditions, the estimation for Δj_{en} did not exceed 0.35 mA/cm^2 for inner-channel conditions and 0.14 mA/cm^2 for outer-channel conditions. The observed increases in ion current density exceed these estimates by over an order of magnitude.

6.2.3 Effects of Facility Background Pressure on Near-Field Current Density

For Faraday probes, elevated background pressure p_c can alter the measured ion current density through effects such as neutral ingestion and charge-exchange collisions. The effect of charge-exchange ions are well-known for far-field Faraday probe measurements [85, 86] where the indicated current density tends to increase with p_c in the periphery of the plume. Near-field measurements are generally considered less sensitive to background charge exchange [70]. For the X2, data at three background pressures were collected to check that near-field current density measurements are actually dominated by ion current from the thruster instead of background CEX ions.

The primary effect of increasing p_c appears to be an axial shift in the near-field ion current density, as changes in the ion current density are not globally linear nor globally unidirectional with increasing p_c. Figure 6.12(a) shows ion current measure-

ments along the centerline of the outer channel before and after averaging. The raw measurements show negligibly small changes due to background pressure, and the averaged results show axial shifts, primarily within $0.5d_{OC}$ of the exit plane.

The two-dimensional ion current density maps in Figures 6.13(a) - 6.13(c) along with the short animation in Figure 6.14 provide views of the near-field variations with background pressure. Near the exit of each channel, the current density peaks shift further downstream with increasing p_c. Additionally, the axial positions where blending occurs also shift downstream and the plumes becomes more extended from z = 0. Considering shifts in the acceleration zone due to background pressure [87], the observed changes in the near-field are more likely the result of changing thruster behavior instead of global increases in CEX ion density due to higher p_c.

As a result, correction of near-field current density measurements for back pressure effects would first require an adjustment for changes in thruster operation. Due to the variation in both thruster behavior, changes in the measurement cannot be purely isolated. Instead, these measurements will quantify the variations in integrated beam current and divergence angle with background pressure, and the observed changes will become part of the measurement uncertainty.

Determining the variation in I_b and β with p_c will provide bounds for the uncertainty in these quantities due to the variability in thruster operation. Integrated beam currents showed no clear trends with background pressure, as shown in Figure 6.15(a). For the inner channel, the I_b decreased and then increased slightly with increasing p_c, while the opposite occurred for the outer channel. A linear fit and extrapolation to vacuum shows an uncertainty of only 2% in I_b.

The variation in divergence angle is closer to linear and shows greater variation over the tested background pressures, as shown in Figure 6.15(b). In both cases, the divergence angle decreased with increasing pressure, and a linear extrapolation to zero pressure yields an additional uncertainty of 18%. The trend of β with respect to

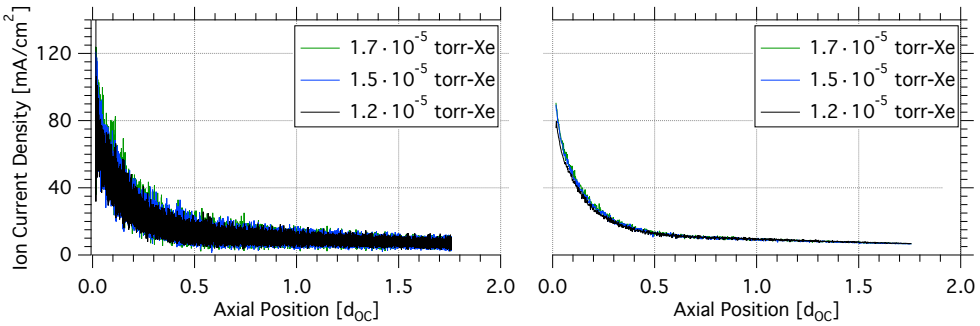

(a) All Pressures

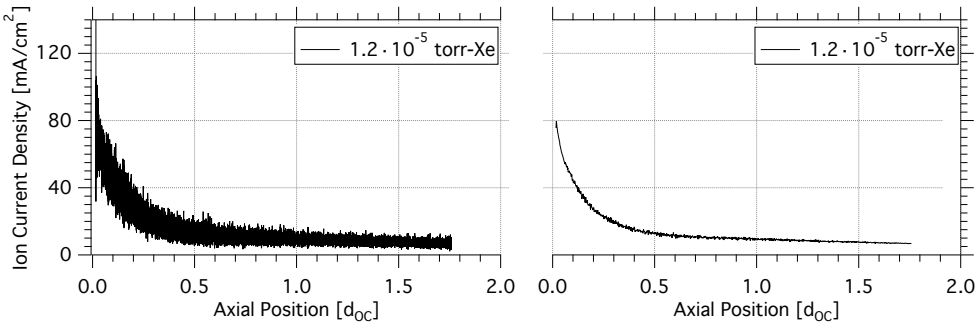

(b) 1.2·10^{-5} torr-Xe

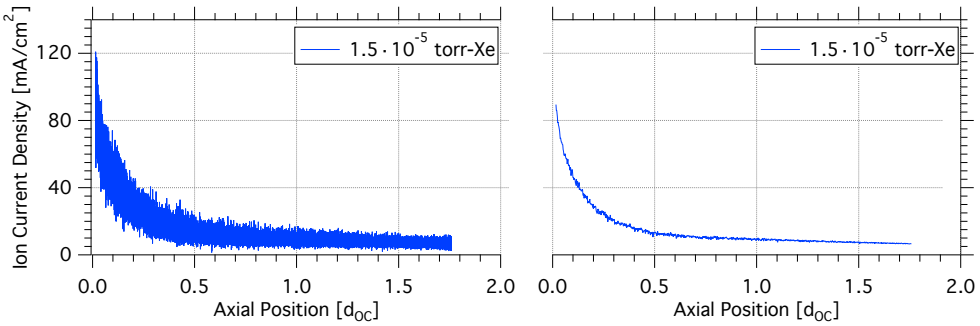

(c) 1.5·10^{-5} torr-Xe

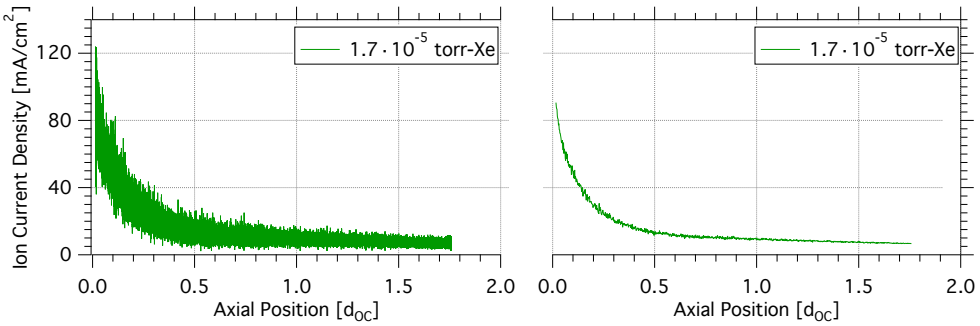

(d) 1.7·10^{-5} torr-Xe

Figure 6.12: **Axial current density measurements along outer-channel centerline at three background pressures before (left) and after (right) averaging to reduce oscillations**

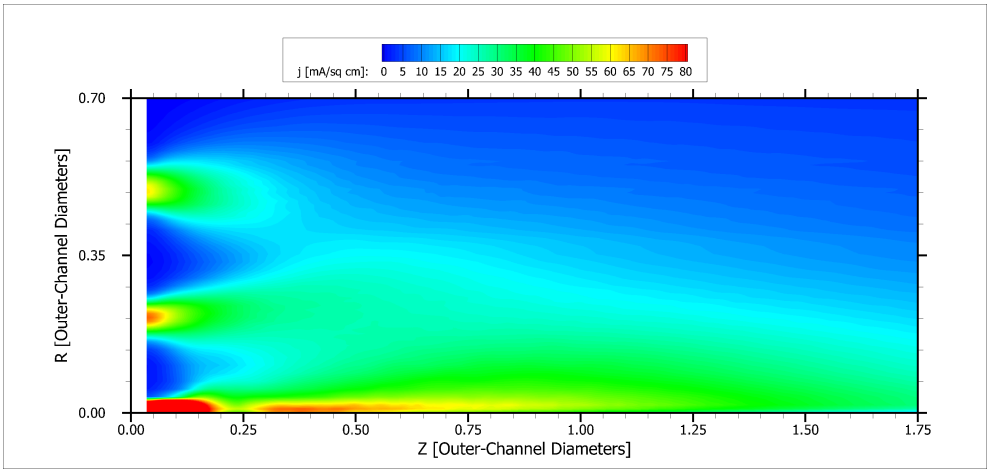

(a) $1.2{\cdot}10^{-5}$ torr-Xe

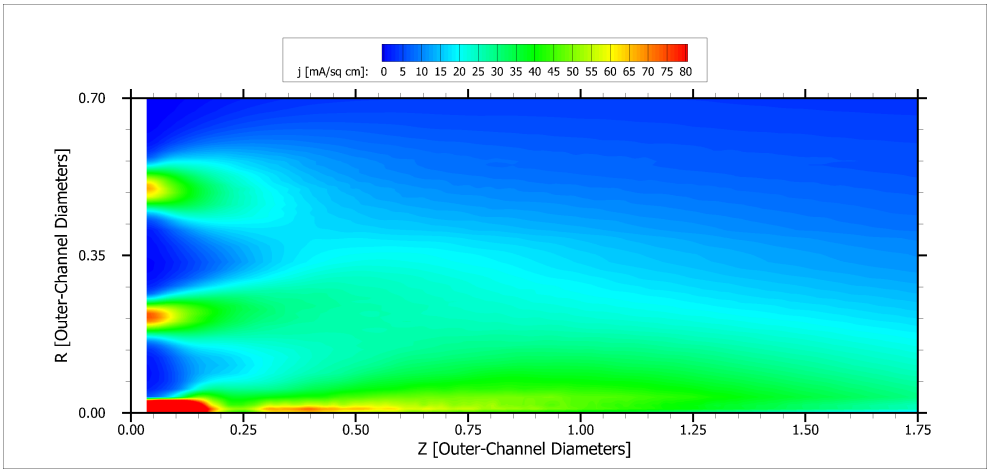

(b) $1.5{\cdot}10^{-5}$ torr-Xe

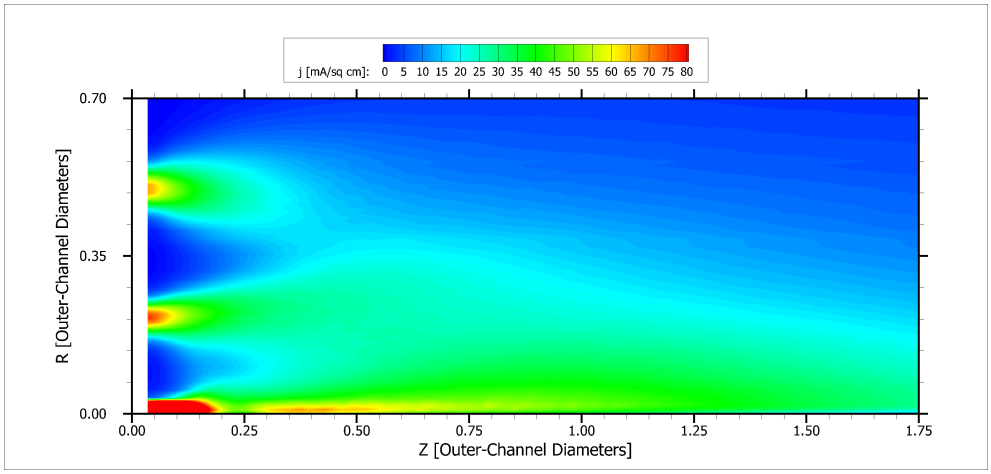

(c) $1.7{\cdot}10^{-5}$ torr-Xe

Figure 6.13: **Variation of dual-channel ion current density distribution with background pressure**

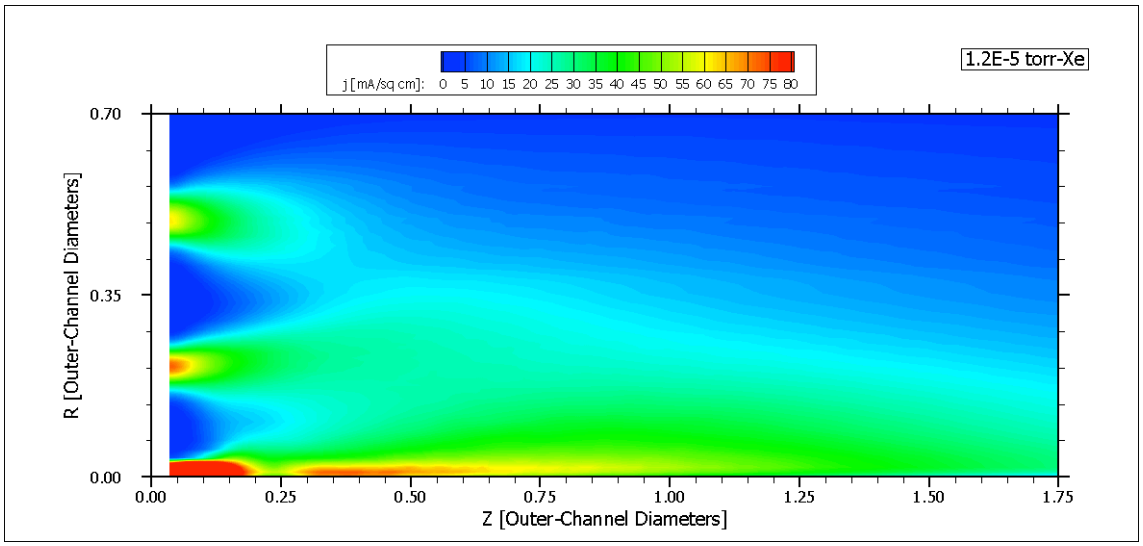

Figure 6.14: **Looped animation of near-field current density maps at $1.2{\cdot}10^{-5}$, $1.52{\cdot}10^{-5}$, and $1.72{\cdot}10^{-5}$ torr-Xe.** Click on figure in Adobe Reader to initiate animation.

p_c is the opposite of those observed with far-field Faraday probe measurements. This case of decreasing divergence with increasing background pressure may be a result of the acceleration zone receding into the discharge channel.

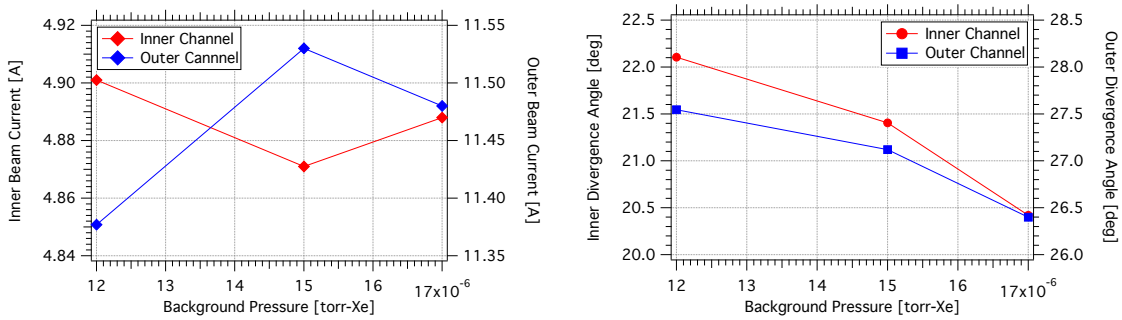

(a) Beam Current

(b) Divergence Angle

Figure 6.15: **Variation in integrated beam current and divergence angle with background pressure**

6.2.4 Results

The near-field measurement technique coupled with the very-near-field integration domain allow both the inner and outer beam currents to be determined in dual-

channel mode. Figure 6.16(a) and 6.16(b) show the comparisons of beam current in single-channel and dual-channel modes. For the majority of operating conditions, beam current increased proportionally with discharge voltage. However, the inner channel showed a slight decrease in I_b between 150 V and 200 V for both single-channel and dual-channel mode. The 200-V condition for the inner channel is unique due to the use of the internal trim magnet, which may be responsible for the abnormal trend in I_b with respect to discharge voltage.

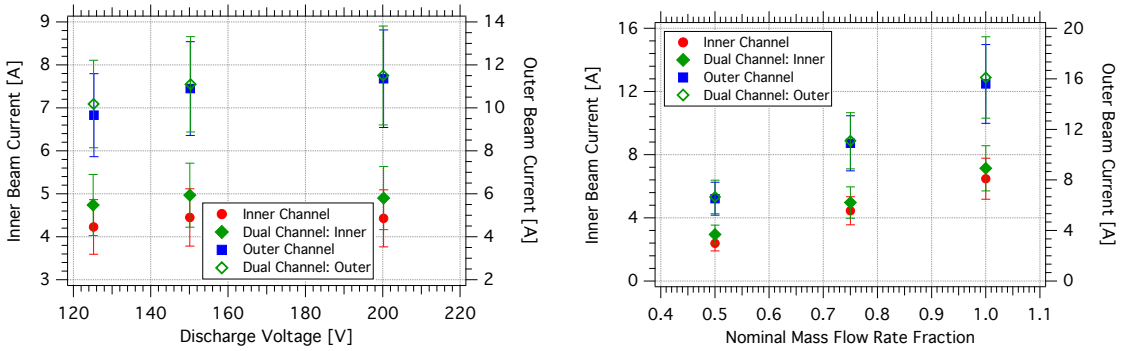

(a) Variation with Discharge Voltage

(b) Variation with Mass Flow Rate

Figure 6.16: **Variation in integrated beam current with discharge voltage and mass flow rate**

For all operating conditions, the dual-channel mode produces comparable or higher beam currents for both channels. However, the measurement uncertainty is considerable, primarily due to sheath expansion and pressure effects discussed in the previous section. The differences between the I_{b_k} in single-channel and dual-channel mode all fall within the measurement uncertainty. The increase is most pronounced for the inner channel in both absolute and relative magnitudes. For example, at 150 V, 7.0+17.4 mg/s, the inner beam current increased by 0.52 A (12%) while the outer beam current increased by 0.20 A (2%). ΔI_b maximizes absolutely at the highest mass flow rate combination and relatively at the lowest mass flow rate combination.

In all but one case, operating in dual-channel mode also reduces plume divergence. The calculated values for divergence angle, shown in Figures 6.17(a) and 6.17(b), The

exception is the inner-channel condition at 150 V, 4.7 mg/s where the mass flow rate was lowest. β did not exhibit great sensitivity to mass flow rate and only generally decreases with increasing discharge voltage for this data set. The exception was the inner channel in both modes from 125 V to 150 V.

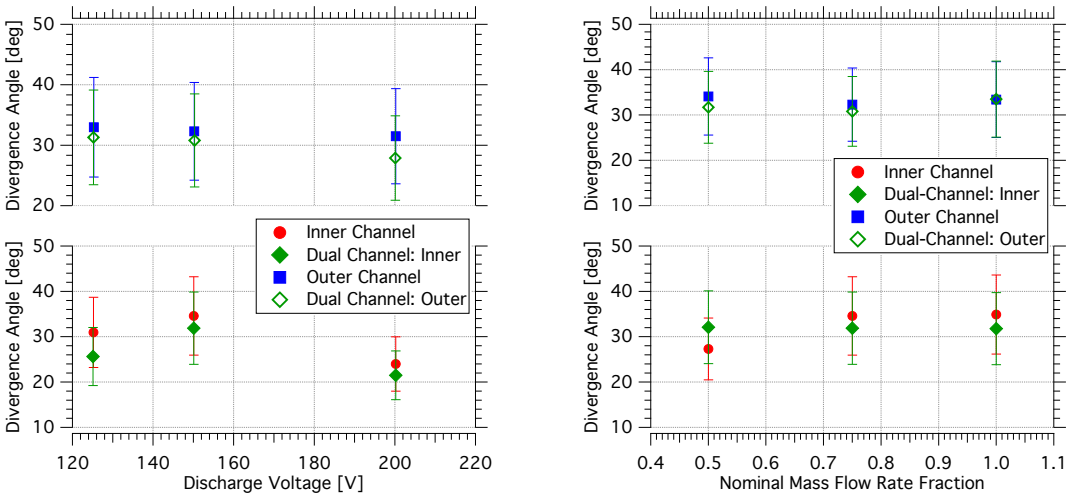

(a) Variation with Discharge Voltage

(b) Variation with Mass Flow Rate

Figure 6.17: **Variation in divergence half-angle with discharge voltage and mass flow rate**

6.3 Plasma Potential Measurements

Far-field measurements with the RPA and E×B probe indicated improved ion acceleration in the dual-channel mode, and the data suggest that a greater fraction of the discharge voltage is available for ion acceleration when firing both channels. Plasma potential measurements will confirm these measurements and will also provide a better understanding of the changes (or lack thereof) occurring in each discharge channel. Due to their short lifespan, the floating emissive probe technique yielded data on only one set of operating conditions. These are the dual channel condition at 200 V, 7.0+17.4 mg/s and the two corresponding single-channel conditions.

For simplicity, this section will show measurements taken along the centerlines of

each discharge channel. Measurements using the floating emissive probe and double probe typically began with the inner channel and then moved to the outer channel. The HARP injected the tip of each probe to 0.02 d_{OC} of the anode exit planes.

The raw measurements from the emissive probes along each channel centerline provide an indication of the axial variation of plasma potential within the accuracy of $1.5T_e(z)$ [71, 72]. Shown in Figures 6.18(a) and 6.18(b), the axial distributions of the probe potentials capture the 200-V discharge voltage applied between the anode and cathode along with rough locations of the acceleration zones. All potentials are relative to cathode instead of facility ground. From the raw measurements, the changes in cathode coupling voltages become apparent, and the advantage for the inner channel is especially pronounced. Within the accuracy of $1.5T_e(z)$, no changes in plasma potential appear to be significant upstream of the acceleration zone, suggesting that the interior plasma potential profiles remain relatively unaffected by dual-channel operation.

Comparison of the acceleration voltages from the emissive probe and RPA measurements can confirm the utility of these raw emissive probe measurements. For the 200-V dual-channel condition, the RPA measured acceleration voltages of 183±9 V and 181±9 V for the inner and outer channels, respectively. The raw emissive probe measurements show a 182-V and 184-V potential drop along the inner-channel and outer-channel centerlines, respectively. RPA measurements also indicated acceleration voltages of 176±9 V and 179±9 V for the 200-V inner-channel and outer-channel conditions, while the emissive probes show potential drops of 173 V and 179 V, respectively. Given the measurement uncertainties, the two measurement techniques agree very well and produce values of V_a within a consistency of 3 V.

The double probe provided measurements of electron temperature along both channel centerlines. Cold electrons make up most of the far-field plumes with temperatures around 1 eV. As expected, the electron temperatures increase as the probe

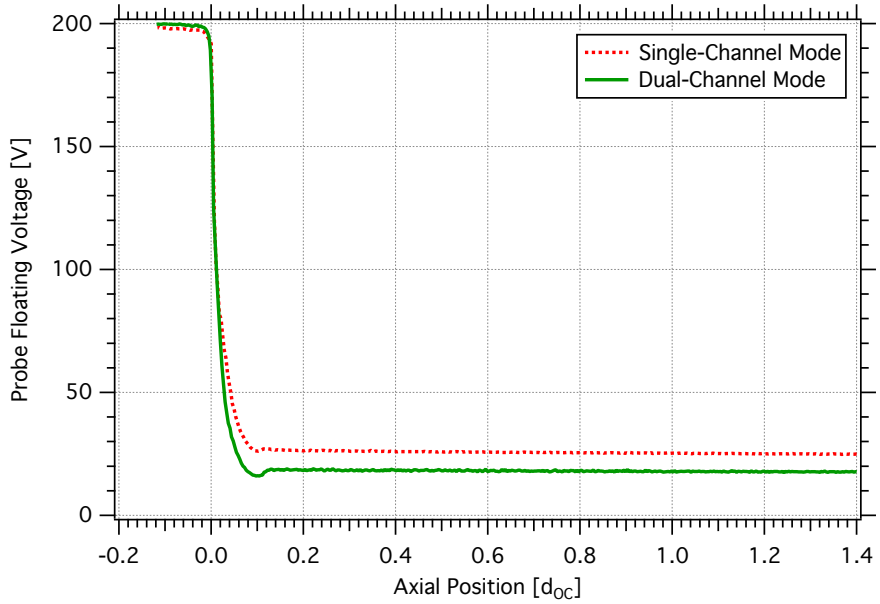

(a) Along Inner-Channel Centerline

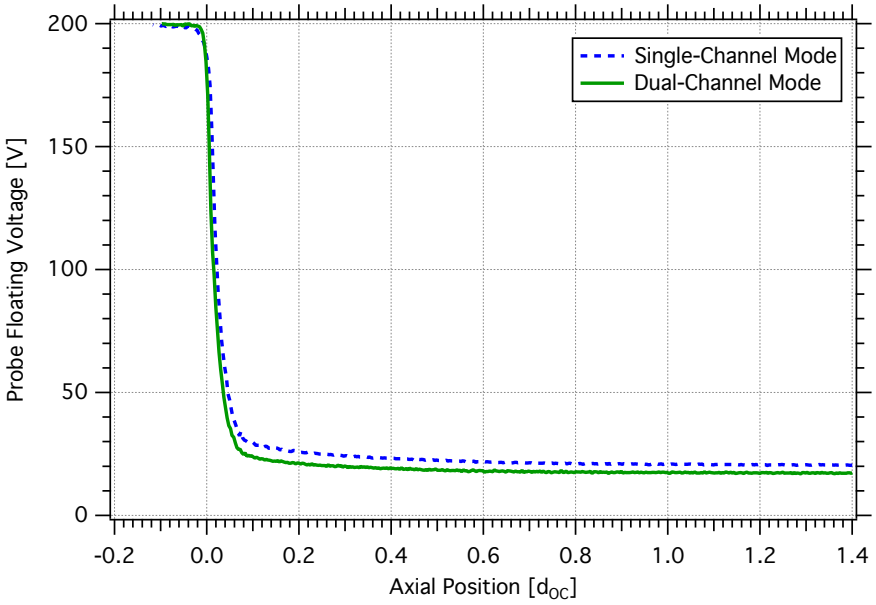

(b) Along Outer-Channel Centerline

Figure 6.18: **Raw measurement from emissive probes along inner-channel and outer-channel centerlines in single-channel and dual-channel modes. All potentials are relative to cathode potential.**

approached the Hall-current region near the exit plane. Unfortunately, saturation of the asymmetric double probe did not occur in the Hall current, so analysis of the I-V characteristics focused primarily on the near-field region up to the exit plane. The one exception was the outer channel centerline in dual-channel mode, where measurements were reliable only down to $0.04d_{OC}$.

The axial profiles of electron temperature, shown in Figures 6.19(a) and 6.19(b), show changes greater than 4 eV in both channels between the two operation modes of the X2. Neither set of profiles indicate that electron temperature globally increases or decreases due to the presence of another operating nested discharge channel. The far-field electron temperatures remain nearly the same between modes. Along the inner-channel centerline, T_e decreases upstream of $0.1d_{OC}$ and increases between $0.1d_{OC}$ and $0.15d_{OC}$ in dual-channel mode. The outer channel profiles of T_e show nearly the opposite relationships, with increases in T_e upstream of $0.1d_{OC}$ and decreases between $0.1d_{OC}$ and $0.6d_{OC}$.

Using the available and reliable measurements of electron temperature, the corrected plasma potential profiles show similar results external to the discharge channels as the raw emissive probe measurements. As shown in Figures 6.20(a) and 6.20(b), the external plasma potential decreases in dual-channel mode, which would correspond to decreases in cathode coupling voltage and increases in acceleration voltage. The raw measurements showed decreases in plasma potential along the inner- and outer-channel centerlines of 7.2 V and 3.2 V, respectively. The corrected measurements showed similar drops with 7.0-V and 4.1-V decreases along the inner- and outer-channel centerlines.

Correction for the local plasma potential eliminated the depression in probe floating potential along the inner channel near z=$0.1d_{OC}$. This location corresponds to a local increase in the electron temperature, as shown in Figure 6.19(a), located inside the separatrix surface of the magnetic field surrounding the inner channel. Figure

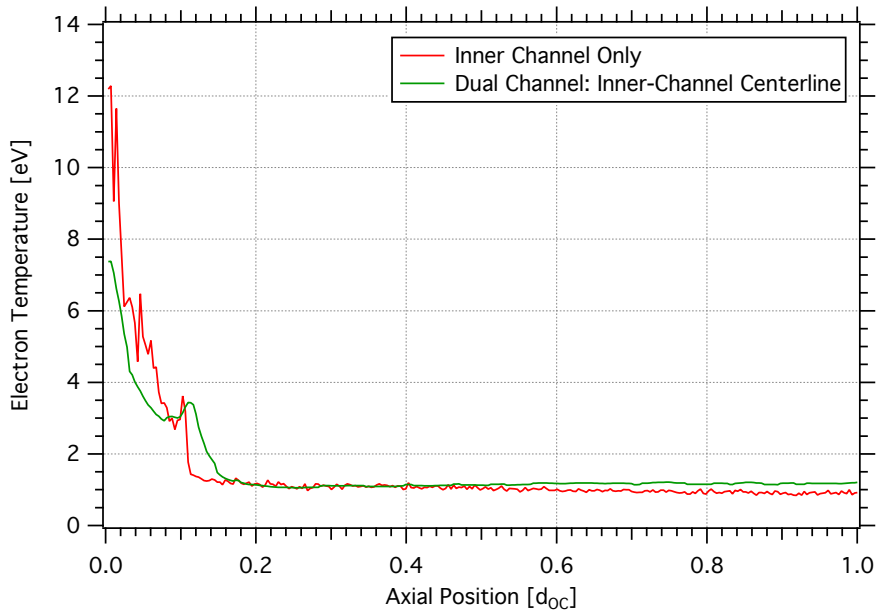

(a) Along Inner-Channel Centerline

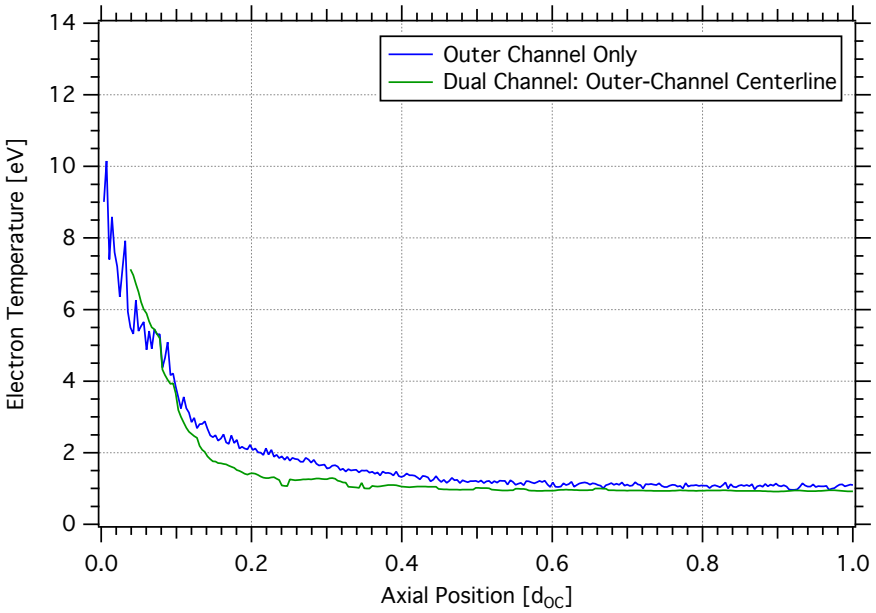

(b) Along Outer-Channel Centerline

Figure 6.19: **Axial distributions of electron temperatures along inner-channel and outer-channel centerlines in single-channel and dual-channel modes**

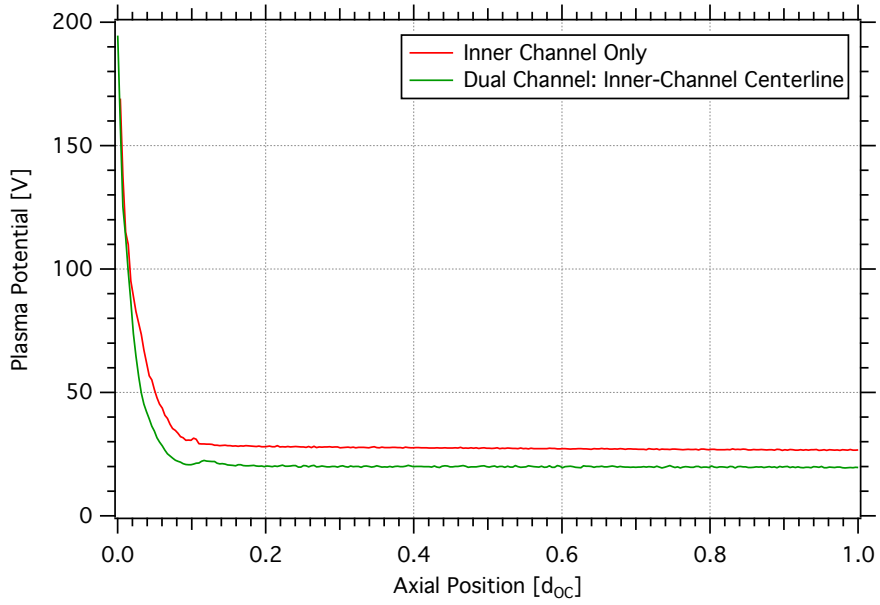

(a) Along Inner-Channel Centerline

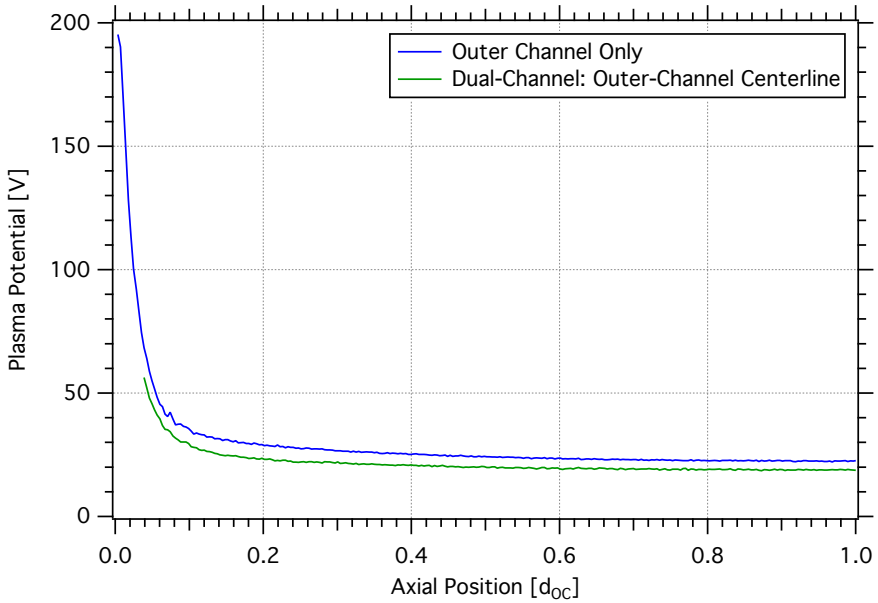

(b) Along Outer-Channel Centerline

Figure 6.20: **Axial distributions of plasma potential along inner-channel and outer-channel centerlines in single-channel and dual-channel modes**

6.21, generated from Infolytica MagNet, shows the near-field magnetic field topology with the intercept of the inner-channel centerline and separatrix surface indicated. The magnetic field at this location is 60 G, and the electron temperatures are up to 3 eV. The resulting electron Lamour radii, as calculated by Equation 6.4, are up to 0.7 mm, showing that electrons are magnetized in the separatrix surface. As magnetized electrons are more mobile along magnetic field lines, electrons emitted from the cathode have higher conductivity paths to the middle pole within the separatrix surface. These hot electrons from the cathode may be the cause of the abrupt change in T_e at $0.1d_{OC}$.

$$r_L = \frac{m_e v_{th}}{eB} = \frac{m_e}{eB}\sqrt{\frac{kT_e}{m_e}} \tag{6.4}$$

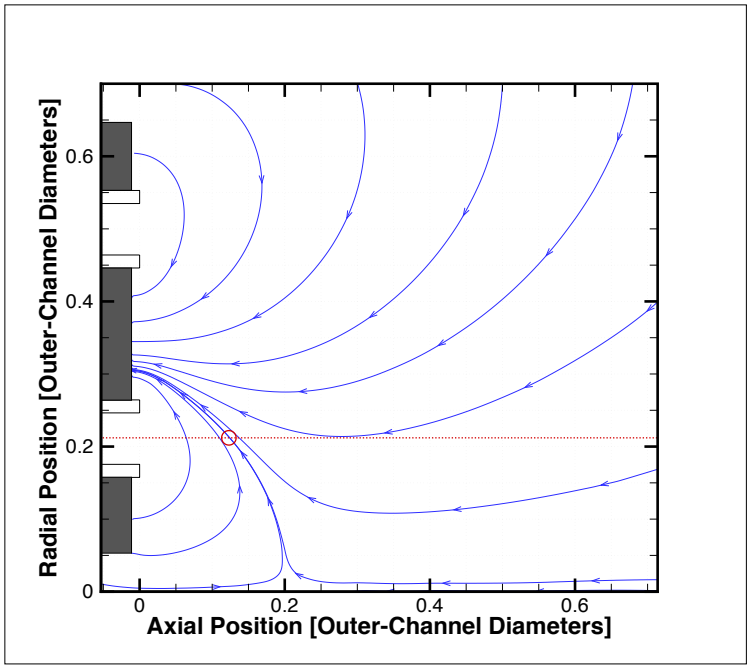

Figure 6.21: **Near-field magnetic field topology of the 200-V conditions with the intersection of the inner-channel centerline and separatrix surface indicated**

6.4 Summary

This chapter detailed the various plume measurements performed on the X2 and the variations in plume parameters between single-channel and dual-channel mode. Far-field measurements indicated that dual-channel operation results in improved acceleration voltages and increases in multiply-charged ion species. Internal measurements showed that the variation of plasma potential occurred primarily downstream of the acceleration zone and confirmed that the changes in acceleration voltages came primarily from improvements in cathode coupling. Near-field measurements permitted the measurement of individual beam currents and showed increased ion beam currents in dual-channel mode. Chapter VII will utilize these plume measurements to further examine the influences of dual-channel operation on efficiency and performance.

CHAPTER VII

Influence of Dual-Channel Operation on Efficiency and Performance

The previous two chapters showed the performance capabilities and plume characteristics of the X2 in both single-channel and dual-channel modes. When firing both channels simultaneously, measurements on the thrust stand indicated increased thrust beyond the superposition of the individually-measured thrust, and the various diagnostics showed corresponding increases in beam current, acceleration voltage, and, in most cases, plume collimation.

The results from the last two chapters include all the required parameters to calculate the various utilization efficiencies, as discussed in Section 7.1. Section 7.2 assesses the utility of the NHT performance model from Section 2.5 and shows the estimation of each discharge channel's thrust from plume measurements.

7.1 Utilization Efficiencies

As derived in the latter part of Section 2.5, the model of NHT performance decomposes anode efficiency into the charge, voltage, axial mass, and axial current utilization efficiencies. Axial mass and axial current utilization efficiencies effectively absorbed the divergence efficiency because of the individually-determined beam cur-

rents and divergence angles. Each utilization efficiency describes a certain aspect of the thruster's operation by quantifying how power or mass flow directly contributes to useful thrust. For the comparisons between single-channel and dual-channel operation, relative changes in these utilization efficiencies are the most relevant.

After converting current fractions Ω_i into charge utilization efficiencies η_q, the increase in multiply-charged species plays only a small role in the change in thruster efficiency between single-channel and dual-channel operation. As expected for discharge voltage between 100 V and 200 V, η_q remains in a narrow band above 98% for all operating conditions. The uncertainty in η_q encompasses the differences in η_q between operating modes, but in general, dual-channel conditions possess lower charge utilization efficiency. The only exception lies with the 100 V operating condition, where the outer-channel condition produced the most doubly-charged species.

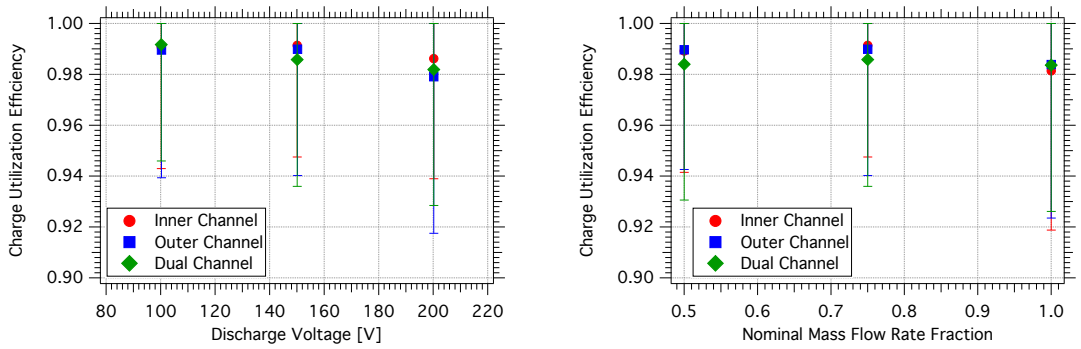

(a) Variation with Discharge Voltage

(b) Variation with Mass Flow Rate

Figure 7.1: **Single-channel and dual-channel charge utilization efficiencies**

As observed in the RPA measurements, the dual-channel modes exhibit the higher voltage utilization efficiencies. With the exception of the 100-V condition, the greatest increase in η_v occurs between the inner-channel conditions and the dual-channel conditions. Despite its proximity to the internally-mounted cathode, the inner channel by itself requires a greater percentage of the discharge voltage to extract electrons.

Measurements of cathode coupling voltages V_c, as determined by Equation 7.1, confirm the observations made in voltage utilization. Data for V_c came from mea-

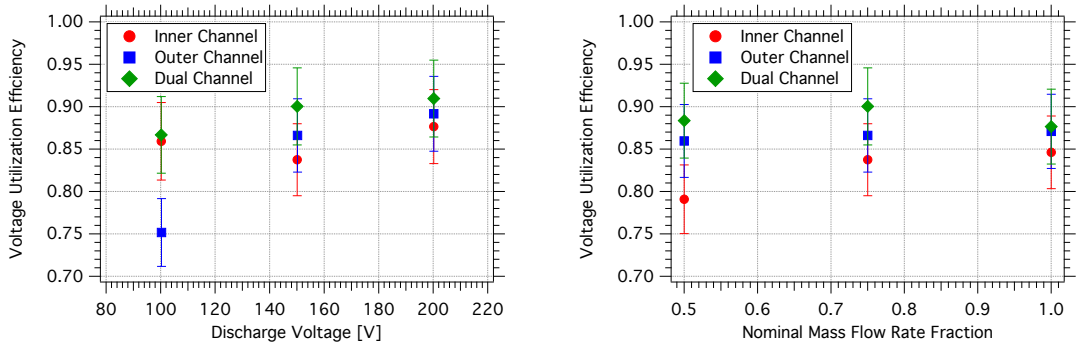

(a) Variation with Discharge Voltage (b) Variation with Mass Flow Rate

Figure 7.2: **Single-channel and dual-channel voltage utilization efficiencies**

surements of the cathode-to-ground voltage V_{cg} and the downstream plasma potential V_p, as shown in Equation 7.1. As shown in Figures 7.3(a) and 7.3(b), the cathode coupling voltage decreases in all cases after a transition from single-channel and dual-channel mode. The inner channel benefits the most from the decrease in cathode coupling voltage.

$$V_c = V_p - V_{cg} \tag{7.1}$$

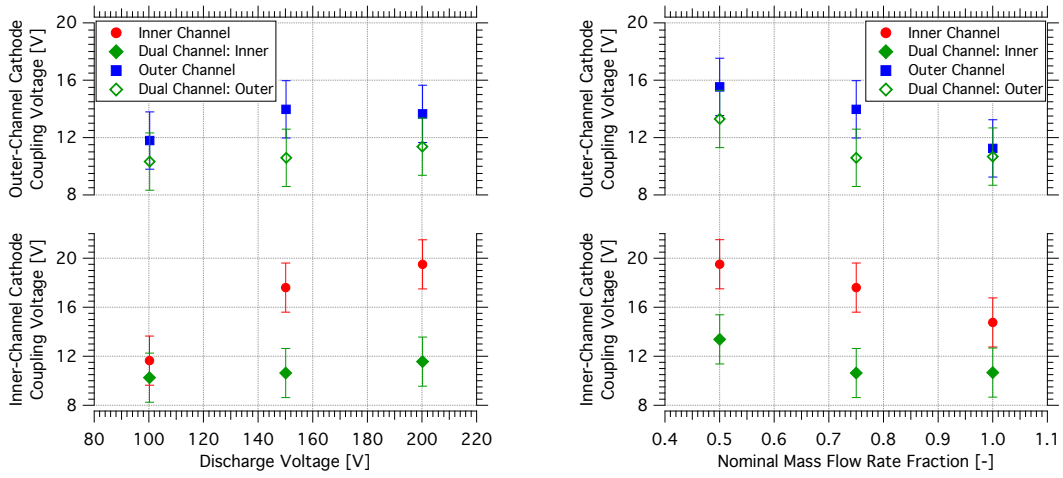

(a) Variation with Discharge Voltage (b) Variation with Mass Flow Rate

Figure 7.3: **Single-channel and dual-channel cathode coupling voltages**

From the near-field measurements, axial beam currents repeatedly rose in the dual-channel mode and resulted in higher axial current utilization efficiencies. In

the case of η_{b_A}, the greatest increase occurs between the outer-channel and the dual-channel conditions. Of the single-channel conditions, the inner channel possessed the better current utilization efficiency over all operating conditions. Note that the dual-channel conditions utilize the combined axial beam current and the combined discharge current. A look at the variations in the individual quantities will be given in Section 7.2.

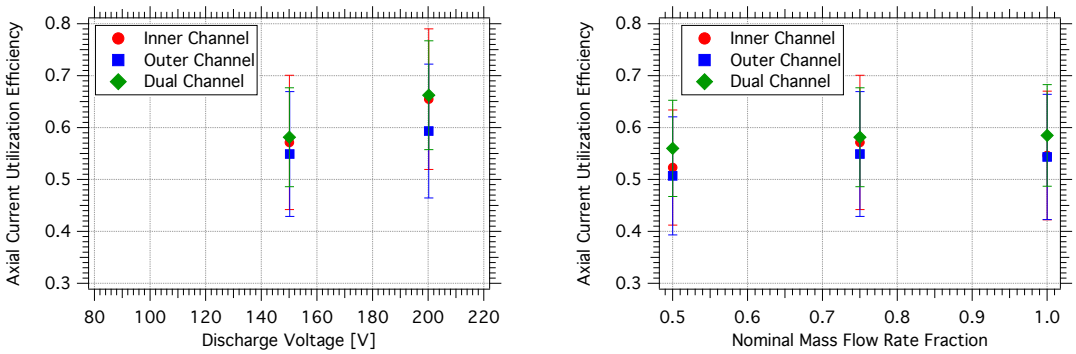

(a) Variation with Discharge Voltage

(b) Variation with Mass Flow Rate

Figure 7.4: **Single-channel and dual-channel axial current utilization efficiencies**

Determined from measurements of beam current, divergence angle, and average charge, the axial mass utilization efficiencies also rose or remained the same between single-channel and dual-channel modes. However, the differences are quite small, especially in comparison to the uncertainties. The magnitude of the uncertainty in η_{m_A} is large due to the propagated uncertainties from I_A, Q, and $\dot{m}_a$.

7.2 Comparison of Dual-Channel to Single-Channel Operation

All the parameters from plume measurements can now yield the thrust, as expressed in the performance model by Equation 2.32. Comparisons with the measured thrust from all operating modes will show the accuracy of the model and its utility in examining the dual-channel thrust.

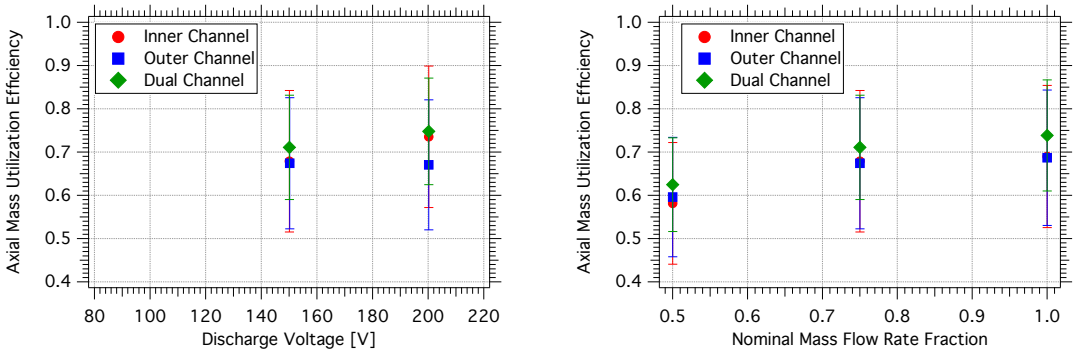

(a) Variation with Discharge Voltage

(b) Variation with Mass Flow Rate

Figure 7.5: **Single-channel and dual-channel axial mass utilization efficiencies**

The following comparisons of measured thrust in this section will not involve measurements at constant background pressure across all operating points. Constant-pressure data from Section 5.1 show that the elevated background pressure did not sufficiently account for the performance increases seen in dual-channel mode anyway. Additionally, the plume measurements did not occur under constant background pressure, because the required amount of xenon would have been prohibitive. For more appropriate and direct comparisons, thrust measurements will be paired with the results of plume measurements at the corresponding pressure without any auxiliary flow.

As shown in Figures 7.6(a) and 7.6(b), the efficiency model tends to underpredict thrust, although the differences fall within the uncertainties of the calculated thrust. Uncertainties in the measured thrust data are within the size of the markers in these figures. The error varies from 11% to 21% of the calculated thrust, although the uncertainties range from 17% to 23% of the same quantities. Despite these shortcomings, examination of the calculated thrusts show that the performance model reflects the relationships observed in the actual thrust measurements. In a relative sense, the models for T can provide the insight required to explain the differences between the operating modes of the X2.

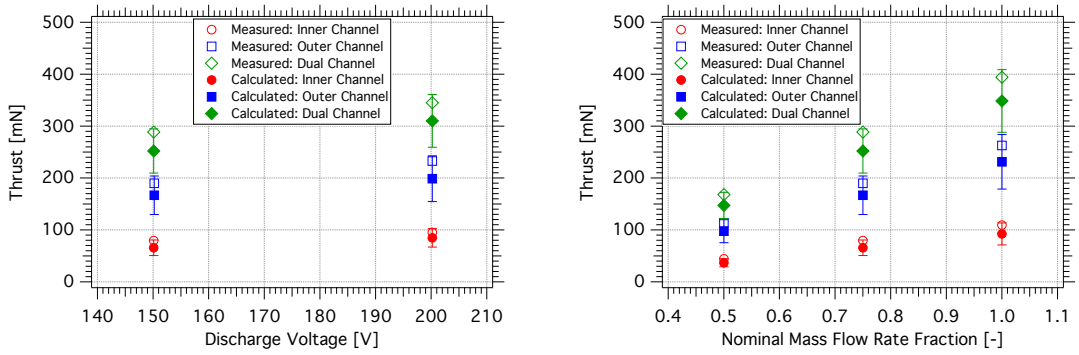

(a) Variation with Discharge Voltage

(b) Variation with Mass Flow Rate

Figure 7.6: **Comparisons of measured thrust to calculated thrust from plume measurements**

Comparisons of the total thrust ratios Υ_t, as defined in Equation 7.2, serve as a logical alternative to the examination of the absolute thrust values. Υ_t is defined as the ratio of the dual-channel thrust T_{1+2} and the sum of the single-channel thrusts T_1 and T_2. The individual thrust from a channel in dual-channel mode is T'. In this nomenclature, the subscript 1 indicates the inner channel while 2 indicates the outer channel.

$$\Upsilon_t = \frac{T_{1+2}}{T_1 + T_2} = \frac{T_1' + T_2'}{T_1 + T_2} \tag{7.2}$$

Figures 7.7(a) and 7.7(b) show the measured and calculated values for Υ_t for all modes of the X2. The calculated thrust ratios fall within 0.04 of the measured thrust ratios, and this good agreement required inclusion of all quantities measured in the plume. In other words, the change in just one measured plume parameter (e.g. acceleration voltage) does not sufficiently account for all the additional thrust provided by the dual-channel mode. Consideration for all plume parameters (V_a, I_b, β, Ω_i) is required.

The performance model can provide an estimation of the individual thrusts from each channel during dual-channel mode. Such a measurement is not possible with the inverted-pendulum thrust stand for a fully-integrated NHT such as the X2, but use

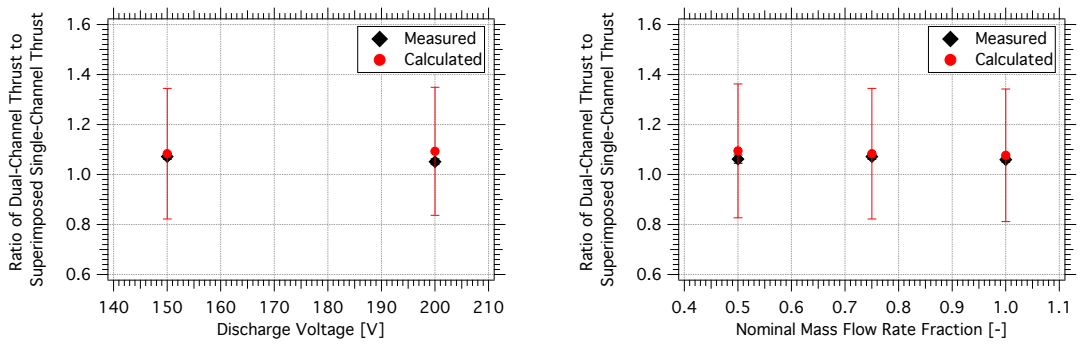

(a) Variation with Discharge Voltage

(b) Variation with Mass Flow Rate

Figure 7.7: **Ratios of single-channel to dual-channel thrust**

of all the plume measurements can yield T_1' and and T_2'. Following the example of Υ_t, the individual thrust ratios Υ are employed to quantify the thrust change for each channel using the measured acceleration voltage, beam current, divergence half-angle, average charge, and charge utilization efficiency.

Υ effectively utilizes the model for thrust from a single-channel HET while decomposing the ratio of thrusts into ratios of individual plume parameters. In keeping with the established utilization efficiency names, these ratios are the voltage factor τ_v, the current factor τ_b, the divergence factor τ_d, and the charge factor τ_q. They will be collectively referred to as plume factors. Each plume factor will show the effect of each plume parameter on the individual thrust ratios. For example, τ_v quantifies the contribution from the change in acceleration voltage on the change in thrust between single-channel to dual-channel mode.

$$\Upsilon = \frac{T_k'}{T_k} = \sqrt{\frac{V_{a_k}'}{V_{a_k}}}\frac{I_{b_k}'}{I_{b_k}}\frac{\cos\beta_k'}{\cos\beta_k}\sqrt{\frac{\eta_q'/Q'}{\eta_{q_k}/Q_k}} = \tau_v\tau_b\tau_d\tau_q \tag{7.3}$$

$$\tau_v = \sqrt{\frac{V_{a_k}'}{V_a}} \tag{7.4}$$

$$\tau_b = \frac{I_{b_k}'}{I_{b_k}} \tag{7.5}$$

$$\tau_d = \frac{\cos\beta'_k}{\cos\beta_k} \tag{7.6}$$

$$\tau_q = \sqrt{\frac{\eta'_q/Q'}{\eta_{q_k}/Q_k}} \tag{7.7}$$

The individual thrust ratios, shown in Figures 7.8(a) and 7.8(b), show that the inner channel repeatedly receives the greatest relative increase in thrust from dual-channel firings. In absolute differences, the calculated thrust for the inner channel increases by 8 mN to 14 mN while the outer channel increases by 4 mN to 10 mN. Note that individual thrust values come from plume measurements in both single-channel and dual-channel modes in order to maintain consistency in comparisons. Although advantageous for both discharge channels, simultaneous firing provides a thrust increase that is biased toward the inner channel.

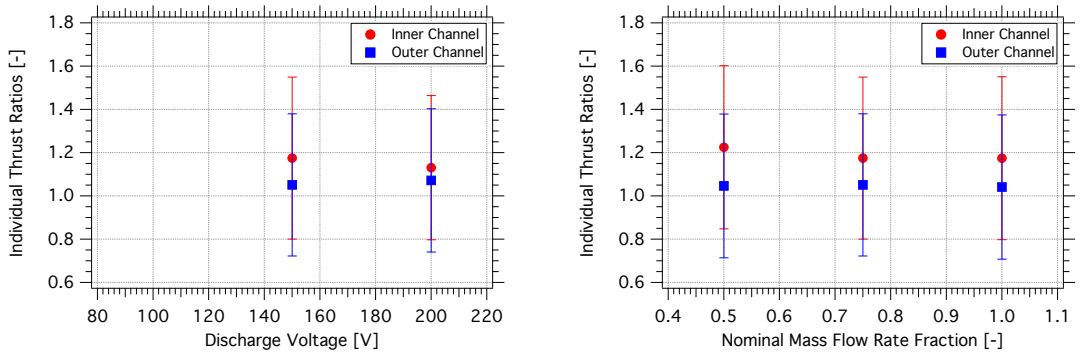

(a) Variation with Discharge Voltage

(b) Variation with Mass Flow Rate

Figure 7.8: **Individual thrust ratios from the calculated inner-channel and outer-channel thrusts**

Of all the plume factors, the current factors are the greatest above unity, indicating that increased beam currents are the primary cause behind the increased thrust in dual-channel mode. As shown in Figures 7.9(a) and 7.9(b), τ_b are consistently higher for the inner channel than the outer channel. In most cases, τ_b is nearly unity for the outer channel, but for the inner channel, the current factor is nearly 1.1 with the exception of the 50% nominal mass flow rate condition with a τ_b of 1.23.

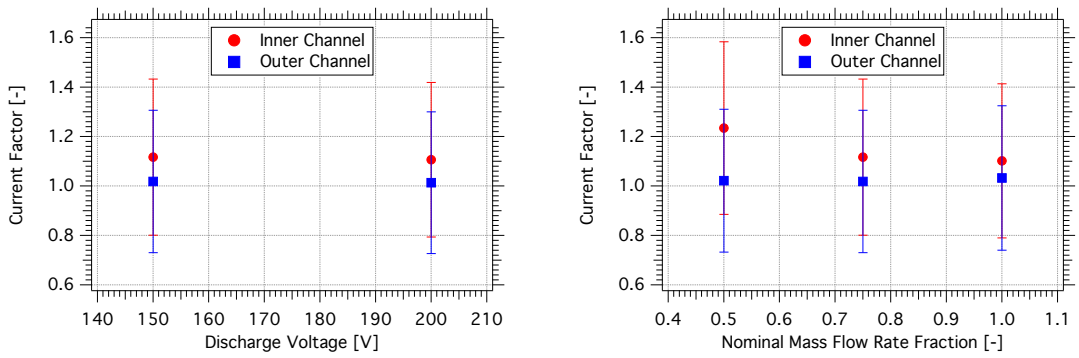

(a) Variation with Discharge Voltage

(b) Variation with Mass Flow Rate

Figure 7.9: **Current factors for dual-channel conditions**

Measurements of facility effects in Sections 5.1 and 6.2 show that entrainment of background neutrals is an unlikely cause of the increased beam currents. A more probable cause is inter-channel neutral ingestion due to the proximity of the two discharge channels to each other and the dominant influence of the discharge channels on near-field neutral density. This form of ingestion could also explain the greater increase in inner-channel beam current compared to the outer-channel beam current. With its higher mass flow rate, the outer channel naturally sources more neutrals to the inner channel than vice-versa. However, future studies are necessary to further investigate this phenomenon and to conclusively determine the cause of the increased beam currents.

To a lesser extent, improvements in voltage utilization also contribute to the increases in thrust. The voltage factors, plotted in Figures 7.10(a) and 7.10(b), show that the increased voltage utilization detected by the RPA does augment thrust but not to the same extent as the increased beam current. Inner-channel values for τ_b range from 1.10 to 1.23 while τ_v vary from 1.02 to 1.06. Υ for the inner-channel vary from 1.13 to 1.23, indicating that the improved acceleration voltages alone cannot sufficiently account for the performance enhancements. Similar to τ_b, τ_v for the outer channel stays much closer to unity, showing little relative benefit to the outer channel.

Changes in divergence and charge species have the smallest influence on the

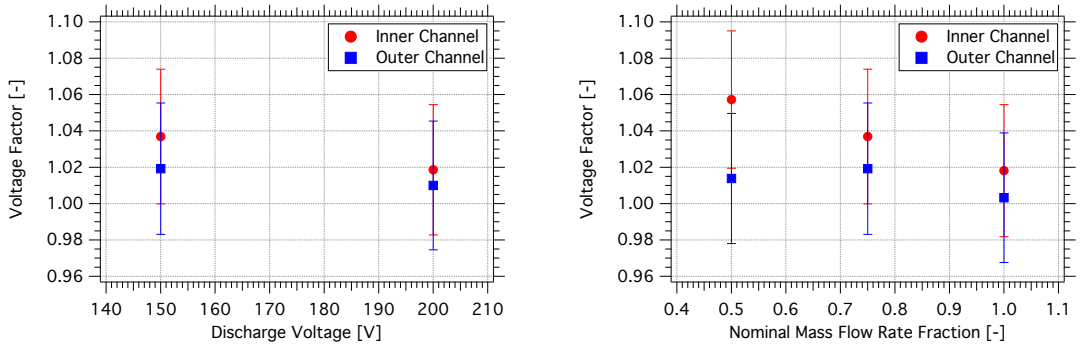

(a) Variation with Discharge Voltage (b) Variation with Mass Flow Rate

Figure 7.10: **Voltage factors for dual-channel conditions**

changes in thrust and, in several cases, result in plume factors less than unity. Both τ_d and τ_q remain close to unity for both channels, varying between 0.95-1.04 and 0.98-1.01, respectively. Improved plume divergence augments the thrust in all cases except for the inner channel at the lowest mass flow rate. The small fraction of multiply-charged species have a very small effect on the thrust changes and are nearly negligible for the conditions considered in this study.

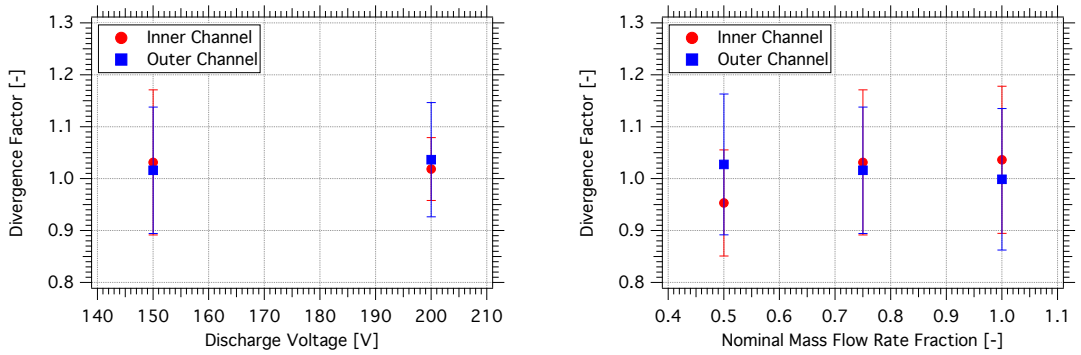

(a) Variation with Discharge Voltage (b) Variation with Mass Flow Rate

Figure 7.11: **Divergence factors for dual-channel conditions**

The combination of all plume factors show the sources behind the thrust augmentation during dual-channel operation of the X2. Increased beam currents possess the greatest influence and benefit the inner channel most in a relative sense. For future designs with more than one nested channel, this form of enhancement could apply for all interior channels, but this effect requires duplication and verification. Increased

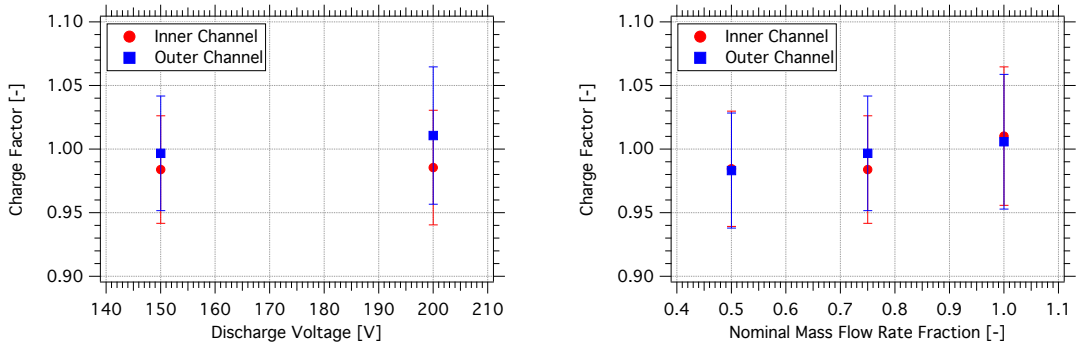

(a) Variation with Discharge Voltage

(b) Variation with Mass Flow Rate

Figure 7.12: **Charge factors for dual-channel conditions**

voltage utilization by decreased cathode coupling has the second greatest influence on the thrust change. Improved divergence may also occur but was not universal in the case of these conditions with the X2. Lastly, at low discharge voltages, the changes in the distribution of charge species had a very small effect.

7.3 Summary

This chapter discussed the changes in utilization efficiencies between single-channel and dual-channel mode. Variations in charge utilization efficiencies remained small for all operation conditions, while voltage, axial current, and axial mass utilization efficiencies showed general improvement from dual-channel operation. The efficiency model outlined in Chapter II, with additional modifications, showed that the inner channel experienced the greatest relative increase in thrust. The augmented performance primarily resulted from increase current utilization and voltage utilization, with smaller influences from changes in divergence and fractions of multiply-charged species.

CHAPTER VIII

Conclusions

8.1 Introduction

The nested Hall-effect thruster proved to be an effective electric propulsion concept through measurements of performance and discharge characteristics. This study included performance measurements with each channel of the NHT firing individually (single-channel mode) and both channels of a NHT firing simultaneously (dual-channel mode). At low discharge voltages, this nested configuration displayed improved performance over the superimposed performance of the individual channels.

The NHT in this work began as a joint research project between the University of Michigan and the Air Force Research Laboratory and eventually took shape as the X2. As a demonstrator of the NHT concept, the X2 had two concentric discharge channels with a shared internal LaB_6 hollow cathode provided by the Jet Propulsion Laboratory and the Air Force Research Laboratory. Each discharge channel had similar cross-sectional dimensions and anode designs.

8.2 Summary of Findings

Measurements of performance on the X2 demonstrated that a two-channel NHT can operate efficiently with only one or both discharge channels firing. Dual-channel

measurements of the X2 in this work were primarily at low discharge voltages up to 300 V where dual-channel operation proved most efficient for this particular thruster. Although the outer channel did not perform as well as the inner channel, the shortcomings of the X2's outer channel are specific to this NHT and can be avoided in future NHT designs. The X2 demonstrated a constant-power throttling method at 5 kW and 6 kW and showed that an additional channel can expand the mass flow rate capabilities of a HET.

Thrust measurements at constant background pressure showed small degrees of thrust augmentation in the dual-channel mode. Performing these measurements at constant background pressure eliminated the ingestion of background neutrals as a major contributor to the performance increase. Comparisons showed 4% to 9% increases in thrust between dual-channel conditions and the combination of corresponding single-channel conditions with the same magnetic field and cathode flow fraction. Of the two channels, the inner channel repeatedly benefited more from simultaneous firings.

The plume measurements provided further insight into the thrust increase in dual-channel mode and found that the augmentation originated from several factors. In dual-channel mode, both channels saw increases in beam current and acceleration voltage, but the higher beam currents were predominantly responsible for the improvements in thrust. A likely cause of the higher beam currents is inter-channel neutral ingestion, but identification of the source of beam current augmentation will require additional study. The increased acceleration voltages resulted in smaller contributions to the improved performance and manifested as reduced cathode coupling voltages. Corresponding to the thrust measurements, the inner channel tended to have greater increases in beam current and acceleration voltage for the conditions considered in this study.

8.3 Recommendations for Future Work

The experiments and results of this work were the first on a thruster that served as a technology demonstrator and testbed. NHT technology shows promise for expanding Hall-effect thruster capabilities, and additional work on the X2, more evolved NHTs, and traditional HETs are necessary for further advances. As the HET is the building block of the NHT, the majority of HET research will be useful and applicable to their nested derivatives. Improving HETs is necessary for evolving NHTs, and there exist many recommendations for further work in single-channel Hall-effect thrusters. However, the following are recommendations specific to nested Hall-effect thrusters.

8.3.1 NHT Geometries and Configurations

A nested Hall-effect thruster can include many different configurations and geometries that differ from the X2, and further exploration of the design space may lead to improved capabilities, especially considering the number of design philosophies that exist between propulsion organizations. Additional measurements on other NHTs are also necessary to determine if the observations on the X2 are universal to NHTs or design-specific.

Determination of the effect of different channel geometries requires the development of additional NHTs and many additional experiments. Such NHTs could feature the nesting of three or more discharge channels and the use of variable discharge channel geometries. Changes in the inter-channel spacing and different magnetic circuit design would also be worthwhile to explore.

The X2 is a NHT of fixed configuration where both discharge channels are integrated into a single structure. However, other alternative configurations may be suitable based on design philosophies, development timelines, or application. One alternative is the modular NHT where each channel is an individual thruster and

maybe be separated for modification or isolated study. Similarly, an existing HET can be retrofitted with an additional nested discharge channel, as Busek [46] showed, or an entirely different thruster type, such as the HET-ion engine hybrid suggested by Patterson [88, 89]. The modular configuration would make possible the measurement of the individual thrust of each channel in NHT multi-channel modes. For such a measurement, the individual channels must be free from contact from each other. The channels would require separate thrust stands or separate pumpdowns where only one channel is mounted to the thrust stand at a time while the others remain static.

Different propellants can provide larger variations in specific impulse between discharge channels than demonstrated with the X2. For example, a two-channel NHT can flow krypton through a high-voltage inner channel while the outer channel remained on xenon for higher thrust-to-power ratio. In the most simple case, the propellant flow system may only provide one type of propellant to each channel.

8.3.2 Effects of Cathode Flow Fraction and Inactive Channel Flow on Near-Field Pressure

Increased near-field pressure and inter-channel neutral ingestion are plausible causes of the increased performance in dual-channel mode for the X2, but the sources of additional neutrals were not isolated. The two most influential sources would be the increased cathode flow in dual-channel mode along with the propellant injected by the adjacent discharge channel. The operating conditions used in this NHT study held the cathode flow fraction constant between operating modes, so the influence of CFF on dual-channel performance remained unquantified. A study on the sensitivity of dual-channel (or multi-channel operation) under varying cathode flow fractions is worth considering, as an internally mounted cathode can influence in the near-field pressure in front of interior channels. One simple method would be to hold cathode

flow rate constant and investigate if thrust remains augmented in dual-channel (or multi-channel) mode.

Single-channel conditions can also undergo testing with propellant injected through the inactive channel(s). In this simple method, the active channels can ingest neutrals from the inactive channels in an effort to simulate the conditions present in multi-channel modes. For example, one can revisit the 150 V, 7.0+17.4 mg/s operating condition on the X2 by firing only the inner channel at 7.0 mg/s and supplying additional propellant through the inactive outer channel. However, applying the full 17.4 mg/s would likely introduce too many neutrals for the inner channel to ingest, because most of the propellant applied to the outer channel becomes ionized and accelerated. A more appropriate mass flow rate would be the unionized neutral mass flow rate for the outer channel in dual-channel mode. This $\dot{m}_2$ would be equal to the product of (1-$\eta'_{m,2}$) and 17.4 mg/s, which is 3.3 mg/s.

8.3.3 Channel Interactions and Time-Resolved Discharge Properties

Continued study on the interactions between discharge channels would be useful for future development of NHTs. Measurements on the X2 [90] indicated increased discharge current oscillations and varying cross-talk based on operation condition, and experiments conducted by Lobbia and Sekerak [91] along with McDonald and Sekerak [92,93] provided additional measurements on time-varying discharge properties, plume characteristics and azimuthal nonuniformities (spokes). Naturally, the problem of channel interactions is multidimensional, as the degree of interactions may vary with mass flow rate, discharge voltage, channel separation, number of active cathodes, chamber pressure, and other factors.

8.3.4 Near-Field Current Density Measurements

Current density measurements on the X2 provided reference cases where dual-channel operation resulted in improved ion beam current. Similar measurements on other NHTs are necessary to confirm the commonality of this phenomenon. Maintaining constant background pressure by auxiliary propellant flow or varying the number of active pumps are methods of bypassing the influences of facility neutrals when making relative comparisons between modes. Measurements in single-channel mode may also feature propellant flowing through inactive channels in order to simulate the neutral flow conditions in multi-channel mode. Varying the inactive channel mass flow rate can provide a means of determining the sensitivity of the single-channel beam current to inter-channel neutral ingestion.

Future studies of NHT near-field current density may also consider the influence of the stronger discharge current oscillations on the multi-channel beam current. Extending Lobbia's method [94] to the near-field Faraday probe would provide time-resolved measurements on the dynamic variations in ion current density. Additional measurements should also quantify the variations of the near-field oscillations with background pressure, as the in-orbit oscillations of a HET can vary significantly from the dynamic behavior in vacuum chambers.

APPENDICES

APPENDIX A

Operation of the X2 on a Shared Power Supply

As discussed in Chapter III, separate power supplies powered the two discharge channels of the X2. To determine if any crosstalk was due to the communication between discharge power supplies, the X2 was fired in dual-channel mode off the same discharge power supply. Additionally, this short test verified that both channels could operate off the same power supply without affecting the operation of the NHT.

A single operating condition was chosen for this test. The discharge voltage applied to both channels was 150 V, and the mass flow rate combination was 9.3 mg/s through the inner channel and 23.3 mg/s through the outer channel. The cathode flow fraction was 10%, and the magnet settings were held constant.

The results, as shown in Figure A.1(a) and A.1(b) and Table A.1, show negligible changes between operation with separate and shared power supplies. The discharge currents, measured by the NT-series current sensors, changed by only 1.2% for the inner channel and 0.5% for the outer channel. Breathing mode frequencies shifted by less than 1 kHz, and performance was nearly identical between power supply configurations. In Figure A.1(a) and A.1(b) an extra oscillation frequency corresponding to the outer channel's breathing mode appears on both power spectra of the inner-channel discharge current. This form of crosstalk, which was also observed during 6-kW operation [90], is independent of the two power supply configurations.

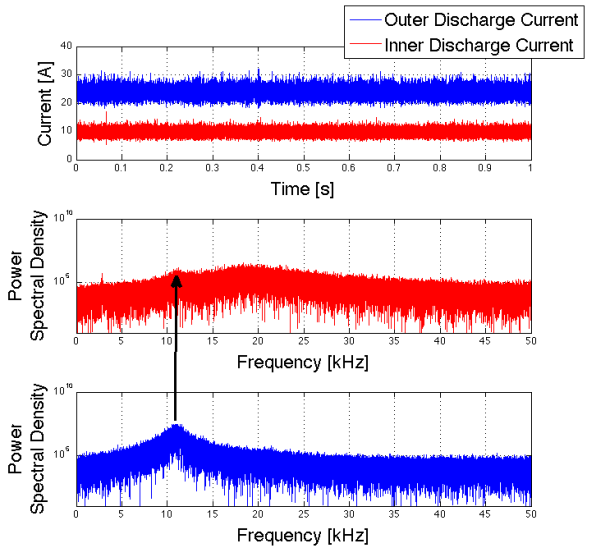

(a) Discharge current measurements for dual-channel operation with separate discharge power supplies

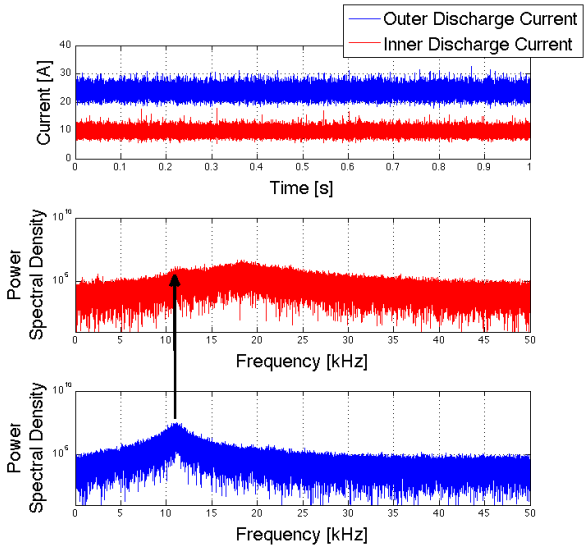

(b) Discharge current measurements for dual-channel operation with a shared discharge power supply

Figure A.1: **Comparison of dual-channel discharge characteristics with separate discharge power supplies and a shared discharge power supply**

Table A.1: **Discharge and performance characteristics for operation with separate discharge power supplies and a shared discharge power supply**

	Separate Power Supplies	Single Power Supply
Discharge Voltage	150	150
Inner Discharge Current [A]	9.53	9.65
Outer Discharge Current [A]	23.65	23.77
Inner $I_{d,AC}/I_d$	11%	10%
Outer $I_{d,AC}/I_d$	7%	7%
Inner Breathing Mode Frequency [kHz]	18.6	19.3
Outer Breathing Mode Frequency [kHz]	11.0	10.9
Thrust [mN]	386	389
Anode Specific Impulse [s]	1211	1220
Anode Efficiency	46%	47%

Shared-power supply operation of a NHT also shows that such a thruster could operate on a single power processing unit (PPU). For the development of a flight model, shared-PPU operation of the nested channels could potentially simplify the implementation of a NHT. As the thrust, anode specific impulse, and anode efficiency did not vary significantly between power supply configurations, the use of a shared PPU is not expected to affect the performance of the thruster

BIBLIOGRAPHY

BIBLIOGRAPHY

[1] Kim, V., Manzella, D. H., and Murashko, V. M., "High-Power Hall Devices: Status and Current Challenges," *International Symposium on Energy Conversion Fundamentals*, Istanbul, Turkey, June 2004, pp. 1–14.

[2] Arhipov, B. A., Vinogradov, V. N., Kozubsky, K. N., Kudriavtsev, S. S., Maslennikov, N. A., and Murashko, V. M., "Development and Application of Electric Thrusters at EDB "Fakel"," *25th International Electric Propulsion Conference*, Cleveland, OH, Jan. 1997, pp. 1–11.

[3] Hargus, Jr, W. A. and Reed, G., "The Air Force Clustered Hall Thruster Program," *28th AIAA/ASME/SAE/ASEE Joint Propulsion Conference & Exhibit*, Indianapolis, IN, July 2002, pp. 1–10.

[4] Pote, B. M., Hruby, V. J., and Tedrake, R. A., "Performance of a Multi-Kilowatt Non-Circular Discharge Hall Thruster," *36th Joint Propulsion Conference & Exhibit*, Huntsville, AL, July 2000, pp. 1–15.

[5] Raitses, Y. F., Smirnov, A., and Fisch, N. J., "Cylindrical Hall Thrusters," *37th AIAA Plasmadynamics and Lasers Conference*, San Francisco, CA, June 2006, pp. 1–9.

[6] Tedrake, R. A., "Shared Magnetics Hall Thruster," *NASA SBIR/STTR Technologies*, Natick, MA, 2006, pp. 1–1.

[7] Duchemin, O., Lorand, A., Notarianni, M., and Chesta, E., "Multi-Channel Hall-Effect Thrusters: Mission Applications and Architecture Trade-Offs," *30th International Electric Propulsion Conference*, SNECMA and CNES, Florence, Italy, Sept. 2007, pp. 1–15.

[8] Temkin, S. E., *Performance Characterization of a Three-axis Hall Effect Thruster*, Master's thesis, Air Force Institute of Techology, Wright-Patterson AFB, OH, Dec. 2010.

[9] Huzel, D. K., Huang, D. H., Arbit, H., Bissell, W. R., Brewster, R., Cardenas, M. P., Cross, E. H., Gaspar, K. C., Gillon, W., Jackson, III, E. D., Martinez, A., Stanley, W. M., and Urquidi, R., *Modern Engineering for Design of Liquid-Propellant Rocket Engines*, Vol. 147 of *Progress in Astronautics and Aeronautics*, American Institute of Aeronautics and Astronautics, 1992.

[10] Stuhlinger, E., "Origin and Early Development of Electric Propulsion Concepts," *AIAA/NASA/OAI Conference of Advanced SEI Technologies*, Cleveland, OH, Sept. 1991, pp. 1–9.

[11] Jahn, R. G., *Physics of Electric Propulsion*, Dover books on physics, McGraw-Hill, Inc., New York, NY, 1968.

[12] Morozov, A. I. and Savelyev, V. V., "Fundamentals of Stationary Plasma Thruster Theory," *Reviews of Plasma Physics*, Springer US, Boston, MA, 2000, pp. 203–391.

[13] Goebel, D. M. and Katz, I., *Fundamentals of Electric Propulsion: Ion and Hall Thrusters*, Jet Propulsion Laboratory: California Institute of Technology, March 2008.

[14] Linnell, J. A., *An Evaluation of Krypton Propellant in Hall Thrusters*, Ph.D. thesis, University of Michigan, Ann Arbor, MI, 2007.

[15] Hofer, R. R., Peterson, P. Y., Jacobson, D. T., and Manzella, D. H., "Factors Affecting the Efficiency of Krypton Hall Thrusters," *46th Meeting of the APS Division of Plasma Physics*, QSS Group, Inc and NASA Glenn Research Center, Savannah, GA, Nov. 2004, pp. 1–13.

[16] Peterson, P. Y., Jacobson, D. T., Manzella, D. H., and John, J. W., "The Performance and Wear Characterization of a High-Power High-Isp NASA Hall Thruster," *41st AIAA/ASME/SAE/ASEE Joint Propulsion Conference & Exhibit*, Tucson, AZ, July 2005, pp. 1–14.

[17] Massey, D. R., *Development of a Direct Evaporation Bismuth Hall Thruster*, Ph.D. thesis, Michigan Technological University, Houghton, MI, 2008.

[18] Marrese-Reading, C., Frisbee, R. H., Sengupta, A., Cappelli, M. A., Tverdokhlebov, S. O., Semenkin, S., and Boyd, I. D., "Very High Isp Thruster with Anode Layer (VHITAL): An Overview," *AIAA SPACE 2004 Conference & Exposition*, San Deigo, CA, Oct. 2004, pp. 1–6.

[19] Brophy, J. R., Ganapathi, G. B., Garner, C. E., Gates, J., Lo, J., Marcucci, M. G., and Nakazono, B., "Status of the Dawn Ion Propulsion System," *40th AIAA/ASME/SAE/ASEE Joint Propulsion Conference & Exhibit*, Fort Lauderdale, FL, July 2004, pp. 1–12.

[20] Racca, G., Marini, A., Stagnaro, L., van Dooren, J., Di Napoli, L., Foing, B., Lumb, R., Volp, J., Brinkmann, J., Grünagel, R., Estublier, D., Tremolizzo, E., McKay, M., Camino, O., Schoemaekers, J., Hechler, M., Khan, M., Rathsman, P., Andersson, G., Ano, K., Berge, S., Bodin, P., Edfors, A., Hussain, A., Kugelberg, J., Larsson, N., Ljung, B., Meijer, L., Mortsell, A., Nordeback, T., Persson, S., and Sjöberg, F., "SMART-1 Mission Description and Development Status," *Planetary and Space Science*, Vol. 50, No. 14-15, Dec. 2002, pp. 1323–1337.

[21] "Boeing 702SP Satellite," 2012.

[22] Andrews, D. G. and Wetzel, E. D., "Solar Electric Space Tug to Support Moon and Mars Exploration Missions," *AIAA SPACE 2005 Conference & Exposition*, Andrews Space, Inc, Long Beach, CA, Aug. 2005, pp. 1–11.

[23] Gilland, J. H., Lapointe, M. R., Oleson, S. R., Mercer, C., Pencil, E. J., and Mason, L. S., "MW-Class Electric Propulsion System Designs for Mars Cargo Transport," *AIAA SPACE 2011 Conference & Exposition*, Long Beach, CA, Sept. 2011, pp. 1–15.

[24] Brophy, J. R., Gershman, R., Strange, N., Landau, D., Merrill, R. G., and Kerslake, T. W., "300-kW Solar Electric Propulsion System Configuration for Human Exploration of Near-Earth Asteroids," *47th AIAA/ASME/SAE/ASEE Joint Propulsion Conference & Exhibit*, San Diego, CA, July 2011, pp. 1–13.

[25] Oleson, S. R., "Electric Propulsion Technology Development for the Jupiter Icy Moons Orbiter Project," *40th AIAA/ASME/SAE/ASEE Joint Propulsion Conference & Exhibit*, Fort Lauderdale, FL, July 2004, pp. 1–26.

[26] Charania, A., St Germain, B., Wallace, J. G., and Olds, J. R., "REACTIONN: A Nuclear Electric Propulsion Mission Concept to the Outer Solar System," *40th AIAA/ASME/SAE/ASEE Joint Propulsion Conference & Exhibit*, Fort Lauderdale, FL, July 2004, pp. 1–13.

[27] "Human Space Exploration Framework Summary," Tech. rep., National Aeronautics and Space Administration, Washington, DC, Jan. 2011.

[28] Manzella, D. H., Jankovsky, R. S., and Hofer, R. R., "Laboratory Model 50 kW Hall Thruster," *38th AIAA/ASME/SAE/ASEE Joint Propulsion Conference & Exhibit*, Indianapolis, IN, July 2002, pp. 1–11.

[29] Soulas, G., Haag, T. W., Herman, D., Huang, W., Kamhawi, H., and Shastry, R., "Performance Test Results of the NASA-457M v2 Hall Thruster," *48th AIAA/ASME/SAE/ASEE Joint Propulsion Conference & Exhibit*, American Institute of Aeronautics and Astronautics, Atlanta, GA, July 2012, pp. 1–17.

[30] Hofer, R. R., Goebel, D. M., Snyder, J. S., and Sandler, I., "BPT-4000 Hall Thruster Extended Power Throttling Range Characterization for NASA Science Missions," *31st International Electric Propulsion Conference*, Ann Arbor, MI, Sept. 2009, pp. 1–21.

[31] Mikellides, I. G., Katz, I., Hofer, R. R., Goebel, D. M., de Grys, K. H., and Mathers, A. J., "Magnetic shielding of the channel walls in a Hall plasma accelerator," *Physics of Plasmas*, Vol. 18, No. 3, March 2011, pp. 033501.

[32] Mikellides, I. G., Katz, I., and Hofer, R. R., "Design of a Laboratory Hall Thruster with Magnetically Shielded Channel Walls, Phase I: Numerical Simulations," *47th AIAA/ASME/SAE/ASEE Joint Propulsion Conference & Exhibit*, San Diego, CA, July 2011, pp. 1–18.

[33] Hofer, R. R., Goebel, D. M., Mikellides, I. G., and Katz, I., "Design of a Laboratory Hall Thruster with Magnetically Shielded Channel Walls, Phase II: Experiments," *48th AIAA/ASME/SAE/ASEE Joint Propulsion Conference & Exhibit*, Atlanta, GA, July 2012, pp. 1–39.

[34] Mikellides, I. G., Katz, I., Hofer, R. R., and Goebel, D. M., "Design of a Laboratory Hall Thruster with Magnetically Shielded Channel Walls, Phase III: Comparison of Theory with Experiment," *48th AIAA/ASME/SAE/ASEE Joint Propulsion Conference & Exhibit*, Atlanta, GA, July 2012, pp. 1–26.

[35] Choueiri, E. Y., "Fundamental difference between the two Hall thruster variants," *Physics of Plasmas*, Vol. 8, No. 11, Nov. 2001, pp. 5025–5033.

[36] Schmidt, D. P., Meezan, N. B., Hargus, Jr, W. A., and Cappelli, M. A., "Operating Characteristics of a Linear Hall Thruster with an Open Electron-Drift," *35th AIAA/ASME/SAE/ASEE Joint Propulsion Conference & Exhibit*, July 1999, pp. 1–11.

[37] Smirnov, A., Raitses, Y. F., and Fisch, N. J., "Parametric Investigation of Miniaturized Cylindrical and Annular Hall Thrusters," *Journal of Applied Physics*, Vol. 92, No. 10, Nov. 2002, pp. 5673–5679.

[38] Hofer, R. R., *Development and Characterization of High-Efficiency, High-Specific Impulse Xenon Hall Thrusters*, Ph.D. thesis, University of Michigan, Ann Arbor, MI, 2004.

[39] Reid, B. M., *The Influence of Neutral Flow Rate in the Operation of Hall Thrusters*, Ph.D. thesis, University of Michigan, Ann Arbor, MI, 2009.

[40] Brown, D. L., *Investigation of Low Discharge Voltage Hall Thruster Characteristics and Evaluation of Loss Mechanisms*, Ph.D. thesis, University of Michigan, Ann Arbor, MI, 2009.

[41] Kim, V., "Main Physical Features and Processes Determining the Performance of Stationary Plasma Thrusters," *Journal of Propulsion and Power*, Vol. 14, No. 5, Sept. 1998, pp. 736–743.

[42] Beal, B. E., *Clustering of Hall Effect Thrusters for High-Power Electric Propulsion Applications*, Ph.D. thesis, University of Michigan, Ann Arbor, MI, 2004.

[43] Grishin, S. D. and Leskov, L. V., *Electric Rocket Engines for Spacecraft*, Machinostroenie, Moscow, USSR, 1989.

[44] Jacobson, D. T., John, J. W., Kamhawi, H., and Manzella, D. H., "An Overview of Hall Thruster Development at NASA's John H. Glenn Research Center," *41st AIAA/ASME/SAE/ASEE Joint Propulsion Conference & Exhibit*, Tucson, AZ, July 2005, pp. 1–15.

[45] McVey, J. B. and Perrucci, A. S., "Multichannel Hall Effect Thruster," April 2006.

[46] Szabo, Jr, J. J., Pote, B. M., Hruby, V. J., Byrne, L. T., Tedrake, R. A., Kolencik, G., Kamhawi, H., and Haag, T. W., "A Commercial One Newton Hall Effect Thruster for High Power In-Space Missions," *47th AIAA/ASME/SAE/ASEE Joint Propulsion Conference & Exhibit*, San Diego, CA, July 2011, pp. 1–11.

[47] Florenz, R., Gallimore, A. D., and Peterson, P. Y., "Developmental Status of a 100-kW Class Laboratory Nested channel Hall Thruster," *32nd International Electric Propulsion Conference*, Wiesbaden, Germany, Sept. 2011, pp. 1–9.

[48] Beal, B. E. and Gallimore, A. D., "Effects of Cathode Configuration on Hall Thruster Cluster Plume Properties," *Journal of Propulsion and Power*, Vol. 23, No. 4, July 2007, pp. 836–844.

[49] Walker, M. L. R. and Gallimore, A. D., "Hall Thruster Cluster Operation with a Shared Cathode," *Journal of Propulsion and Power*, Vol. 23, No. 3, May 2007, pp. 528–536.

[50] Walker, M. L. R., *Effects of Facility Backpressure on the Performance and Plume of a Hall Thruster*, Ph.D. thesis, University of Michigan, Ann Arbor, MI, 2005.

[51] Hofer, R. R. and Jankovsky, R. S., "A Hall Thruster Performance Model Incorporating the Effects of a Multiply-Charged Plasma," *37th AIAA/ASME/SAE/ASEE Joint Propulsion Conference & Exhibit*, Salt Lake City, UT, July 2001, pp. 1–12.

[52] Hofer, R. R., Katz, I., Mikellides, I. G., Goebel, D. M., Jameson, K. K., Sullivan, R. M., and Johnson, L. K., "Efficacy of Electron Mobility Models in Hybrid-PIC Hall Thruster Simulations," *44th AIAA/ASME/SAE/ASEE Joint Propulsion Conference & Exhibit*, Hartford, CT, July 2008, pp. 1–29.

[53] Brown, D. L., Larson, C. W., Beal, B. E., and Gallimore, A. D., "Methodology and Historical Perspective of a Hall Thruster Efficiency Analysis," *Journal of Propulsion and Power*, Vol. 25, No. 6, Nov. 2009, pp. 1163–1177.

[54] Jameson, K. K., Goebel, D. M., Hofer, R. R., and Watkins, R. M., "Cathode Coupling in Hall Thrusters," *30th International Electric Propulsion Conference*, Jet Propulsion Laboratory, Florence, Italy, Sept. 2007, pp. 1–20.

[55] Jameson, K. K., *Investigation of Hollow Cathode Effects on Total Thruster Efficiency in a 6 kW Hall Thruster*, Ph.D. thesis, University of California, Los Angeles, Los Angeles, CA, 2008.

[56] Shastry, R., *Experimental Characterization of the Near-Wall Region in Hall Thrusters and its Implications on Performance and Lifetime*, Ph.D. thesis, University of Michigan, Ann Arbor, MI, 2011.

[57] Huang, W., *Study of Hall Thruster Discharge Channel Wall Erosion via Optical Diagnostics*, Ph.D. thesis, University of Michigan, Ann Arbor, MI, 2011.

[58] McDonald, M. S., *Electron Transport in Hall Thrusters*, Ph.D. thesis, University of Michigan, Ann Arbor, MI, 2012.

[59] Goebel, D. M., Jameson, K. K., and Hofer, R. R., "Hall Thruster Cathode Flow Impact on Coupling Voltage and Cathode Life," *Journal of Propulsion and Power*, Vol. 28, No. 2, Jan. 2012, pp. 355–363.

[60] Goebel, D. M. and Watkins, R. M., "Compact lanthanum hexaboride hollow cathode," *Review of Scientific Instruments*, Vol. 81, No. 8, Aug. 2010, pp. 083504.

[61] Hofer, R. R. and Jankovsky, R. S., "The Influence of Current Density and Magnetic Field Topography in Optimizing the Performance, Divergence, and Plasma Oscillations of High Specific Impulse Hall Thrusters," *28th International Electric Propulsion Conference*, QSS Group, Inc and NASA Glenn Research Center, Toulouse, France, March 2003, pp. 1–12.

[62] Walker, M. L. R. and Gallimore, A. D., "Performance Characteristics of a Cluster of 5-kW Laboratory Hall Thrusters," *Journal of Propulsion and Power*, Vol. 23, No. 1, Jan. 2007, pp. 35–43.

[63] Haag, T. W., "Thrust stand for high-power electric propulsion devices," *Review of Scientific Instruments*, Vol. 62, No. 5, May 1991, pp. 1186–1191.

[64] Xu, K. G. and Walker, M. L. R., "High-Power, Null-Type, Inverted Pendulum Thrust Stand," *Review of Scientific Instruments*, Vol. 80, No. 5, May 2009, pp. 055103.

[65] Shastry, R., Hofer, R. R., Reid, B. M., and Gallimore, A. D., "Method for analyzing EB probe spectra from Hall thruster plumes," *Review of Scientific Instruments*, Vol. 80, No. 6, June 2009, pp. 063502.

[66] Reid, B. M., Shastry, R., Gallimore, A. D., and Hofer, R. R., "Angularly-Resolved EB Probe Spectra in the Plume of a 6-kW Hall Thruster," *44th AIAA/ASME/SAE/ASEE Joint Propulsion Conference & Exhibit*, Hartford, CT, July 2008, pp. 1–21.

[67] King, L. B., *Transport-Property and Mass Spectral Measurements in the Plasma Exhaust Plume of a Hall-Effect Space Propulsion System*, Ph.D. thesis, University of Michigan, Ann Arbor, MI, 1998.

[68] Chen, F. F., "Lecture Notes on Langmuir Probe Diagnostics," *32nd IEEE International Conference on Plasma Science*, Jeju, Korea, June 2003, pp. 1–42.

[69] Haas, J. M., *Low-perturbation Interrogation of the Internal and Near-field Plasma Structure of a Hall Thruster Using a High-Speed Probe Positioning System*, Ph.D. thesis, University of Michigan, Ann Arbor, MI, 2001.

[70] Reid, B. M. and Gallimore, A. D., "Near-field Ion Current Density Measurements of a 6-kW Hall Thruster," *31st International Electric Propulsion Conference*, Ann Arbor, MI, Sept. 2009, pp. 1–14.

[71] Sheehan, J. P. and Hershkowitz, N., "Emissive probes," *Plasma Sources Science and Technology*, Vol. 20, No. 6, Nov. 2011, pp. 063001.

[72] Schwager, L. A., "Effects of secondary and thermionic electron emission on the collector and source sheaths of a finite ion temperature plasma using kinetic theory and numerical simulation," *Physics of Fluids B*, Vol. 5, No. 2, Feb. 1993, pp. 631–645.

[73] Herman, D. A., *The Use of Electrostatic Probes to Characterize the Discharge Plasma Structure and Identify Discharge Cathode Erosion Mechanisms in Ring-Cusp Ion Thrusters*, Ph.D. thesis, University of Michigan, 2005.

[74] Chen, F. F., "Electric Probes," *Plasma Diagnostic Techniques*, Academic Press, Inc., New York, NY, 1999, pp. 1–88.

[75] Johnson, E. O. and Malter, L., "Double-Probe Method for Determination of Electron Temperatures in Steady and Time-Varying Gas Discharges," *Physical Review*, Vol. 76, No. 9, Sept. 1949, pp. 1411–1412.

[76] Johnson, E. O. and Malter, L., "A Floating Double Probe Method for Measurements in Gas Discharges," *Physical Review*, Vol. 80, No. 1, Oct. 1950, pp. 58–68.

[77] "Agilent Vacuum Measurement," Agilent Technologies, 2011.

[78] Dushman, S., *Scientific foundations of vacuum technique*, Wiley, New York, NY, 2nd ed., 1962.

[79] Randolph, T. M., Kim, V., Kaufman, H. R., Kozubsky, K. N., Zhurin, V. V., and Day, M., "Facility Effects on Stationary Plasma Thruster Testing," *23rd International Electric Propulsion Conference*, Seattle, WA, Sept. 1993, pp. 1–11.

[80] Hofer, R. R., Peterson, P. Y., and Gallimore, A. D., "Characterizing Vacuum Facility Backpressure Effects on the Performance of a Hall Thruster," *27th International Electric Propulsion Conference*, Pasadena, CA, Oct. 2001, pp. 1–10.

[81] Byers, D. and Dankanich, J. W., "A Review of Facility Effects on Hall Effect Thrusters," *31st International Electric Propulsion Conference*, Ann Arbor, MI, Sept. 2009, pp. 1–12.

[82] Diamant, K. D., Spektor, R., Beiting, E. J., Young, J. A., and Curtiss, T. J., "The Effects of Background Pressure on Hall Thruster Operation," *48th AIAA/ASME/SAE/ASEE Joint Propulsion Conference & Exhibit*, Atlanta, GA, July 2012, pp. 1–13.

[83] Huang, W., Shastry, R., Herman, D. A., Soulas, G. C., and Kamhawi, H., "Ion Current Density Study of the NASA-300M and NASA-457Mv2 Hall Thrusters," *48th AIAA/ASME/SAE/ASEE Joint Propulsion Conference & Exhibit*, Atlanta, GA, July 2012, pp. 1–29.

[84] Hofer, R. R. and Gallimore, A. D., "Recent Results from Internal and Very-Near-Field Plasma Diagnostics of a High Specific Impulse Hall Thruster," *28th International Electric Propulsion Conference*, Toulouse, France, March 2003, pp. 1–16.

[85] Brown, D. L. and Gallimore, A. D., "Evaluation of Facility Effects on Ion Migration in a Hall Thruster Plume," *Journal of Propulsion and Power*, Vol. 27, No. 3, May 2011, pp. 573–585.

[86] Walker, M. L. R., Victor, A. L., Hofer, R. R., and Gallimore, A. D., "Effect of Backpressure on Ion Current Density Measurements in Hall Thruster Plumes," *Journal of Propulsion and Power*, Vol. 21, No. 3, May 2005, pp. 408–415.

[87] Nakles, M. R. and Hargus, Jr, W. A., "Background Pressure Effects on Ion Velocity Distribution Within a Medium-Power Hall Thruster," *Journal of Propulsion and Power*, Vol. 27, No. 4, July 2011, pp. 737–743.

[88] Patterson, M. J., "Electric Propulsion Apparatus: Next-Generation Electric Propulsion Thruster(s)," *18th Advanced Space Propulsion Workshop*, Colorado Springs, CO, Nov. 2010, pp. 1–20.

[89] Dankanich, J. W. and Patterson, M. J., "Mission Performance of the Dual-Mode Hybrid Engine," *47th AIAA/ASME/SAE/ASEE Joint Propulsion Conference & Exhibit*, San Diego, CA, July 2011, pp. 1–13.

[90] Liang, R. and Gallimore, A. D., "Constant-Power Performance and Plume Measurements of a Nested-Channel Hall-Effect Thruster," *32nd International Electric Propulsion Conference*, Wiesbaden, Germany, Sept. 2011, pp. 1–14.

[91] Lobbia, R. B., Sekerak, M. J., Liang, R., and Gallimore, A. D., "High-speed Dual Langmuir Probe Measurements of the Plasma Properties and EEDFs in a HET plume," *32nd International Electric Propulsion Conference*, Wiesbaden , Germany, Sept. 2011, pp. 1–8.

[92] Hofer, R. R., McDonald, M. S., and Gallimore, A. D., "Inter-Channel Discharge Coupling Induced Plasma Oscillations and Electron Transport in Nested Hall Thrusters," *National Aeronautics and Space Administration*, Pasadena, CA, 2012, pp. 1–1.

[93] McDonald, M. S., Sekerak, M. J., Gallimore, A. D., and Hofer, R. R., "Plasma Oscillation Effects on Nested Hall Thruster Operation and Stability," *2013 IEEE Aerospace Conference*, Big Sky, MT, 2013, pp. 1–18.

[94] Lobbia, R. B., *A Time-resolved Investigation of the Hall Thruster Breathing Mode*, Ph.D. thesis, University of Michigan, Ann Arbor, MI, 2010.